Design, Analysis, Modeling and Testing of a Micro-scale Refrigeration System

Submitted in partial fulfillment of the requirements for

the degree of

Doctor of Philosophy

in

Mechanical Engineering

Dongzhi Guo

B.S., Thermal and Power Engineering, Xi'an Jiaotong University (2008)
M.S., Engineering Thermophysics, Xi'an Jiaotong University (2010)

Carnegie Mellon University
Pittsburgh, PA

August, 2014

To my mother

Acknowledgments

I wish to express my sincere gratitude to my advisor, Prof. S.C. Yao, who not only guided my research academically and supported me financially, but also helped me to build the career path perceptively. His talent and experience in thermal science and MEMS enriched my knowledge, broadened my academic view, and made me ready for future challenges.

I am grateful to my thesis committee members, Prof. Alan J.H. McGaughey, Prof. Gary K. Fedder and Prof. Sheng Shen, for their valuable comments on my thesis. Prof. McGaughey always gave advice and helped me a lot to polish my writings during my PhD study. Prof. Fedder is knowledgeable in MEMS technology and provided many brilliant suggestions for the project.

I would like to thank all members in ACM project group. My special appreciation goes to Suresh Santhanam for his instructions of microfabrication skills and assistances for the experiement preparations. Equal appreciation goes to my friend, Jinsheng Gao, who worked with me on this project. He always encouraged me to make progress in the research. I must thank Ying-Ju Yu for her contributions to this thesis. I am also indebted to other members in ACM group for the many helpful discussions, including Andrew Slippey, Taylor Maxwell, David Wolf & Chris Peters at ACT, and Matthew Moran at Isotherm Technologies LLC.

In addition, I owe gratitudes to Dr. Yang Zhang for his help with my thesis. I am also thankful to Prof. Q.M. Zhang and Dr. Haiming Gu at Penn State for their valuable discussions.

Most importantly, none of this would be achieved without the generous understanding and continuous support from my family. I would like to express my deepest gratitude to them.

Finally, this work was supported by the Defense Advanced Research Projects Agency (DARPA) and the U.S. Army Aviation and Missile Research, Development, and Engineering Center (AMRDEC) under Grant No. W31P4Q-10-1-0015.

Abstract

Chip scale refrigeration system is critical for the development of electronics with the rapid increase of power consumption and substantial reduction of device size, resulting in an emergent demand on novel cooling technologies with a high efficiency for the thermal management. In this thesis, active refrigeration devices based on Stirling cycle and an electrocaloric material, are designed and investigated to achieve a high cooling performance.

Firstly, a new Stirling micro-refrigeration system composed of arrays of silicon MEMS cooling elements is designed and evaluated. The cooling elements are fabricated in a stacked array on a silicon wafer. A regenerator is placed between the compression (hot side) and expansion (cold side) diaphragms, which are driven electrostatically. Under operating conditions, the hot and cold diaphragms oscillate sinusoidally and out of phase such that heat is extracted to the expansion space and released from the compression space. A first-order of thermodynamic analysis is performed to study the effect of geometric parameters. Losses due to regenerator non-idealities and chamber heat transfer limitation are estimated. A multiphysics computational approach for analyzing the system performance that considers compressible flow and heat transfer with a large deformable mesh is demonstrated. The optimal regenerator porosity for the best system *COP* (coefficient of performance) is identified. To overcome the computational complexity brought about by the fine pillar structure in the regenerator, a porous medium model is used to allow for modeling of a full element. The analysis indicates the work recovery of the system and the diaphragm actuation are main challenges for this cooler design.The pressure drop and friction factor of gas flow across circular silicon micro pillar arrays fabricated by deep reactive ion etch (DRIE) process are investigated. A new correlation that considers the coupled effect of pillar spacing and aspect ratio, is proposed to predict the friction factor in a Reynolds

number range of 1-100. Silicon pillars with large artificial roughness amplitudes is also fabricated, and the effect of the roughness is studied in the laminar flow region. The significant reduction of pressure drop and friction factor indicates that a large artificial roughness could be built for pillar arrays in the regenerator to enhance the micro-cooler efficiency.

The second option is to develop a fluid-based refrigeration system using an electrocaloric material poly(vinylidene fluoride-trifluoroethylene-chlorofluoroethylene) [P(VDF-TrFE-CFE)] terpolymer. Each cooling element includes two diaphragm actuators fabricated in the plane of a silicon wafer, which drive a heat transfer fluid back and forth across terpolymer layers that are placed between them. Finite element simulations with an assumption of sinusoidal diaphrahm motions are conducted to explore the system performance detailedly, including the effects of the applied electric field, geometric dimensions, operating frequency and externally-applied temperature span. Multiphysics modeling coupled with solid-fluid interaction, heat transfer, electrostatics, porous medium and moving mesh technique is successfully performed to verify the thermal modeling feasibility. The electrocaloric effect in thin films of P(VDF-TrFE-CFE) terpolymer is directly measured by infrared imaging at ambient conditions. At an electric field of 90 V/μm, an adiabatic temperature change of 5.2 °C is obtained and the material performance is stable over a long testing period. These results suggest that application of this terpolymer is promising for micro-scale refrigeration.

Contents

Acknowledgments iii
Abstract iv
List of Tables ix
List of Figures x
Nomenclature xv
Chapter 1 Introduction 1
1.1 Motivation 1
1.2 Stirling cooling 4
1.3 Electrocaloric cooling 5
1.4 Thesis overview 9
Chapter 2 Design and thermodynamic analysis of a MEMS-based Stirling microcooler 12
2.1 Introduction 12
2.2 Design concept 14
2.2.1 Overall concept 14
2.2.2 Hot and cold chambers 16
2.2.3 Regenerator 17
2.2.4 High-frequency operation 17
2.3 Thermodynamic analysis of the system 18
2.3.1 Stirling cycle 18
2.3.2 Thermodynamic analysis of the Stirling cycle 19
2.4 System-level loss evaluation 24
2.4.1 Coefficient of performance 24
2.4.2 Energy balance 25
2.4.3 System evaluation 32
2.5 Work recovery of the system 34
2.6 Summary 35
Chapter 3 Multiphysics modeling of the micro Stirling refrigeration system 36
3.1 Introduction 36
3.2 Regenerator analysis 36

3.2.1 Fluid compressibility 40
3.2.2 Porosity optimization 41
3.3 System evaluation 44
3.3.1 Porous medium governing equations 44
3.3.2 Specifying the permeability and Forchheimer coefficient 45
3.3.3 Convection coefficient 46
3.3.4 Computational domain and boundary conditions 47
3.3.5 Results and discussions 49
3.4 Modeling of diaphragm actuation and thermal evaluation 52
3.5 Summary 55
Chapter 4 Experimental investigation of laminar flow across short micro pin fin arrays 56
4.1 Introduction 56
4.2 Experimental details 59
4.2.1 Device description 59
4.2.2 Data reduction 64
4.3 Results and discussions 65
4.3.1 Coupled effect of height-to-diameter ratio and pitch-to-diameter ratio 65
4.3.2 Effect of artificial roughness 70
4.4 Summary 74
Chapter 5 Design and modeling of a fluid-based electrocaloric refrigeration system 76
5.1 Introduction 76
5.2 Design concept 78
5.2.1 Overall design 78
5.2.2 Hot and cold chambers 80
5.2.3 Working fluid and thermal penetration 80
5.3 Thermal evaluation of the system 81
5.3.1 Governing equations 81
5.3.2 Computational setup 82
5.3.3 Results and discussions 83
5.4 Diaphragm modeling and multiphysics simulation 93
5.4.1 PDMS Diaphragm modeling 93

5.4.2 Porous medium model 95
5.4.3 Multiphysics modeling 96
5.5 Summary 100
Chapter 6 Electrocaloric characterization of P(VDF-TrFE-CFE) terpolymer 101
6.1 Introduction 101
6.2 Experimental details 102
6.3 Experimental results 104
6.3.1 Measured results and the adiabatic temperature change 104
6.3.2 Effect of stage temperature and operating frequency 110
6.3.3 P(VDF-TrFE-CFE) terpolymer thin film stability 112
6.4 Summary 113
Chapter 7 Summary of thesis work and future research 114
7.1 Summary of thesis work 114
7.2 Future research 116
Bibliography 119
Appendices 130

List of Tables

Table 2.1 Comparison of the regenerator effectiveness at different operating frequencies from an analytical model [Eq. (2.26)] and finite element simulations [35]. When the porosity is 0.798, 0.864, or 0.916, the maximum difference between the two predictions is less than 5%, giving confidence to the use of the much simpler analytical model..... 29

Table 2.2 Comparison of the pressure drop through the regenerator at different operating frequencies calculated from an analytical model [Eqs. (2.31)-(2.34)] and FEA simulations [35]. When the porosity is 0.798, 0.864, or 0.916, the maximum difference does not exceed 15%, giving confidence to the use of the much simpler analytical model..... 31

Table 3.1 Regenerator pillar configurations used in porosity optimization study. 40

Table 4.1 A summary of the geometric parameters of test devices 62

Table 4.2 Mean absolute error of friction factors between the present experimental data and values calculated from available correlations for circular pillar array..... 68

Table 4.3 Mean absolute error of the new correlation (Eq. (4.7)) for circular pillar array..... 70

Table 5.1 Summary of EC materials and their performances 77

Table 5.2 Properties of HT-70 and P(VDF-TrFE-CFE) terpolymer..... 80

Table 5.3 The chamber depths and EC module heights with different EC polymer thickness 87

List of Figures

Figure 1.1 A schematic of TMT programs (MACE, TGP, ACM, NTI and NJTT) and the task areas in a representative device [4]. 2

Figure 1.2 Theoretical *COP* as a function the temperature difference T_H-T_C for a thermoelectric cooler. 3

Figure 1.3 The Moran concept [23,24] uses silicon diaphragms with vertical electrostatic comb drives to move the working gas through a regenerator vertically (i.e., perpendicular to the plane of the silicon wafer). Left: Micro-Stirling cooler assembly. Right: Regenerator design showing orthogonal flow between diaphragms. 5

Figure 1.4 Conceptual demonstration of the mechanism of the electrocaloric effect. The material becomes polar-ordered under the electric field and the decreased material entropy increases temperature. When the electric field is removed, the material returns to a polar-disordered state, the material entropy increases, and the temperature drops. 6

Figure 1.5 Design and setup of a solid-state refrigerator based on the electrocaloric effect (Jia and Ju [31]). 7

Figure 1.6 Schematic of the prototype of a solid-state electrocaloric cooler (Gu et al. [32]), which includes two 0.25 mm thick 24-layer EC module and four 0.5 mm thick regenerators 8

Figure 2.1 The current in-plane micro-scale implementation positions the regenerator flow channel parallel to the wafer plane connecting the compression and expansion chambers, allowing for thermal isolation. Top: Cross-sectional view of Stirling micro cooler elements showing the silicon chamber and the in-plane gas flow direction. Bottom: Planar view (*A*-*A'*) of the cooler element displaying the polymer membrane with the embedded electrodes and silicon pillars in the regenerator. 14

Figure 2.2 Solid-model view of a Stirling microcooler element that is 5 mm-long, 2.5 mm-wide, has a thickness of 150 μm, and is fabricated on a silicon wafer. (Courtesy of Jinsheng Gao [34]) 15

Figure 2.3 Vision of the arrayed Stirling microcooler. A 2 × 2 cm^2 cooling area is made by first arraying eight elements along their width and then stacking 114 of these 1 × 8 arrays 16

Figure 2.4 The ideal Stirling refrigeration cycle includes four processes: isothermal compression (1-2), regenerative cooling (2-3), isothermal expansion (3-4) and regenerative heating (4-1). 19

Figure 2.5 Geometric parameters for a microcooler element. The dead volume, V_D, includes the regenerator volume, V_r, and the non-swept volume between the regenerator and the chambers, V_{ns}. V_C and V_H are the swept volume in the cold and hot chambers. 19

Figure 2.6 (a) Dimensionless heat extraction as a function of swept volume ratio for different non-swept volume ratios. The lead phase angle of the cold side to the hot side is 90°. (b) Dimensionless heat extraction as a function of lead phase angle for different swept volume ratios. The non-swept volume ratio is 0.4. 23

Figure 2.7 System sketch of the single Stirling microcooler element and the energy balance in each chamber. $T_{g,C}$ and $T_{g,H}$ are the gas temperature in the cold and hot chambers. The heat source temperature is T_C and the heat sink temperature is T_H. 26

Figure 2.8 (a) System *COP* as a function of regenerator porosity at different operating frequencies. The swept volume ratio is unity for the two chambers and the phase lag of the volume variations between the cold and hot sides is 90°. (b) System cooling power density as a function of the

operating frequency at different porosities. The swept volume ratio is unity for the two chambers and the phase lag of the volume variations between the cold and hot sides is 90°. . 33

Figure 2.9 System *COP* and cooling power density as a function of frequency with different losses. The swept volume ratio is unity for the two chambers and the phase lag of the volume variations between the cold and hot sides is 90°. (a) *COP* (b) Cooling power density at $\varepsilon = 0.864$. 34

Figure 3.1 Two-dimensional regenerator computational domain and boundary conditions for the porosity optimization study (see also Table 3.1). The horizontal pitch is S_L and the vertical pitch is S_T. The regenerator length is L. 39

Figure 3.2 Frequency-dependence of (a) time-averaged pressure drop across the regenerator and (b) regenerator effectiveness for $S_L / S_T = 0.289$ and $\varepsilon = 0.892$ and 0.833. The differences between considering compressible or incompressible flow are small. 41

Figure 3.3 Effect of operating frequency and porosity for $S_L / S_T = 0.289$ on (a) time-averaged pressure drop across the regenerator and (b) regenerator effectiveness..... 42

Figure 3.4 Predicted *COP* as a function of operating frequency and porosity for (a) $S_L / S_T = 0.289$ and (b) $S_L / S_T = 0.866$. 43

Figure 3.5 (a) Pressure drop across the regenerator as a function of average fluid velocity between (i) the full pillars structure and (ii) the porous medium model. (b) Regenerator Nusselt number as a function of Reynolds number for the current calculations and from existing correlations [49,59,60]. The current simulation results are used for the system modeling. 46

Figure 3.6 Computational domain and geometry for the three-dimensional full-system model. The hot and cold diaphragms, which have a 90° phase lag, prescribe the moving boundaries of the fluid flow. The regenerator and the dead space are replaced by the porous medium. 48

Figure 3.7 Space-averaged cooling capacity as a function of time at an operating frequency of 100 Hz when the porosity is 0.892. Steady state is achieved after four cycles. 49

Figure 3.8 The temperature contours for the full Stirling cooler system simulation. (a) One quarter of the cycle at an operating frequency of 100 Hz. (b) Three quarters of the cycle at an operating frequency of 100 Hz. (c) One quarter of the cycle at an operating frequency of 800 Hz. (d) Three quarters of the cycle at an operating frequency of 800 Hz. 50

Figure 3.9 (a) System cooling power density as a function of the frequency from the multiphysics simulations and the analytical calculation from Chapter 2. With the increase of the operating frequency, the cooling capacity increases. (b) Multiphysics simulation prediction of the system *COP* and the analytical result as a function of the cooling power density. The theoretical *COP* is 11.5 With $T_H = 313.15$ K and $T_C = 288.15$ K. 52

Figure 3.10 Computation domain and configuration for finite-element analysis. 53

Figure 3.11 (a) Pressure increase in the chamber vs. the applied voltage on the diaphragm. (b) Pressure increase in the chamber vs. effective Young's Modulus of the diaphragm at 200V. 54

Figure 3.12 Temperature drop vs. pressure differential. The maximum pressure of 1600 Pa is indicated by vertical black dotted line. 55

Figure 4.1 SEM of a fabricated regenerator with rough pillars [80]. The silicon oxide mesh layer is on the top. 58

Figure 4.2 (a) Top view of a sample device including micro pin fin array, pressure ports, inlet and outlet. (b) View of one device under microscope. (c) Geometrical dimensions of the micro-pillar

array. (d) Types of the rough pillar. Type I: coarse roughness with 6 teeth and II: fine roughness with 8 teeth. 60

Figure 4.3 Typical SEM images of micro silicon pillar array with or without roughness. 61

Figure 4.4 Wyko images for quantifying the height of micro silicon pillars. 63

Figure 4.5 Friction factors as a function of *Re* for the circular staggered pillar array with different height-to-diameter ratios (a) S_T/d=1.5 (b) S_T/d=2.3. The result for infinite long pillar is from numerical simulation. 66

Figure 4.6 Friction factors for the circular staggered pillar array with different pitch-to-diameter ratios (S_T/d=1.5 and 2.3) when *H/d* is 0.48, 0.96, and 2.28. 67

Figure 4.7 Friction factor comparison between experimental data and values calculated from the new correlation. 70

Figure 4.8 Friction factors for circular pin fins and rough pillars with different roughness amplitudes. (a) Type I: coarse roughness (b) Type II: fine roughness. The pitch-to-diameter ratio is 1.5 and the height-to-diameter ratio is 1.52. 71

Figure 4.9 Friction factor of rough pillars for different roughness types (coarse roughness and fine roughness). The pitch-to-diameter ratio is 1.5 and the roughness amplitude ratio is 0.2. 72

Figure 4.10 Friction factor comparisons of circular and rough pillar arrays with different pitch-to-diameter ratios (1.5 and 2.3). The height-to-diameter ratio is 1.52 and the roughness amplitude ratio is 0.2. 73

Figure 5.1 Solid-model view of the EC cooler element. The two diaphragm actuators are driven electro-statically. The EC module, which includes multiple terpolymer layers, is located between two diaphragm actuators. The fluid flow is within the plane of the wafer (Courtesy of Andrew Slippey). 78

Figure 5.2 The thermodynamic refrigeration cycle of a fluid element based on the EC effect. The process includes four steps: (A) heat absorption, (B) polarization, (C) heat rejection, and (D) depolarization. 79

Figure 5.3 Computational region of the EC cooling device. 83

Figure 5.4 The smooth trapezoidal waveform of electric field applied to the EC module and the motion of the center point for the hot diaphragm. τ is the period of a cycle. E_{max} is the amplitude of the electric field. Z_{max} is the maximum amplitude of the hot diaphragm motion. Δt_1 is the transit time when the electric field rises/drops. Δt_2 is the time lag between the diaphragm motion and the electric field in the EC module. 84

Figure 5.5 Cooling power density, which is space-averaged on the cold end surface of the element, versus time. The operating frequency is 10 Hz, heat source temperature T_C is 295.15 K, Δt_1 is 0.02 s, and Δt_2 is 0.025 s. The heat flux is positive, which indicates the heat flow direction is from the cold side to the hot side. 85

Figure 5.6 Distributions of temperature in the *x* direction in the element: (a) t = 0.925 s; (b) t = 0.975 s. At t = 0.925 s, the hot diaphragm is at the minimum displacement, and the cold diaphragm is at the maximum displacement. At t = 0.975 s, the diaphragm positions are reversed. The operating frequency is 10 Hz, heat source temperature T_C is 295.15 K, Δt_1 is 0.02 s, and Δt_2 is 0.025 s. 85

Figure 5.7 Time-averaged cooling power densities due to the change of (a) transit time (Δt_1) (b) time lag between the diaphragm and the electric field (Δt_2). The operating frequency is 1 Hz or 20 Hz. T_C is 295.15 K. 86

Figure 5.8 (a) The cooling power density and (b) pressure drop with different EC layer thickness at a frequency of 10 Hz. 87

Figure 5.9 (a) The cooling power density and (b) pressure drop with different EC module lengths at a frequency of 10 Hz. The EC channel height is 50 μm, the fin width is 50 μm and the channel width at outlet of chambers is 50 μm. Four EC channels and five EC polymer layers are placed in the EC module. The middle layer thickness of EC material is 20 μm and the top and bottom layers thickness are 10 μm. 88

Figure 5.10 (a) Cooling power density (b) Pressure drop vs width of fins at outlet of chambers with different channel widths. The frequency is 10 Hz. Temperature span is 5 K. EC module length is 2.5 mm. EC channel height is 50 μm. 89

Figure 5.11 (a) Time-averaged cooling power density (b) *COP* as a function of operating frequency. The transit time Δt_1 is 0.2τ, the time lag Δt_2 is 0.25τ, and T_C is 295.15 K. 91

Figure 5.12 (a) Time - averaged cooling power density, (b) system *COP* and (c) percent of Carnot *COP*: COP/COP_C vs. the temperature span between the heat sink and the heat source at different electric field amplitudes. The transit time Δt_1 is 0.2τ and the time lag Δt_2 is 0.25τ. The operating frequency is 10 Hz. 92

Figure 5.13 (a) Displacement vs pressure comparisons between the linear elastic model, Mooney Rivlin model, and experimental values [97]. (b) Comparison of PDMS membrane deformation shape between the finite element simulation based on Mooney Rivlin model and experimental result [97]..... 94

Figure 5.14 2D computational region of the EC cooling device coupled with multiple physics phenomena. 97

Figure 5.15 Temperature contours at different time when the diaphragm is driven electrostatically at an operating frequency of 5 Hz. (a) t = 1 s (b) t = 1.05 s (c) t = 1.1 s (d) t = 1.15 s..... 97

Figure 5.16 The volume variations of hot and cold chambers and the electric filed applied to EC materials. 98

Figure 5.17 The volume variations of hot and cold chambers, corresponding to the driven voltage of hot and cold diaphragms. 99

Figure 5.18 Comparisons of (a) the cooling power density and (b) pressure drop in a frequency range of 1 to 10 Hz between the thermal modeling results and multiphysics modeling results. 99

Figure 6.1 P(VDF-TrFE-CFE) terpolymer film with sputtered gold electrodes. 103

Figure 6.2 Test bed setup for the electrocaloric effect measurement of P(VDF-TrFE-CFE) thin film (joint work with Jinsheng Gao). 104

Figure 6.3 (a) Example of a trapezoidal electric field applied to the EC sample and the measured current. The ramp time of the electric field is 1.2 s and its maximum amplitude is 67 V/μm. (b) Infrascope-measured temperature images at different time in a cycle and the temperature as a function of time. The temperature changes abruptly when the electric field is ramping up and down (2 and 4). 105

Figure 6.4 Measured cooling temperature for CMU and Piezotech samples as a function of the electric field at different voltage ramp times. The stage temperature is 25 ˚C for all measurements. 106

Figure 6.5 Measured temperature profile indicating the thermal time constant and the temperature variation when the electric field changes. 108

Figure 6.6 The comparison between the measured data and the computational result at an electric field of 90 V/μm. 109

Figure 6.7 Adiabatic temperature change vs. electric field and comparison to literature results. 109

Figure 6.8 Measured cooling temperature at different stage temperatures. The ramp time of the voltage is 0.8 s. 110

Figure 6.9 (a) Measured minimum temperature as a function of the operating frequency. (b) Measured temperature change when switching off the electric field with the operating frequency. A ramp time of 0.8 s is fixed at different frequencies for a fair comparison. The stage temperature is 25 ˚C. The inset is a plot of measured temperature when the operating frequency is 0.3 Hz and the electric field amplitude is 73 V/μm. ΔT is the temperature change when switching off the electric field. 111

Figure 6.10 Temperature history of a sample for 30 minutes at a stage temperature of 25 °C. The ramp time of the voltage is 0.8 s. The frequency is 0.2 Hz and the electric field amplitude is 54 V/μm. Gaps in the date are due to limitations of the infrascope, the electric field was modulated at all times. 112

Figure 7.1 (a) Cross section of PDMS diaphragm with embedded electrode fabricated on the gelatin sacrificial layer. (b) Optical microscope photos of the fabricated diaphragm with bonding pad. (c) SEM images of chambers fabricated by grayscale lithography (Courtesy of Jinsheng Gao [103]) 117

Figure 7.2 Solidworks model for electrocaloric cooler and components for assembly. (Courtesy of Andrew Slippey) 118

Figure 7.3 Solidworks model of test bed for the electrocaloric cooler. (Courtesy of Andrew Slippey) ... 118

Nomenclature

A	Convective heat transfer area in the chamber, m^2
A_{min}	Minimum cross-sectional area, m^2
A_w	Wetted area of the pillars, m^2
C_1, C_2, C_3, C_4	Constants
COP	Coefficient of performance
COP_C	Carnot COP
D_h	Hydraulic diameter, m
E	Electric field, V/m
F	Forchheimer coefficient
H	Height, m
K	Permeability, m^4
L	Length, m
M	Amplitude of the mass flow rate, kg/s
MAE	Mean absolute error
M_g	Molar mass of the gas, kg/mol
N	Number of row of pillars
NTU	Number of transfer units
Nu	Nusselt number
Pr	Prandtl number
Q	Heat extraction per cycle, J
$\dot{Q}$	Heat source, W/m^3

R	Ideal gas constant, J/(mol·K)
Re	Reynolds number
S	Entropy, J/(kg·K)
S_L	Longitudinal pitch, m
S_T	Traverse pitch, m
T	Temperature, K
U	Average velocity, m/s
V	Volume, m^3
W	Work, W
Z_{max}	Vibration amplitude of the diaphragm, m
ZT	Figure of merit
a_{fs}	Solid surface area per unit volume, 1/m
c_p	Specific heat, J/(kg·K)
d	Pillar diameter, m
e	Regenerator effectiveness
f	Friction factor
$f_{correlation}$	Friction factor predicted from correlations
f_{exp}	Friction factor from experimental data
h	Convection coefficient, W/(m^2·K)
k	Thermal conductivity, W/(m·K)
m	Mass, kg
$\dot{m}$	Gas mass flow rate, kg/s
n	Number of data points

p	Pressure, Pa
q	Rate of heat transfer, W
q_{cd}	Heat conduction loss across regenerator walls, W
u	Velocity, m/s
$\bar{u}$	Average velocity, m/s
w	Total channel width, m
Δp	Pressure drop through the regenerator, Pa
Δt_1	Transit time, s
Δt_2	Time lag between the electric field and the diaphragm motion, s
δ_t	Thermal penetration depth, m
ε	Porosity
η	Regenerator effectiveness
κ	Swept volume ratio, V_H/V_C
μ	Dynamic viscosity, Pa·s
ρ	Density, kg/m^3
σ	Electrical conductivity, S/m
$\bar{\bar{\tau}}$	Viscous tensor, N/m^2
τ	Gas temperature ratio, $T_{g,H}/T_{g,C}$
φ	Phase angle
χ	Dead volume ratio

Subscripts

C	Cold side
D	Dead space

H	Hot side
g	Gas
$loss$	Loss
max	Maximum value
ns	Non-swept space
out	Outlet
r	Regenerator
s	Solid

Others

$\boldsymbol{n}$	Unit vector normal to the boundary.
$\mathbf{u}$	Velocity vector, m/s
∇	Differential operator, 1/m

Chapter 1 Introduction

1.1 Motivation

Micro-scale refrigeration systems have a wide range of potential applications, such as cooling for integrated circuits, MEMS sensors, radio-frequency electronics, and biomedical devices [1,2]. With the development of MEMS technologies and semiconductors, power consumption has increased significantly while device size has reduced substantially, resulting in an emergent demand on dissipating a high heat density. Novel cooling technologies with a high efficiency are attractive due to growing energy consumption and the requirement of thermal management. The coefficient of performance of the cooler (*COP*), is defined as the ratio of heat removal to the input work [3]. The Carnot coefficient of performance, COP_C, which represents the maximum theoretical efficiency possible between constant temperature hot (T_H) and cold (T_C) sources, can be found from

$$COP_C = T_C / (T_H - T_C). \quad (1.1)$$

In recent years, the Defense Advanced Research Projects Agency (DARPA) has invested extensively to improve the thermal management technologies (TMT) [4] and enhance the cooling capacity and efficiency for the electronics system.

As shown in Fig. 1.1 [4], DARPA TMT program (2008-2013) includes five subprograms: Microtechnologies for Air-Cooled Exchangers (MACE), Thermal Ground Plane (TGP), Nano-Thermal Interfaces (NTI), Near Junction Thermal Transport (NJTT) and Active Cooling Modules (ACM) [4]. Each subprogram is corresponding to a specific task area according to the thermal resistance chain in Fig. 1.1. The MACE program is to develop new technologies to improve the performance of heat sinks by decreasing the thermal resistance. The TGP program is

to achieve superior heat conduction (10 KW/(m·K)-20 KW/(m·K)) by incorporating nanostructured material for thin two-phase chambers at high g-loads (10 g-20 g) operational conditions, while replacing the traditional heat spreader. The goal of NTI program is to reduce the thermal resistance of the interface layers that exist in many places from the electronic device to air by using novel materials and nanostructures. The fourth program NJTT pursued a 3x enhancement in RF power output by providing localized thermal management within 100 μm of the electronic junction. The primary goal of ACM program is developing and demonstrating active cooling of electronics based on novel materials and thermodynamic cycles, to provide about 10 ˚C-25 ˚C of cooling with a cooling power density of 25 W/cm^2 and a coefficient of performance (*COP*) of 2 in the centimeter scale [4]. An efficient active cooling module with a high performance could enable low-temperature operation of the device, including operation below ambient temperature, and allow larger power utilization margins in electronic devices.

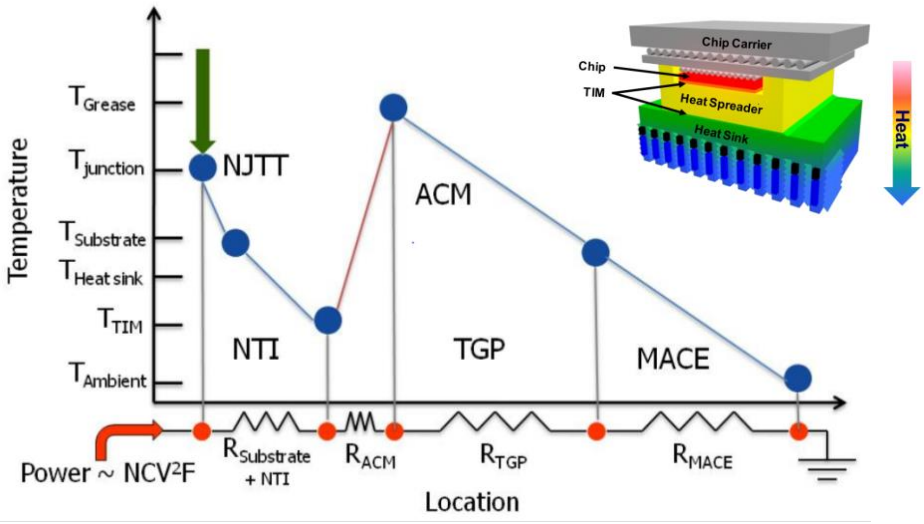

Figure 1.1 A schematic of TMT programs (MACE, TGP, ACM, NTI and NJTT) and the task areas in a representative device [4].

Thermoelectric coolers are a common active refrigeration device and have been scaled to the micro-domain [5-8]. The efficiency of thermoelectric energy conversion is determined by the

thermoelectric material's figure of merit, *ZT*, which is defined by $ZT = S^2\sigma T/k$, where *S*, σ and *k* are the Seebeck coefficient, electrical conductivity, and thermal conductivity [9]. The maximum *COP* of a thermoelectric cooler is [5]

$$COP = \frac{T_C\left(\sqrt{1+ZT}-T_H/T_C\right)}{(T_H-T_C)\left(\sqrt{1+ZT}+1\right)}. \quad (1.2)$$

This maximum *COP* is plotted as a function of the temperature difference T_H-T_C in Fig. 1.2 for *ZT* values of one and two (the latter is the maximum value currently available in bulk thermoelectric materials [5]). For a typical temperature difference of 25 K for cooling in ambient conditions, the maximum *COP* of a realistic thermoelectric cooler is 2.6, which is 24% of the Carnot *COP*. While thermoelectric coolers are gaining traction in applications, significant challenges exist to increase *ZT* beyond unity due to the difficulty of reducing the thermal conductivity while maintaining good electrical properties [10]. The low efficiency and challenges in material fabrication suggest that alternatives are needed.

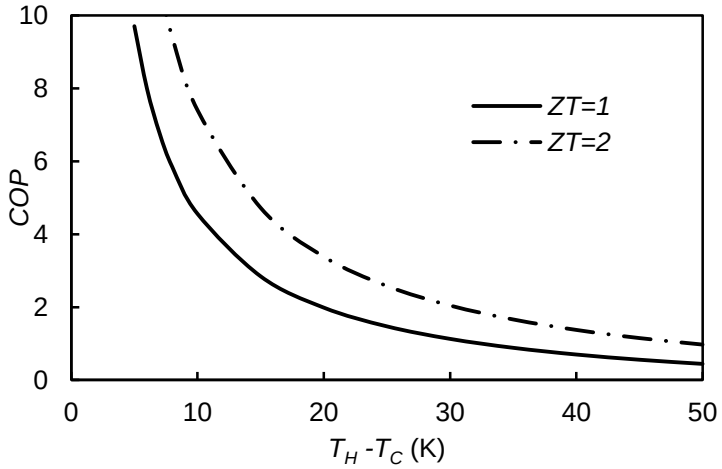

Figure 1.2 Theoretical *COP* as a function the temperature difference T_H-T_C for a thermoelectric cooler.

In this work, alternative options, active refrigeration devices based on Stirling cycle and electrocaloric materials, are investigated to realize a high cooling performance in the centimeter scale. The design concept, the analysis methodology, testing approach and results provide a valuable view insight of these two active cooling technologies and build the foundations for the further explorations.

1.2 Stirling cooling

Micro-scale devices operating on the Stirling cycle, which was developed in 1816 [11], are an attractive potential alternative due to the high efficiencies realized for macro-scale Stirling machines [1]. The traditional mechanical Stirling cooler uses two pistons to transfer the working fluid back and forth between hot and cold chambers that are separated by a regenerator. The heat is released from the hot chamber during the compression process and absorbed from the cold chamber during the expansion process. Ceperley [12] recognized that sound waves can be used to replace the pistons or diaphragms for gas compression and displacement in the Stirling cooler. Thermoacoustic technology based on the Stirling cycle was thus developed. Reid et al. [13], Jin et al. [14], and Symko et al. [15] built thermoacoustic refrigeration systems and applied them in cryogenic cooling. Banjare et al. [16] and Zink et al. [17] performed CFD analysis to demonstrate the principle of the thermally-driven cooling. The temperature gradient achieved due to the thermoacoustic cooling, however, is limited by the critical temperature gradient [18].

Attempts to miniaturize Stirling coolers for application in electronics cooling have been scale-limited by the use of traditional components (e.g., pistons, linkages, and pressure vessels) [18,19]. The state-of-the-art in small, but conventionally manufactured, Stirling coolers is exemplified by an on-board system measuring $13 \times 25 \times 6$ cm^3 in the palm-size titanium infrared imagers made by FLIR [21]. Efforts on a prototype micro-scale Stirling cooler, which are

documented in a series of cryocooler patents [22,23], addressed frictional losses and leakage concerns by replacing the conventional pistons and the associated linkages with electrostatically-driven diaphragms. The Moran concept [23,24] used 1-2 cm diameter silicon diaphragms with vertical electrostatic comb drives to move the working gas through a layered metal/polymer regenerator, as illustrated in Fig. 1.3. The substantial heat loss from the hot side to the cold side is challenging to minimize.

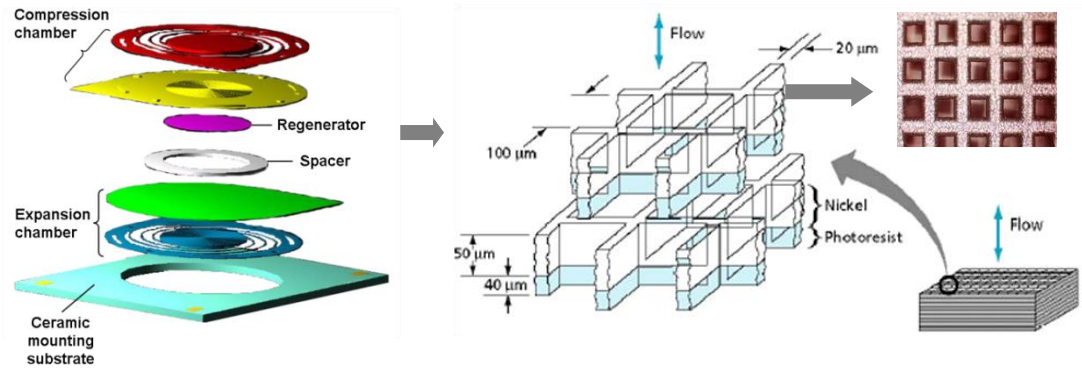

Figure 1.3 The Moran concept [23,24] uses silicon diaphragms with vertical electrostatic comb drives to move the working gas through a regenerator vertically (i.e., perpendicular to the plane of the silicon wafer). Left: Micro-Stirling cooler assembly. Right: Regenerator design showing orthogonal flow between diaphragms.

1.3 Electrocaloric cooling

In recent years, novel solid-state cooling technologies, such as electrocaloric (EC) and magnetocaloric cooling, have attracted interest [25,26]. The electrocaloric effect is a phenomenon in which reversible, polarization-related temperature and entropy changes of material appear under the application and removal of an electric field. As shown in Fig. 1.4, applying the electric field orients the dipoles and reduces the entropy associated with the polarization. This process happens so fast (on the order of milliseconds [27]) that it can be

considered to be adiabatic. The temperature of the material therefore increases, as required by the entropy of material decrease. Reversely, removing the electric field disorders the dipoles, increases the entropy of material, and cools the material. The magnetocaloric effect is similar to the electrocaloric effect, with the use of a magnetic field instead of an electric field. While refrigeration based on the magnetocaloric effect can be employed to achieve extremely low temperatures, miniaturization of devices is challenging while maintaining a high cooling performance.

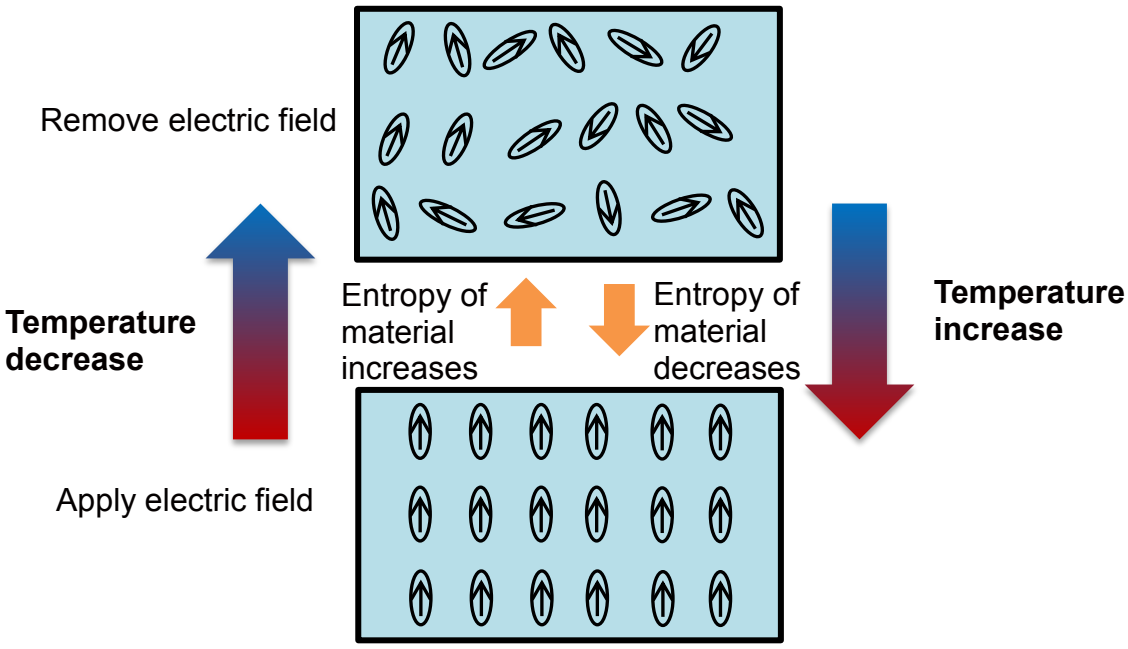

Figure 1.4 Conceptual demonstration of the mechanism of the electrocaloric effect. The material becomes polar-ordered under the electric field and the decreased material entropy increases temperature. When the electric field is removed, the material returns to a polar-disordered state, the material entropy increases, and the temperature drops.

Although the EC effect was first reported by Kobeco and Kurtschatov in 1930 [28], potential applications have been limited by the relatively low entropy and temperature changes for most ferroelectric materials. Recently, materials with a large EC effect have been discovered [29,30], suggesting practical applications in cooling devices.

Jia and Ju [31] proposed a design of a solid-state refrigeration system based on the EC effect where an EC material is dynamically moved by a motorized z-stage between a heat source and a heat sink, as shown in Fig. 1.5. 1 K temperature drop was observed in their experimental testing at a frequency of 0.3 Hz. Reduction of the thermal contact resistances at the interfaces between the EC material and the heat source/sink (which are periodically brought into and out of contact) is challenging in this design. The overall cooling performance is limited by the poor performance of the electrocaloric material $BaTiO_3$.

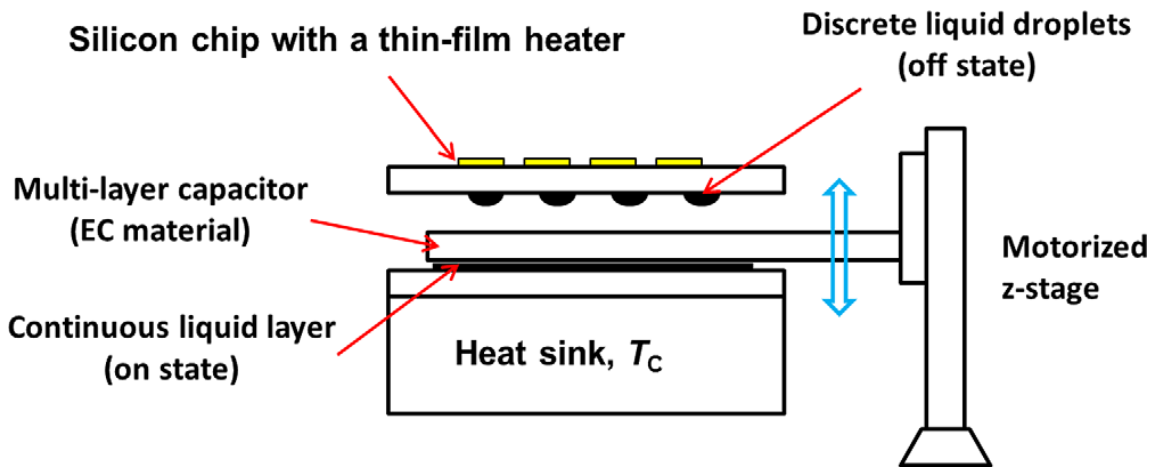

Figure 1.5 Design and setup of a solid-state refrigerator based on the electrocaloric effect (Jia and Ju [31]).

Gu et al. [32,33]reported a chip scale solid-state electrocaloric oscillatory refrigeration device based on the high energy electron irradiated poly (vinylidene fluoridetrifluoroethylene) 68/32 mol% (ei-copolymer), and the prototype cooling device achieved more than 6 K temperature span between the hot and cold sides, as shown in Fig. 1.6. However, the cyclic motion of regenerators in the refrigerator was realized by a step motor, which is not compact and does not satisfy the size requirement for the chip scale cooling. The cooler performance is also limited by the friction loss and the thermal conduction between EC modules and regenerators in this design.

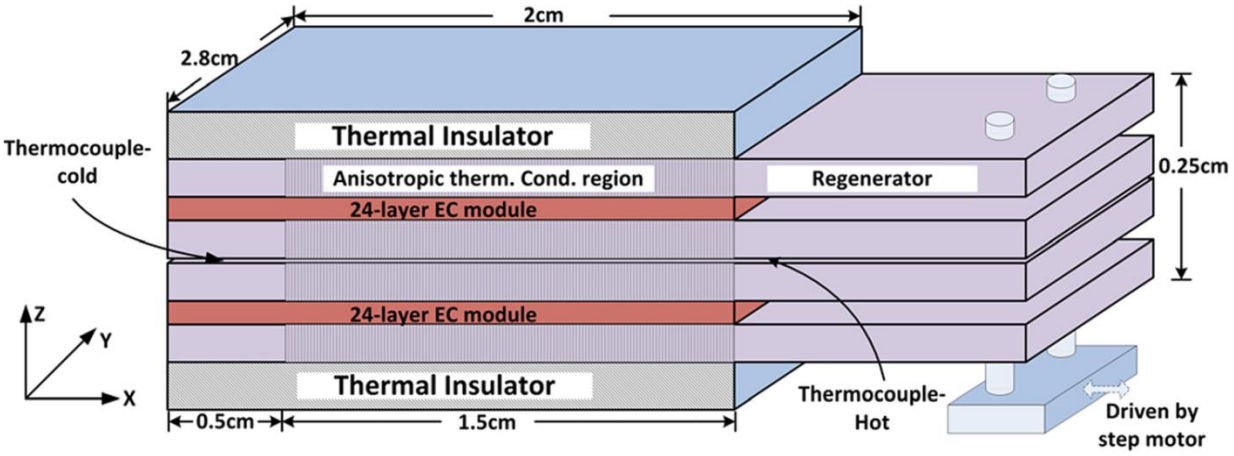

Figure 1.6 Schematic of the prototype of a solid-state electrocaloric cooler (Gu et al. [32]), which includes two 0.25 mm thick 24-layer EC module and four 0.5 mm thick regenerators.

1.4 Thesis overview

This thesis is part of a collaborative work on a DARPA ACM program involving graduate students Jinsheng Gao (electrostatic pump modeling and fabrication) in Department of Electrical and Computer Engineering, and Ying-Ju Yu (EC material molecular dynamics modeling and fabrication, 3D box printing) in Department of Mechanical Engineering and Andrew Slippey (EC cooler performance testing) at Advanced Cooling Technologies, Inc. (ACT). Their contributions are indicated in the corresponding parts of this thesis.

The objective of this thesis is to develop a chip scale refrigeration system for cooling of electronic devices. Due to the high efficiency realized for the conventional scale Stirling cooler, miniaturization of Stirling cooler is presented in this work. In order to minimize the heat loss from the hot side to the cold side of the device, an in-plane design of the system is realized on a silicon wafer. The cooler thermal performance is investigated based on the thermodynamic analysis and finite element modeling. Another option is to develop the refrigeration system based on novel materials, and a fluid-based electrocaloric device is designed in this thesis, which also employs the concept of the in-plane flow. The detailed design and the system performance, including material performance, are explored.

The rest of the thesis is organized as follows. The scaled Stirling cooler was discussed in Chapters 2, 3 and 4. In Chapter 2, a new micro-scale Stirling cooler system, including two diaphragm actuators driven electrostatically and a regenerator on a silicon wafer, was designed [34]. The in-plane micro-scale implementation offers efficient thermal isolation between the hot and cold sides. To achieve a larger heat lift, a large number of cooler elements in this design can be assembled in parallel. A system-level thermodynamic analysis of the Stirling cooler element

was preformed, and sources of inefficiency and losses were analyzed and evaluated by using detailed fluid dynamics and heat transfer analyses.

In Chapter 3, a finite element modeling that incorporates compressible fluid flow, heat transfer, and solid mechanics was used to study the thermal performance of the full system [35]. Firstly the regenerator was isolated and its design was optimized. Then for the system-level estimation, a porous medium model was used to replace the fine pillar structures in the regenerator, allowing for a full-system finite element calculation. The proposed design can achieve a cooling power density of 4.2 W/cm^2 and a system *COP* of 2.93 with a temperature span of 25 K.

The pin fin structures employed by the current regenerator in the Stirling cooler have a significant effect on the cooler performance. The experimental investigation of gas laminar flow across a bank of pin fin arrays was conducted in Chapter 4. The experimental data for circular pin fins were compared with the data of conventional flows, and the existing correlations of friction factor. A new correlation, which considers the coupled effects of the pin fin aspect ratio and pillar spacing, was proposed for predicting the friction factor. The effect of circular pillars with artificial roughness on the friction factor was explored. The creation of roughness on pin fins, which is easily realized by the mask design in lithography process, can be used improve the efficiency of the micro regenerators, micro reactors or other related applications.

The study of fluid-based electrocaloric cooler was presented in Chapters 5 and 6. In Chapter 5, the detailed design of EC cooler was documented [36], which includes two diaphragm pumps and an EC module in between. A heat transfer fluid is sealed within the element and pumped back and forth with the carried heat between hot and cold chambers. Finite element modeling was conducted to evaluate the system thermal performance with an assumption of a

sinusoidal diaphragm motion. Then multiphysics simulations of the system coupled with thermal fluid modeling and modeling of the diaphragm driven by electrostatics were performed. A cooling power density of 3.65 W/cm^2 and a *COP* of 2.5 with a temperature span of 25 K could be achieved based on this novel design. (Jinsheng Gao: joint diaphragm modeling and multiphysics modeling with diaphragm deformations).

The characterization of electrocaloric effect for a thin film of P(VDF-TrFE-CFE) terpolymer was obtained in Chapter 6. The infrared imaging technique was demonstrated to be an effective and convenient method for the thin film measurement. A significant percentage of the adiabatic temperature change (about 50%) was realized, which is much larger than that obtained in other reported measurement techniques. A theoretical correction considering the convection heat transfer between the thin film and the environment was performed to quantify the adiabatic temperature change. The frequency dependence of the EC effect was investigated and the film stability was also studied. (Jinsheng Gao: joint EC material test bed setup, Ying-Ju Yu: EC film fabrication).

A summary of this thesis work and suggestions for future research was presented in Chapter 7.

Chapter 2 Design and thermodynamic analysis of a MEMS-based Stirling microcooler

2.1 Introduction

Micro-scale devices operating on the Stirling cycle are attractive based on the high efficiencies realized for macro-scale Stirling machines, which is about 15 to 25% of Carnot *COP* [37]. However, Stirling coolers have been impractical for most electronic packaging applications due to the use of traditional components (e.g., pistons, linkages, and pressure vessels) [38-41]. Recently, electrostatically-driven diaphragms are employed to replace conventional pistons to pump the gas in the micro-domain [22-24]. In this chapter, a new design of the micro-scale Stirling cooler system, which includes two diaphragms and a regenerator that separates the hot and cold chambers, is presented, as shown in Fig. 2.1. This in-plane micro-scale implementation offers efficient thermal isolation between the hot and cold sides by enabling a longer length regenerator than may be practical in a stacked assembly meant to support gas flow perpendicular to the wafer, as shown in Fig. 1.3.

Classical theories, such as an isothermal model or an adiabatic model, can be applied to analyze Stirling coolers [3]. The isothermal analysis is based on the Schmidt cycle with sinusoidal volume variations. Assumptions are required to obtain a closed form-analytical expression for the cooling power. Notably, the gas temperature in the hot (cold) side is assumed to be the constant and to take on the temperature of the heat sink (source) and the regenerator is assumed to be perfect. The adiabatic analysis is more realistic as the working spaces tend to be adiabatic rather than isothermal in real machines. The adiabatic analysis assumes that the hot and cold spaces are thermally-insulated and that all the heat input and output occur at the heat

exchangers. The gas flows out of the heat exchangers at the heat sink (source) temperature and then comes into the hot (cold) space. The regenerator is also assumed to be perfect.

Martini [42], Wale et al. [43], Lee et al. [44], and Shoureshi [45] included more realistic losses and inefficiencies in the isothermal or adiabatic models. The important losses and inefficiencies in the Stirling cooler devices include: 1) Parasitic regenerator heat conduction, whereby a heat flow develops along the device walls due to the temperature gradient between the hot and cold sides. 2) Due to the finite convection coefficient and limited heat capacity of the regenerator, when the gas flows from the hot side to the cold side, the output gas temperature is higher than the cold space temperature, thus reducing the maximum possible heat transfer. 3) The pressure drop when the gas flows through the regenerator. 4) The finite convection coefficients in the hot and cold exchangers. For different types of Stirling devices, losses and inefficiencies may also exist due to gas leakage, mechanical damping, and electrical effects [1].

In this study, the losses associated with the regenerator (parasitic heat flow, pressure drop, and insufficient heat transfer) and the finite heat transfer in the chambers are incorporated in a system-level model to evaluate the cooling performance of the device. The rest of the chapter is organized as follows. In Section 2.2, the detailed design concept of the new Stirling microcooler is discussed. A system-level thermodynamic analysis of the system is then presented in Section 2.3 and the effects of non-idealities on the cooler performance are quantified in Section 2.4 using detailed fluid dynamics and heat transfer analyses.

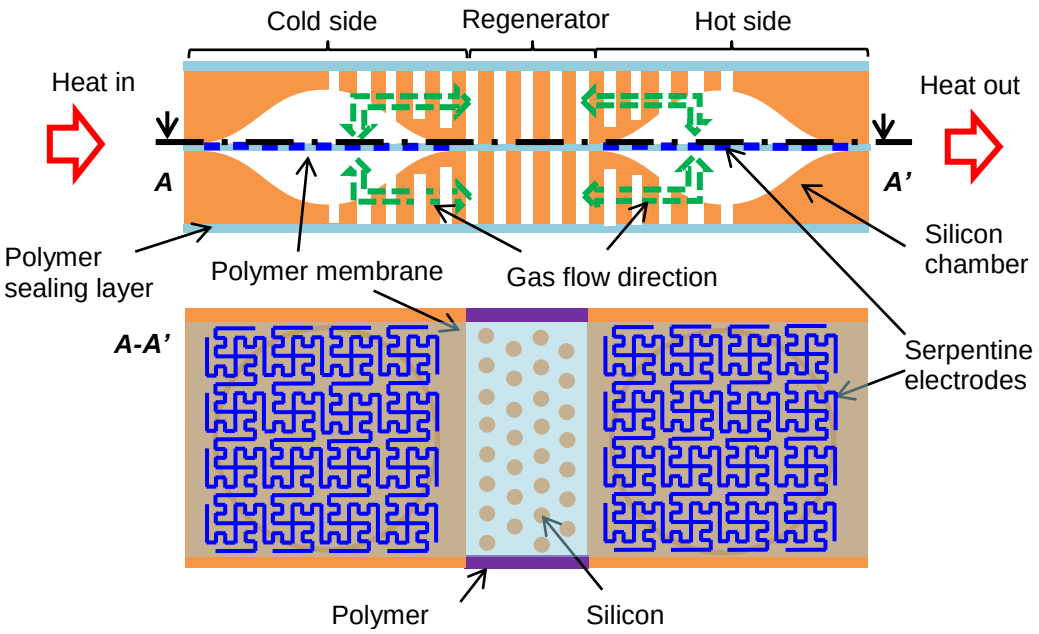

Figure 2.1 The current in-plane micro-scale implementation positions the regenerator flow channel parallel to the wafer plane connecting the compression and expansion chambers, allowing for thermal isolation. Top: Cross-sectional view of Stirling micro cooler elements showing the silicon chamber and the in-plane gas flow direction. Bottom: Planar view (*A-A'*) of the cooler element displaying the polymer membrane with the embedded electrodes and silicon pillars in the regenerator.

2.2 Design concept

2.2.1 Overall concept

The Stirling microcooler elements are each 5 mm-long, 2.5 mm-wide, have a thickness of 150 μm, and are fabricated on a silicon wafer, as illustrated in Fig. 2.2. The design minimizes conduction heat losses across a 0.5 mm-long regenerator by distancing the compressor and expander assemblies with a low thermal conductivity passage. The working fluid is dry air assumed to be the ideal gas in the later analysis, and pressurized at 2 bar. The compression and expansion processes are driven by 2.25 mm diameter circular diaphragms that are actuated electrostatically. The assembled structure is comprised of a pair of identical planar elements

positioned face-to-face, as shown in Fig. 2.1, and has five parts: the diaphragm layer in the middle, the top and bottom chamber substrates, and two sealing layers. Each of these parts is attached with activated bonding of polydimethylsilicone (PDMS) to either silicon or silicon oxide layers. The cooling elements are designed to be arrayed along their width and thickness to create larger-area surfaces with cooling capacity that scales with their cross-section area. For example, the 2 × 2 cm^2 cooling area shown in Fig. 2.3 is made by first arraying eight elements along their width and then stacking 114 of these 1 × 8 arrays. This active cooling module is reduced in volume by three orders of magnitude compared to a standard small-scale (2000 cm^3) Stirling cooler.

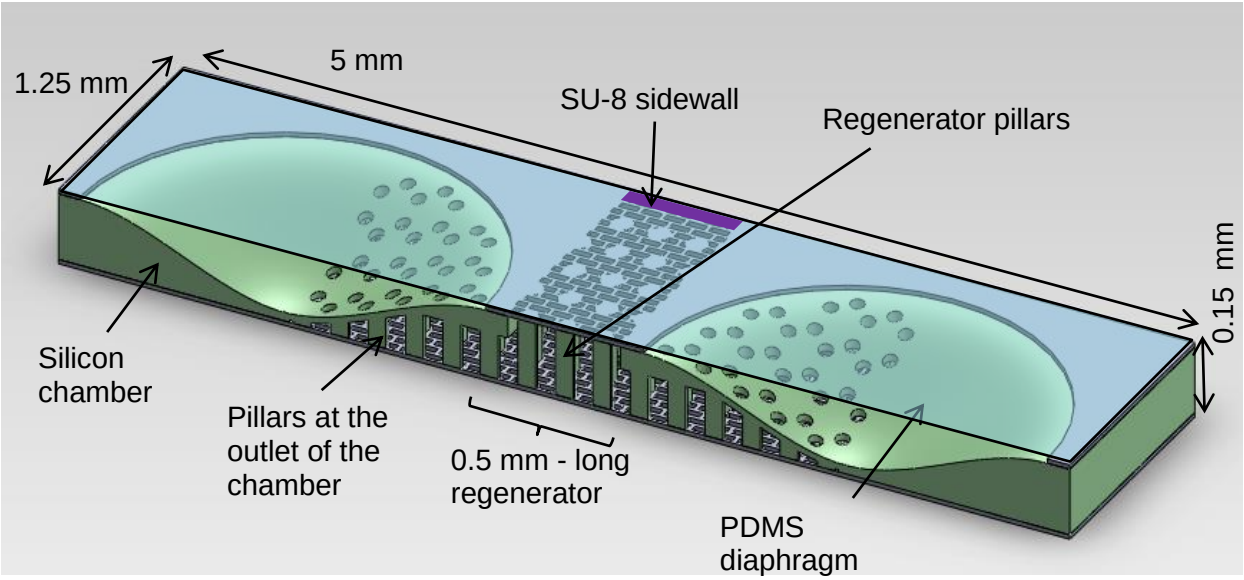

Figure 2.2 Solid-model view of a Stirling microcooler element that is 5 mm-long, 2.5 mm-wide, has a thickness of 150 μm, and is fabricated on a silicon wafer. (Courtesy of Jinsheng Gao [34])

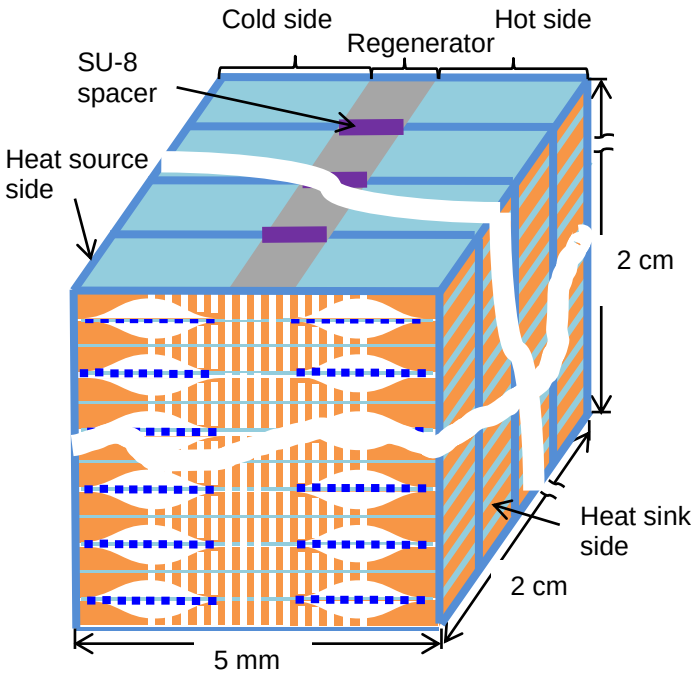

Figure 2.3 Vision of the arrayed Stirling microcooler. A 2 × 2 cm^2 cooling area is made by first arraying eight elements along their width and then stacking 114 of these 1 × 8 arrays.

2.2.2 Hot and cold chambers

Under operating conditions, the hot and cold diaphragms oscillate sinusoidally and out of phase such that heat is extracted from the source (which is at a lower temperature than the sink) to the expansion space and released to the sink (typically the surroundings) from the compression space. The diaphragms are actuated electrostatically to drive the working fluid, which transfers heat between the two chambers. In this design, the bulk silicon substrate on which the device is grown is etched with zipper-shaped chambers under the diaphragms. The silicon substrate enables efficient heat transfer between the gas and heat source/sink and the zipper shape of the substrate reduces the pull-in voltage required to actuate the diaphragms. The addition of silicon pillars at the outlet of each chamber also enhances heat transport from the gas, as shown in Fig. 2.2.

2.2.3 Regenerator

The flow channels of the 0.5 mm-long regenerator are positioned along the wafer plane connecting the compression and expansion chambers. The top and bottom walls of the regenerator are made from thin-film silicon oxide and coated with PDMS. Both materials' thermal conductivities are about one hundred times less than that of silicon. The sidewalls are made from SU-8 epoxy, which also has low thermal conductivity. As a result, the conductive heat leakage from the hot section to the cold section is small (see Section 2.4.2.2). A series of vertical silicon pillars (diameter 20 μm) are fabricated in the regenerator and serve as the thermal capacitor, which enables efficient heat transfer to/from the gas as it passes through.

2.2.4 High-frequency operation

The cooling capacity of a Stirling cooler is directly related to its operating frequency. Small thermal penetration depths make high frequency-regenerators impractical in large coolers. In microcoolers, however, high-frequency operation is possible, as the length scales of the components of the regenerator can be made comparable to the thermal penetration depth, δ_t, which is given by [46],

$$\delta_t = \sqrt{\frac{k}{\pi f \rho c_p}}, \tag{2.1}$$

where k is the thermal conductivity of the silicon, f is the operating frequency, ρ is the silicon density and c_p is the specific heat of the silicon. At an operating frequency of 2 kHz, the thermal penetration depth in silicon is 122 μm at a temperature of 20˚C. Therefore, the diameters of the pillars in the regenerator should thus not exceed 122 μm. Much smaller feature sizes (down to about 20 μm) are accessible though micro-fabrication.

2.3 Thermodynamic analysis of the system

2.3.1 Stirling cycle

The basic Stirling cooling concept employs pumps (either pistons or diaphragms) to drive a working fluid between a cold region and a hot region across a regenerative heat exchanger (i.e., the regenerator). The operation of an ideal Stirling refrigeration cycle is illustrated in Fig. 2.4. Also shown are the corresponding pressure-volume and temperature-entropy diagrams. The ideal cycle starts with an isothermal compression of the working gas from states 1 to 2 that increases the pressure and decreases the gas volume, thereby sending heat to the surrounding chamber. The gas is then cooled in a constant volume process as it is forced through the regenerator into the expansion space (states 2 to 3) while dumping the heat to the regenerator. From states 3 to 4, the working gas is expanded in an isothermal process that decreases the pressure and increases the gas volume, thereby extracting heat from the surrounding chamber. The cycle returns to its original state (states 4 to 1) with the gas absorbing heat from the regenerator. During steady-state operation, this cycle produces a cold region by extracting heat in the expansion space for cooling and a hot region by releasing heat in the compression space. In reality, the Stirling refrigerator will not operate as an ideal cycle, but rather in a sinusoidal-like motion with a phase lag between the cold and hot sides.

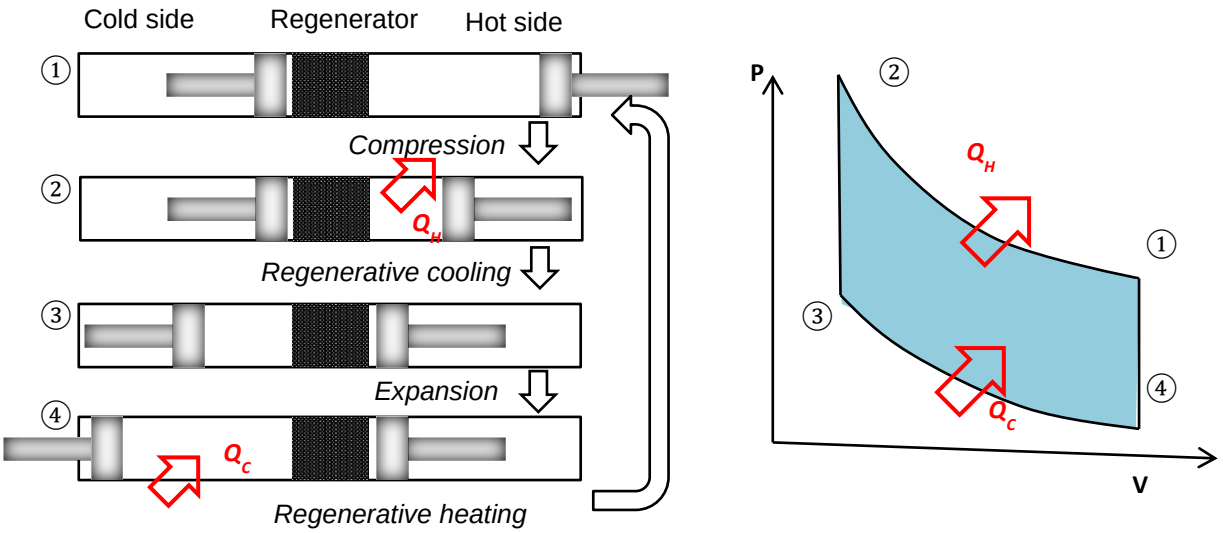

Figure 2.4 The ideal Stirling refrigeration cycle includes four processes: isothermal compression (1-2), regenerative cooling (2-3), isothermal expansion (3-4) and regenerative heating (4-1).

2.3.2 Thermodynamic analysis of the Stirling cycle

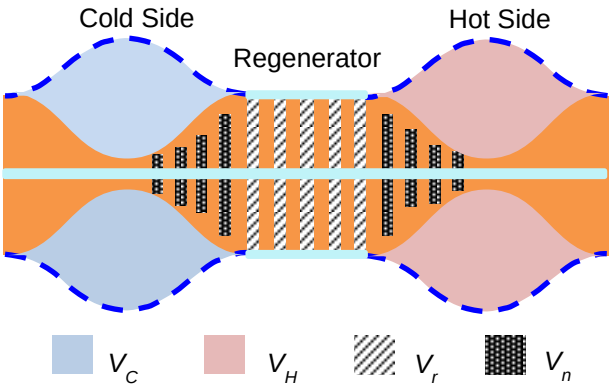

Figure 2.5 Geometric parameters for a microcooler element. The dead volume, V_D, includes the regenerator volume, V_r, and the non-swept volume between the regenerator and the chambers, V_{ns}. V_C and V_H are the swept volume in the cold and hot chambers.

In a cooler driven by the Stirling cycle, the dead volume ratio and the swept volume ratio between the two chambers play an important role in determining the cooling capacity [3]. The dead volume, V_D, includes the regenerator volume, V_r, and the non-swept volume between the regenerator and the chambers, V_{ns}. These volumes are shown in Fig. 2.5. V_C and V_H, which are also shown in Fig. 2.5, are the swept volume of the cold and hot chambers. $\kappa = V_H/V_C$, is the swept volume ratio, and $\chi = V_D/V_C$ is the dead volume ratio. In order to understand the effects of these volume-related parameters on the Stirling cooler, its performance can be approximated with a first-order analysis without considering any losses in the system.

Several assumptions are made during this procedure. We assume that the regenerator is perfect, such that at the outlet of the regenerator, the gas temperature is the same as the chamber temperature (i.e., the regenerator effectiveness is unity). The pressure, p, in the system at any point in time is uniform. The gas temperature in each chamber is uniform and constant, and the temperature profile in the dead space is linear. If the phase lag between the cold side and the hot side is α, then the volume variation of the cold space as a function of the phase angle φ, is

$$V_c = \frac{1}{2} V_C (1 + \cos \varphi), \tag{2.2}$$

and the volume variation of the hot space is

$$V_h = \frac{1}{2} V_H [1 + \cos(\varphi - \alpha)]. \tag{2.3}$$

The total mass of the working fluid in the system, m, is constant, so that, using the ideal gas law,

$$\frac{mR}{p} = \frac{V_c}{T_{g,C}} + \frac{V_h}{T_{g,H}} + \frac{V_D}{T_{g,D}}, \tag{2.4}$$

where $T_{g,C}$ is the average cold gas temperature and $T_{g,H}$ is the average hot gas temperature. The mean temperature in the dead space, $T_{g,D}$, is

$$T_{g,D} = \frac{1}{2}(T_{g,H} + T_{g,C}). \tag{2.5}$$

The expansion and compression processes take place isothermally, so that the heat released or absorbed in each chamber is equal to the work, such that

$$Q = \int p dV. \tag{2.6}$$

Based on Eqs. (2.2)-(2.6), the variation of the system pressure as a function of the phase angle φ is

$$p = \frac{p_{max}(1-\delta)}{1+\delta\cos(\varphi-\theta)}. \tag{2.7}$$

Using Eqs. (2.6) and (2.7), the heat extracted by the gas in the cold chamber per cycle is then

$$Q_C = \frac{\pi\delta\sin\theta\sqrt{1-\delta}}{(1+\kappa)\sqrt{1+\delta}\left(1+\sqrt{1-\delta^2}\right)} p_{max}(V_C + V_H). \tag{2.8}$$

The heat released by in the hot chamber per cycle is

$$Q_H = \tau Q_C. \tag{2.9}$$

In Eqs. (2.7)-(2.9), p_{max} is the maxmium pressure, δ is an intermediate variable,

$$\delta = \frac{\sqrt{\tau^2+\kappa^2+2\tau\kappa\cos\alpha}}{\tau+\kappa+2S}, \tag{2.10}$$

where τ is the gas temperature ratio,

$$\tau = T_{g,H}/T_{g,C}\ , \tag{2.11}$$

and S is the reduced dead volume,

$$S = 2\tau\chi/(1+\tau). \tag{2.12}$$

The variable

$$\theta = \tan^{-1}\left(\frac{\kappa\sin\alpha}{\tau+\kappa\cos\alpha}\right), \tag{2.13}$$

can be interpreted as the lead phase angle of the volume variation in the cold side to the pressure variation in the element. If the initial pressure in the system is p_0, then the maximum pressure in the system is obtained, based on Eq. (2.7), to be

$$p_{max} = p_0\frac{1+\kappa+2\chi}{1+\kappa+2\chi-\sin\alpha}\frac{1-\delta\sin(\alpha-\theta)}{1-\delta}. \tag{2.14}$$

From Eqs. (2.8) and (2.14), the dimensionless heat extraction Q_C^* is

$$Q_C^* = \frac{Q_C}{p_0(V_C+V_H)} = \frac{\pi\delta\sin\theta[1-\delta\sin(\alpha-\theta)]}{(1+\kappa)\sqrt{1-\delta^2}\left(1+\sqrt{1-\delta^2}\right)}\frac{1+\kappa+2\chi}{1+\kappa+2\chi-\sin\alpha}. \tag{2.15}$$

For a 25 K temperature lift, $T_{g,H}$ =313.15 K and $T_{g,C}$=288.15 K, the dimensionless heat extraction per cycle is a function of the swept volume ratio κ, the phase lag between the cold side and the hot side α, and the dead volume ratio χ. For the dead volume, we fix the regenerator volume and study the effect of varying the non-swept volume. Note that the non-swept volume ratio is

$$\chi_{V_{ns}} = V_{ns}/V_C. \tag{2.16}$$

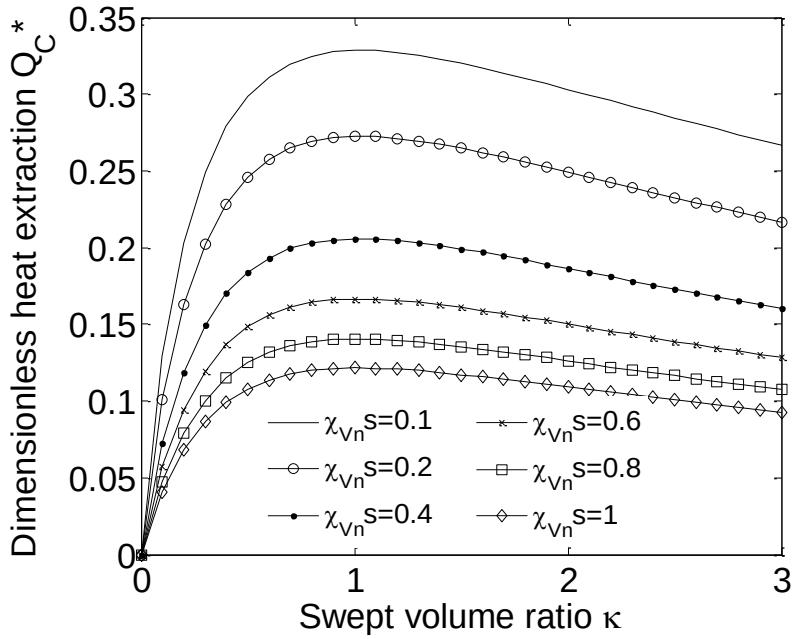

(a)

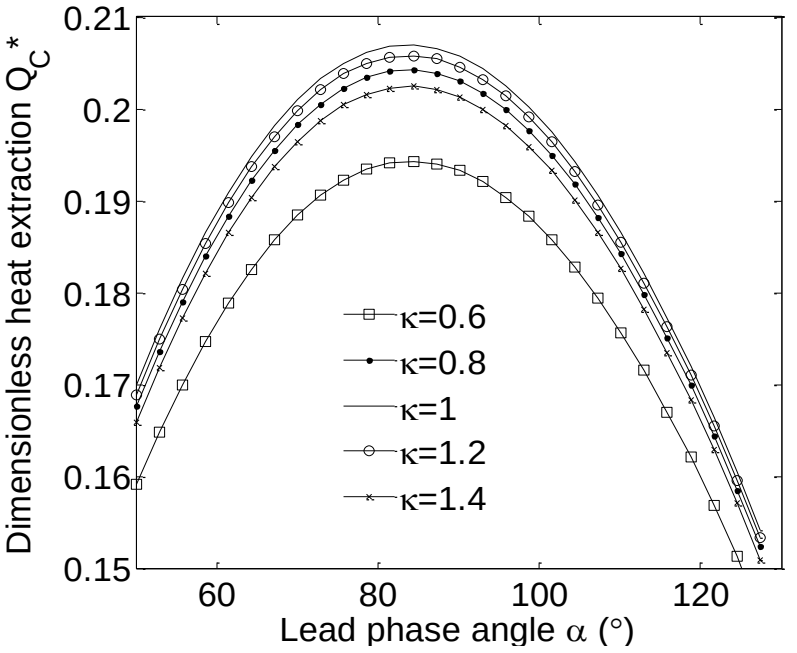

(b)

Figure 2.6 (a) Dimensionless heat extraction as a function of swept volume ratio for different non-swept volume ratios. The lead phase angle of the cold side to the hot side is 90°. (b) Dimensionless heat extraction as a function of lead phase angle for different swept volume ratios. The non-swept volume ratio is 0.4.

In Fig. 2.6, the dimensionless heat extraction per cycle based on variation of κ, α and $\chi_{V_{ns}}$ is plotted. In Fig. 2.6(a), the effect of the swept volume ratio κ on the dimensionless heat extraction at different non-swept volume ratios when the lead phase angle of the cold side to the hot side is 90° is shown. The curves show that an optimum value of κ can be found at which the dimensionless heat extraction is maximized. This optimum value of κ is always unity for this concept, which corresponds to the cold side and hot side having the same swept volume. The same swept volumes maximize the heat extracted or released in the cold or hot chamber. The effect of the non-swept volume ratio is clear from Fig. 2.6(a): with an increase of $\chi_{V_{ns}}$, the dimensionless heat extraction decreases. This result indicates that the non-swept volume should, as expected, be as small as possible. In Fig. 2.6(b), the effect of lead phase angle α on the dimensionless heat extraction at different swept volume ratios when the non-swept volume ratio is 0.4 is plotted. From this figure, we can see that the dimensionless heat extraction varies by only ±10% when the lead phase angle is in the range of 60° to 110°.

2.4 System-level loss evaluation

2.4.1 Coefficient of performance

In Section 2.3, we assumed that the system was perfect and did not consider any losses. In the real system, however, non-idealities will be present and their effects are now considered. Note that in Section 2.3 we use Q to represent the heat extraction per cycle. Here we use q as the rate of the heat transfer. We start with the coefficient of performance (*COP*) of the cooler, which is the ratio of the heat removal to the input work,

$$COP = \frac{q}{w}, \tag{2.17}$$

The Carnot coefficient of performance COP_C, which represents the maximum theoretical efficiency possible between constant temperature heat source (T_C) and heat sink (T_H), is defined as Eq. (1.1). For T_H =313.15 K and T_C =288.15 K, COP_C is 11.5.

An estimate of the actual coefficient of performance requires knowledge of the real work input and the heat loss. In our design, the losses come from: (i) Convective heat transfer resistance between the silicon substrate and the gas in the chamber, (ii) Heat conduction along the regenerator walls, (iii) Insufficient heat transfer in the regenerator, and (iv) Pressure drop through the regenerator.

2.4.2 Energy balance

To estimate the actual cooling power q of the system, a simplified model is built and an energy balance is made. As shown in Fig. 2.7, the regenerator is not perfect, so the gas in the cold side not only absorbs heat from the heat source, but also gets some heat from the gas coming out of the regenerator, q_r. Along the regenerator walls, there is heat conduction loss from the hot side to the cold side, q_{cd}. Combining these losses, we obtain an energy balance for the cold chamber

$$q_C = q + q_{cd} + q_r, \tag{2.18}$$

where q_C is total heat absorbed by the cold gas when the cold gas space expands. It can be calculated from Eq. (2.8). Similarly, for the hot chamber,

$$q_H = q_h + q_{cd} + q_r, \tag{2.19}$$

where q_h is the actual heat rate coming out of the hot chamber and q_H is total heat rate released by the hot gas when the hot gas space is compressed. It can be calculated from Eq. (2.9).

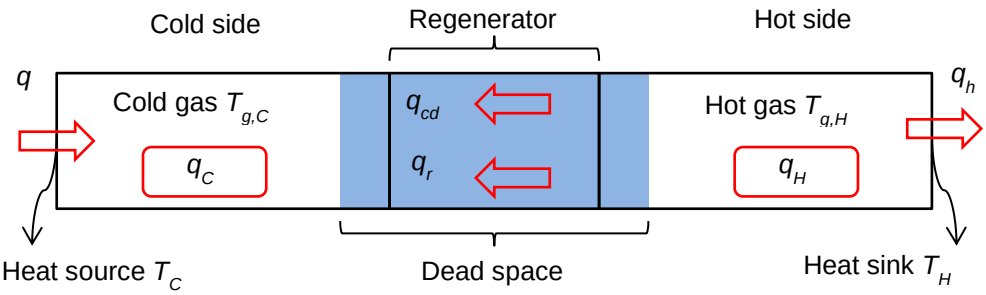

Figure 2.7 System sketch of the single Stirling microcooler element and the energy balance in each chamber. $T_{g,C}$ and $T_{g,H}$ are the gas temperature in the cold and hot chambers. The heat source temperature is T_C and the heat sink temperature is T_H.

2.4.2.1 Heat transfer in the chamber

The heat source temperature is T_C, the heat sink temperature is T_H, the convection coefficient between the cold/hot chamber and the heat source/sink is h, and the surface area between them is A. Due to the high thermal conductivity of silicon, we assume the substrate in each chamber is isothermal. Then, the actural cooling power for the system is

$$q = hA(T_C - T_{g,C}). \tag{2.20}$$

In the hot chamber, the heat coming out of the hot chamber is

$$q_h = hA(T_{g,H} - T_H). \tag{2.21}$$

$T_{g,C}$ and $T_{g,H}$ are the gas temperature in the cold and hot chambers. The convection coefficient in the chamber is obtained from the finite element simulation of the Stirling microcooler system [35]. The Nusselt number used for the calculation is

$$Nu = 0.316Re^{0.31}. \quad (2.22)$$

In the range of the present operating frequency (100 Hz ~ 1000 Hz), the Reynolds number range is about 10 ~ 100. As the chamber structure is complex, here the hydrailic diameter is used for the Nusselt number and Reynolds number.

2.4.2.2 Regenerator heat conduction

The top and bottom walls of the regenerator are made from thin-film silicon oxide and coated with PDMS. The sidewalls are made from SU-8. All these materials have low thermal conductivity: k_{SiO_2} =1.4 W/(m·K), k_{SU-8} =0.3 W/(m·K) and k_{PDMS} =0.2 W/(m·K) at a temperature of 20˚C. The thicknesses of thin-film silicon oxide, SU-8, and PDMS are 2 μm, 50 μm and 12 μm. As a result, the heat conduction loss q_{cd} is

$$q_{cd} = \sum_{i=1}^{3} k_i A_{c_i} \frac{T_{g,H} - T_{g,C}}{L_r}, \quad (2.23)$$

where i =1, 2, 3 represent the three different materials, A_c is the cross-sectional area, which is the thickness multiplied by the width of the regenerator wall, and L_r is the regenerator length.

2.4.2.3 Regenerator ineffectiveness

As the regenerator is not perfect, the temperature of the gas leaving the regenerator will not be the chamber temperature. Thus, the heat required to raise the gas temperature is

$$q_r = (1 - e)\dot{m}c_p\left(T_{g,H} - T_{g,C}\right), \quad (2.24)$$

where $\dot{m}$ is the average mass flow rate in the cooler and e is the regenerator effectiveness. As a first-order estimation, the *NTU* method is used here to estimate the regenerator effectiveness [47]. *NTU*, which is the number of transfer units, is a dimensionless parameter that is widely

used for heat exchanger analysis and it is defined as

$$NTU = \frac{h_r A_w}{\dot{m} c_p}, \tag{2.25}$$

where h_r is the convection coefficient in the regenerator, and A_w is the wetted area in the regenerator. From an energy balance (i.e., setting the change of the gas enthalpy equal to the heat transfer between the gas and the regenerator), we obtain the regenerator effectiveness to be [48]

$$e = \frac{NTU}{1+NTU}. \tag{2.26}$$

The convection coefficient of the regenerator pillars with the gas can be estimated according to Zukauskas's correlation which is widely recognized by the researchers [49],

$$Nu_d = 0.9 {Re_d}^{0.4} Pr^{0.36}, (10 < Re_d < 100). \tag{2.27}$$

The Nusselt number and Reynolds number are defined as

$$Nu_d = \frac{h_{fs} d}{k}, \tag{2.28}$$

and

$$Re_d = \frac{\rho u_{max} d}{\mu}, \tag{2.29}$$

where u_{max} is the maximum velocity through the regenerator, μ is the dynamics viscosity, and Pr is the Prandtl number. *d* is the pillar diameter, which is 20 μm in our design.

Predictions of the regenerator effectiveness from the *NTU* method and from finite element simulations [35] for regenerator porosities of 0.798, 0.864, and 0.916 are presented in Table 2.1. In the present regenerator, the Knudsen number is less than 0.01. The continuum theory is used for the FEA simulations. The maximum difference between the analytical model

and the detailed numerical calculations is less than 5%, justifying the *NTU* method as a simple and useful tool for predicting the regenerator effectiveness. From the result, we can see that the regenerator effectiveness decreases with an increase of the operating frequency and increases with a decrease of the porosity. At a high frequency, the heat transfer between the solid and the gas is limited due to the small interaction time. When the porosity is large, the solid-gas interface area is small and the regenerator effectiveness is poor.

Table 2.1 Comparison of the regenerator effectiveness at different operating frequencies from an analytical model [Eq. (2.26)] and finite element simulations [35]. When the porosity is 0.798, 0.864, or 0.916, the maximum difference between the two predictions is less than 5%, giving confidence to the use of the much simpler analytical model.

	Frequency (Hz)	FEA [35]	*NTU* [Eq. (2.26)]	Error (%)
ε=0.798	100	0.908	0.941	3.6
	200	0.900	0.914	1.6
	400	0.895	0.875	2.2
	800	0.854	0.822	3.7
	1000	0.833	0.802	3.7
ε=0.864	100	0.892	0.911	2.1
	200	0.884	0.872	1.4
	400	0.847	0.817	3.5
	800	0.776	0.747	3.7
	1000	0.746	0.721	3.4
ε=0.916	100	0.871	0.857	1.6
	200	0.833	0.800	4.0
	400	0.760	0.732	3.7
	800	0.657	0.632	3.8
	1000	0.620	0.600	3.2

2.4.2.4 Regenerator pressure drop

The work loss due to the pressure drop across the regenerator, W_{loss}, is modeled as

$$W_{loss} = \Delta p f (V_C + V_H), \tag{2.30}$$

where Δp is the pressure drop through the regenerator. To predict the pressure drop in the regenerator (which is a microchannel containing a pillar matrix), a porous medium model is used in a FEA simulation [35]. The relationship between the pressure drop and the gas velocity is then correlated by the permeability K and Forchheimer coefficient F [50-52]. The one-dimensional Darcy-Forchheimer equation is

$$\frac{\Delta p}{L} = \left(\frac{d^2}{K} + F\ Re_d\right)\frac{\mu U}{d^2}, \tag{2.31}$$

where U is the average velocity. Lee [53] proposed a correlation of the Darcy drag $\frac{d^2}{K}$ and the Forchheimer coefficient F for a bank of the cylinders, given by

$$\frac{d^2}{K} = \frac{31(1-\varepsilon)^{1.3}}{\varepsilon^3(\varepsilon-0.2146)}, \tag{2.32}$$

$$F = \frac{(1-\varepsilon)^{1.4}}{\varepsilon^3(\varepsilon-0.2146)}\sum_{n=1}^{3}\sum_{m=1}^{3}\overline{\overline{a_{mn}}}\varepsilon^{m-1}{Re_d}^{n-1}, \tag{2.33}$$

where

$$\overline{\overline{a_{mn}}} = \begin{bmatrix} 4.825 & -0.166 & 0.001777 \\ -17.754 & 0.5893 & -0.00616 \\ 15.911 & -0.4736 & 0.004836 \end{bmatrix}, \tag{2.34}$$

and ε is the regenerator porosity.

The predictions of the pressure drop from Lee's correlation and from the FEA simulation [35] are shown in Table 2.2. The maximum difference is less than 15%, indicating that the correlation of Lee provides a good estimate to the full system behavior. The pressure drop increases with increasing frequency and decreasing porosity. The higher frequency makes the velocity higher and the pressure drop also increases. Decreasing porosity also increases the velocity and increase the contact area at the same time, leading to a higher pressure drop.

Table 2.2 Comparison of the pressure drop through the regenerator at different operating frequencies calculated from an analytical model [Eqs. (2.31)-(2.34)] and FEA simulations [35]. When the porosity is 0.798, 0.864, or 0.916, the maximum difference does not exceed 15%, giving confidence to the use of the much simpler analytical model.

	Frequency (Hz)	FEA (Pa) [35]	Eqs. (2.31)-(2.34) (Pa)	Error (%)
ε=0.798	100	135.2	153.1	13.2
	200	278.5	313.1	12.4
	400	601.5	654.1	8.7
	800	1375.1	1420.6	3.3
	1000	1816.9	1864.6	2.6
ε=0.864	100	58.4	62.6	7.2
	200	122.7	130.3	6.2
	400	269.9	280.2	3.8
	800	619.9	634.7	2.4
	1000	820.9	837.5	2.0
ε=0.916	100	23.8	24.8	4.2
	200	50.9	52.0	2.2
	400	113.0	113.4	0.4
	800	263.2	261.6	0.6
	1000	350.8	346.9	2.0

2.4.3 System evaluation

Using the results from Sections 2.4.2, the cold gas and the hot gas temperature can be obtained by an iterative calculation by combining Eqs. (2.8), (2.9) and (2.18)-(2.26). If the gas temperature is known, then the actual cooling power of the cooler is obtained from Eq.(2.20). The work loss is calculated from Eqs.(2.30)-(2.34). Then, the actual *COP* of the system can be estimated using Eq. (2.17). Here, our goal is to examine the effects of the regenerator porosity and the operating frequency on the system performance. The porosity of the non-swept space between the regenerator and the chamber space is fixed at 0.89. Based on the parametric study described in Section 2.3, the swept volume ratio is unity and the phase lag of the volume variations between the cold side and the hot side is set to 90°.

The system *COP* as a function of the regenerator porosity at different operating frequencies is plotted in Fig. 2.8(a). For a given frequency, an optimal porosity exists that maximizes the *COP*. This value is different at different frequencies. Generally, the porosity range of 0.8~0.9 gives the best efficiency for the micro-cooler. For the same porosity, the *COP* will always decrease with increasing frequency, as the heat transfer efficiency of the regenerator is reduced and the flow resistance through the regenerator increases. Both of these factors hurt the *COP*. When the operating frequency is 200 Hz, the *COP* of the system could be 6.27; however, the best *COP* is only 2.46 when the frequency is 1000 Hz. If the frequency is less than 600 Hz, then the best *COP* could be higher than 3, which is near to 30% percent of the Carnot *COP*.

Although the *COP* is low at a high frequency, with an increase of the frequency, the cooling capacity will increase. The system cooling capacity as a function of operating frequency at different regenerator porosities is shown in Fig. 2.8(b). The cooling capacity increases when

the porosity decreases. One reason for this trend is that the dead volume ratio decreases when the regenerator porosity decreases. Another reason is due to a decrease in the regenerator heat loss, as the regenerator effectiveness increases with decreasing the porosity.

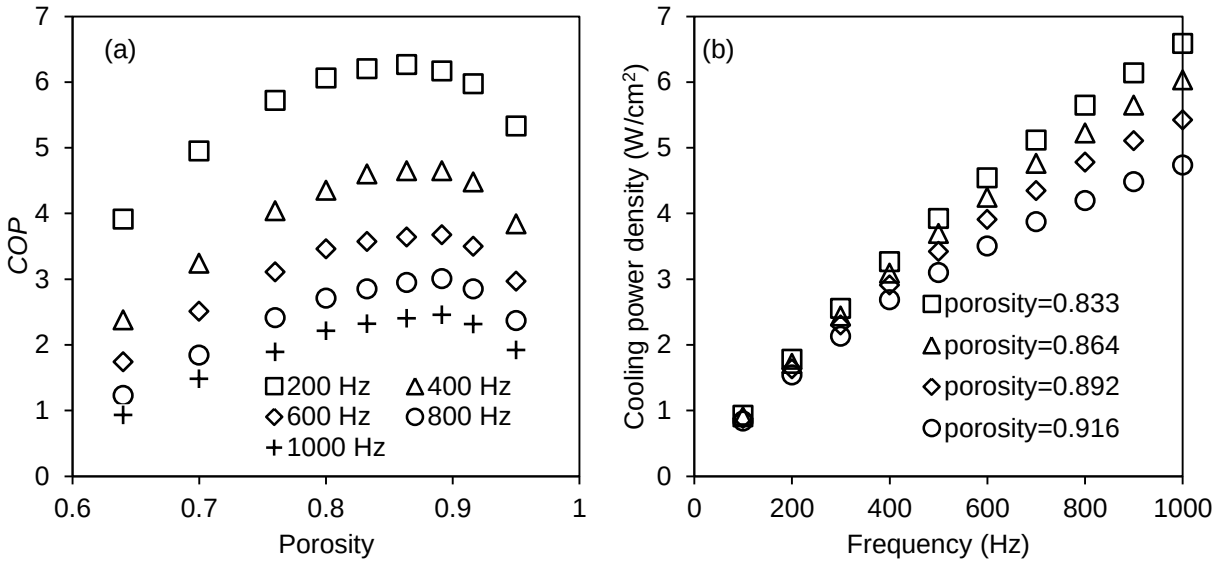

Figure 2.8 (a) System *COP* as a function of regenerator porosity at different operating frequencies. The swept volume ratio is unity for the two chambers and the phase lag of the volume variations between the cold and hot sides is 90°. (b) System cooling power density as a function of the operating frequency at different porosities. The swept volume ratio is unity for the two chambers and the phase lag of the volume variations between the cold and hot sides is 90°.

In Fig. 2.9, the system *COP* and cooling power density with different losses are plotted. As shown in (a) and (b), the regenerator porosity is 0.864. For the ideal system, the *COP* is a constant, 11.5, and the cooling power density is a linear profile with the increase of frequency. For "perfect chamber", the heat transfer in the hot and cold chamber is assumed perfect, that means the heat transfer coefficient between the chamber and gas domain is infinite. Thus these results only consider the heat losses in the regenerator (including the heat conduction loss of regenerator walls) and the pressure loss of gas flows. Comparing the results with different losses, we found at low operating frequency, the effect of the chamber heat loss on *COP* is almost same

with that of the regenerator loss. When the operating frequency is high, the regenerator loss effect on *COP* becomes more significant. This is due to the high friction loss at a high frequency.

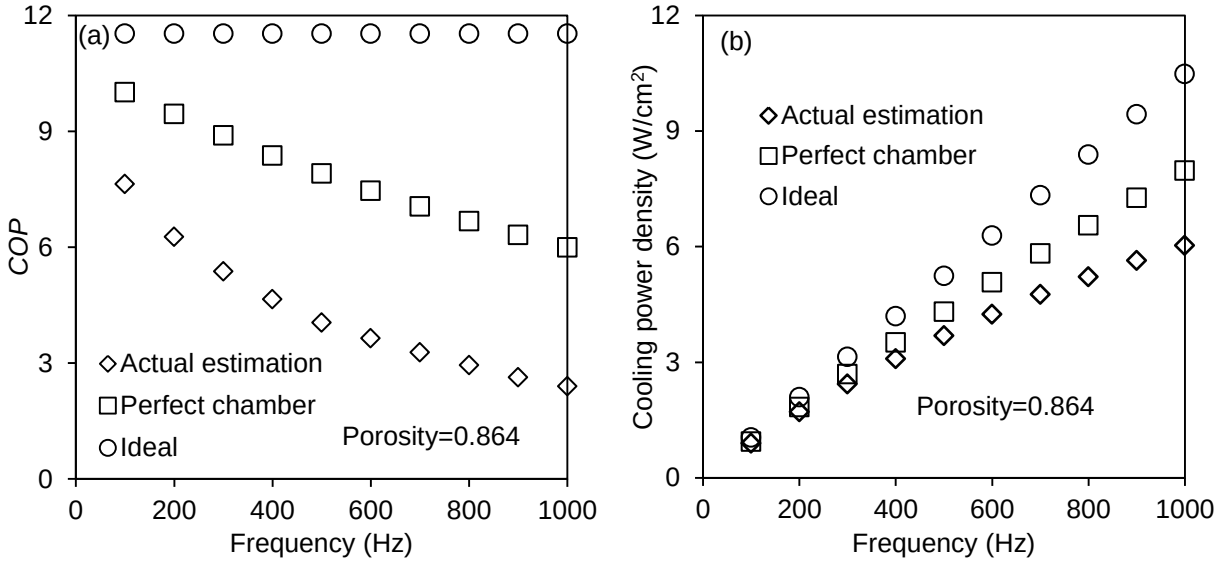

Figure 2.9 System *COP* and cooling power density as a function of frequency with different losses. The swept volume ratio is unity for the two chambers and the phase lag of the volume variations between the cold and hot sides is 90°. (a) *COP* (b) Cooling power density at $\varepsilon = 0.864$.

2.5 Work recovery of the system

It is demonstrated that the Stirling machines operated on Stirling cycle have a high efficiency in the conventional scale. The reason of the realized high efficiency is that there is a hard connection (e.g. the crankshaft) between the hot and the cold actuators (e.g. pistons). Then the work in the cold side can be recorved to the hot side, and the net work of the Stirling cooler system is very small, which is far less than the work for each side. The thermal evaluation in the above analysis also assumed the cold side work is recorved. However, in the micro-scale system, such as the current cooler design, diaphragms (e.g. polymer membranes) are used to drive the gas. It is challenging to make a work recovery from the cold side to the hot side since the mechanical recovery is not favorable here. Some other technologies, such as resonance

phonomenon of diaphragms and energy harvesting circuits, have to be employed to recover this cold side work, or the Stilring micro-cooler efficiency will be low.

2.6 Summary

In this chapter, a new Stirling micro-scale cooler element has been designed and evaluated. The in-plane design, described in Section 2.2, separates the hot and cold chambers by a regenerator and the gas flow direction is within the plane of the wafer, which provides an excellent thermal isolation.

A thermodynamic analysis of the system and parametric studies of geometrical parameters were described in Section 2.3. As shown in Fig. 2.6, to improve the cooling power, the dead volume should be minimized, the swept volume ratio for the two chambers should be unity, and the phase lag of the volume variations between the cold side and the hot side should be 90°.

In Section 2.4, an analytic method was developed and applied to estimate the effects of system non-idealities (specifically related to the regenerator) on the coefficient of performance. The effects of the regenerator porosity and the operating frequency on the cooler performance were then studied. As shown in Figs. 2.8, increasing the frequency reduces the *COP* of the system while increases its cooling power density, and the optimal porosity for the *COP* is 0.8~0.9. The regenerator loss effect on system *COP* becomes more significant with the increase of the frequency.

In Section 2.5, it is indicated that the work recovery of the system is challenging to realize for the current cooler design.

Chapter 3 Multiphysics modeling of the micro Stirling refrigeration system

3.1 Introduction

In Chapter 2, the design of a new micro-scale Stirling cooler system, which includes two diaphragms and a regenerator that separates the hot and cold chambers, is presented. A first-order thermodynamic analysis was performed to evaluate the system performance. A parametric study showed the effects of diaphragm phase lag, swept volume ratio between the hot space and cold space, and dead volume ratio on the cooling performance. For the Stirling micro-cooler, modeling challenges arise mainly from the complicated geometrical structures, (e.g., the large number of pillars in the regenerator) and complex dynamics (e.g., the motion of the diaphragms). We herein address these issues.

In this chapter, the losses associated with the regenerator (parasitic heat flow, pressure drop, and insufficient heat transfer) are discussed and more detailed numerical modeling that incorporates compressible fluid flow, heat transfer, and solid mechanics in a system-level model to evaluate the cooling performance of the device. COMSOL [54], a multiphysics simulation software package, is used to perform the calculations.

The rest of this paper is organized as follows. In Section 3.2, the regenerator is isolated and its design is optimized, with a focus on sources of inefficiency and losses. The full system performance is then evaluated in Section 3.3.

3.2 Regenerator analysis

Estimating the *COP* requires knowledge of the real work input and the heat transfer inefficiencies. In this design, inefficiencies come from the convective heat transfer resistance

between the silicon substrate and the gas in the chamber, the insufficient heat transfer in the regenerator (i.e., the regenerator effectiveness is not unity), and the extra work required to overcome the pressure drop through the regenerator. The regenerator is thus a critical component of the Stirling cooler. Before performing the system-level modeling, the regenerator is first modeled to determine how its complicated geometry can be optimized. In this part of the analysis, the gas temperatures in the chambers are assumed to be the same as the heat source/sink temperatures.

The purpose of the regenerator is to store and release heat from/to the gas during the cycling. The regenerator design has the following requirements [55]: 1) A maximum ratio of the regenerator heat capacity to the gas heat capacity. 2) A maximum heat transfer between the gas and the regenerator, requiring a large contact area. 3) A minimum pressure drop across the regenerator. 4) Complete penetration of the heat in the regenerator material when it is heated or cooled. This last requirement can be achieved by using a solid material with small characteristic dimensions. As discussed in Chapter 2, circular silicon pillars with a diameter of 20 μm are used for the regenerator solid structure due to the limitations of the heat penetration and available fabrication processes.

Finite element analysis of two-dimensional fluid flow is used to analyze the arrangement of the pillars in the regenerator (of particular interest is the porosity) in order to balance the effects of the pressure drop and heat transfer. If inefficiencies reduce the heat transfer by Q_{loss} and the work loss due to the pressure drop is W_{loss}, combining the ideal system cooling power and the work calculated by the isothermal model leads to a system *COP* of

$$COP = \frac{Q - Q_{loss}}{W + W_{loss}}. \tag{3.1}$$

The computational domain and boundary conditions are illustrated in Fig. 3.1. Taking advantage of symmetry, we only need to consider half of an array. The horizontal and vertical pitches are S_L and S_T. The total length of the regenerator, L_r, is 0.5 mm. The width of the studied section is $S_T/2$, which corresponds to a slice of the much wider regenerator. The air flows back and forth between the hot and the cold sides. The mass flow rate at the hot-side surface is taken to be

$$\dot{m} = \dot{M}\sin(2\pi f t), \tag{3.2}$$

where

$$\dot{M} = \pi\rho f S_T V_H / 2H_r. \tag{3.3}$$

$\dot{M}$ is the mass flow rate amplitude, H_r is the regenerator height, and V_H is the volume of the hot gas space, which is 0.48 mm^3. The volume of the chamber space is larger than the regenerator volume, which is 0.17 mm^3 when the porosity of the regenerator is unity. The no-slip condition is applied at the gas-solid interfaces. The hot-side surface temperature condition is

$$\begin{cases} T_H = 313.15 \text{ K if } \mathbf{u}\cdot\mathbf{n} < 0 \\ \nabla T\cdot\mathbf{n} = 0 \text{ if } \mathbf{u}\cdot\mathbf{n} \geq 0. \end{cases} \tag{3.4}$$

The cold-side temperature condition is

$$\begin{cases} T_C = 288.15 \text{ K if } \mathbf{u}\cdot\mathbf{n} < 0 \\ \nabla T\cdot\mathbf{n} = 0 \text{ if } \mathbf{u}\cdot\mathbf{n} \geq 0. \end{cases} \tag{3.5}$$

Here, **u** is the velocity vector and **n** is the unit vector normal to the boundary, as defined in Fig. 3.1. When the fluid flows out from the cold/hot side, the temperature is the heat source/sink temperature T_C / T_H.

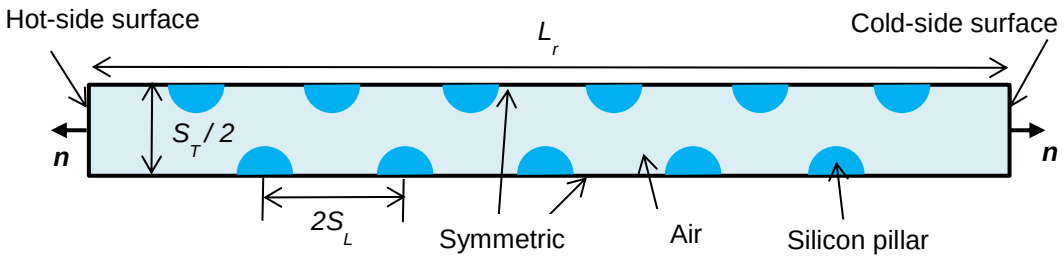

Figure 3.1 Two-dimensional regenerator computational domain and boundary conditions for the porosity optimization study (see also Table 3.1). The horizontal pitch is S_L and the vertical pitch is S_T. The regenerator length is L.

Different porosities are obtained by adjusting the number of pillars, N, and their pitch. To assess the sensitivity of the results to the geometry, two S_L / S_T ratios are considered, as shown in Table 3.1. ε is the regenerator porosity. The time-averaged pressure drop across the regenerator per cycle, Δp, and the actual cold-side surface temperature, T_{out}, are obtained from the simulation results. The effectiveness of the regenerator is calculated from

$$\eta = (T_H - T_{out})/(T_H - T_C). \tag{3.6}$$

Table 3.1 Regenerator pillar configurations used in porosity optimization study.

S_L / S_T	N	$S_T / 2$ (μm)	ε
0.289	13	65.7	0.938
	15	56.3	0.916
	17	49.3	0.892
	19	43.8	0.864
	21	39.4	0.833
	23	35.8	0.798
0.866	8	37.5	0.933
	9	32.8	0.914
	10	29.2	0.892
	11	26.3	0.868
	12	23.9	0.842
	13	21.9	0.813

3.2.1 Fluid compressibility

Due to the pressure variations in the Stirling cooler (1.5 - 2.8 bar), fluid compressibility effects may be important. Most of the air properties relevant to this study do not change significantly within this pressure range (e.g., specific heat, thermal conductivity, and dynamic viscosity [56]). Only the density change is significant. Before performing the regenerator optimization, it should be determined whether compressibility effects need to be included. For the compressible flow, the air is assumed to be ideal, and the equation of state of a classical ideal gas is used to calculate density. The gas pressure as a function of time is calculated based on the isothermal model and is in the range of 1.5 - 2.8 bar. For the incompressible flow, the gas pressure is set to 2 bar. The gas pressure is specified at the cold-side surface of the computation domain. The operating-frequency-dependent pressure drop through the regenerator and the

regenerator effectiveness are plotted in Figs. 3.2(a) and 3.2(b) for both the compressible and incompressible flows. From the results, the effect of compressibility on the flow and heat transfer in the regenerator is small. Therefore an incompressible flow computation for the optimization analysis of the regenerator was used.

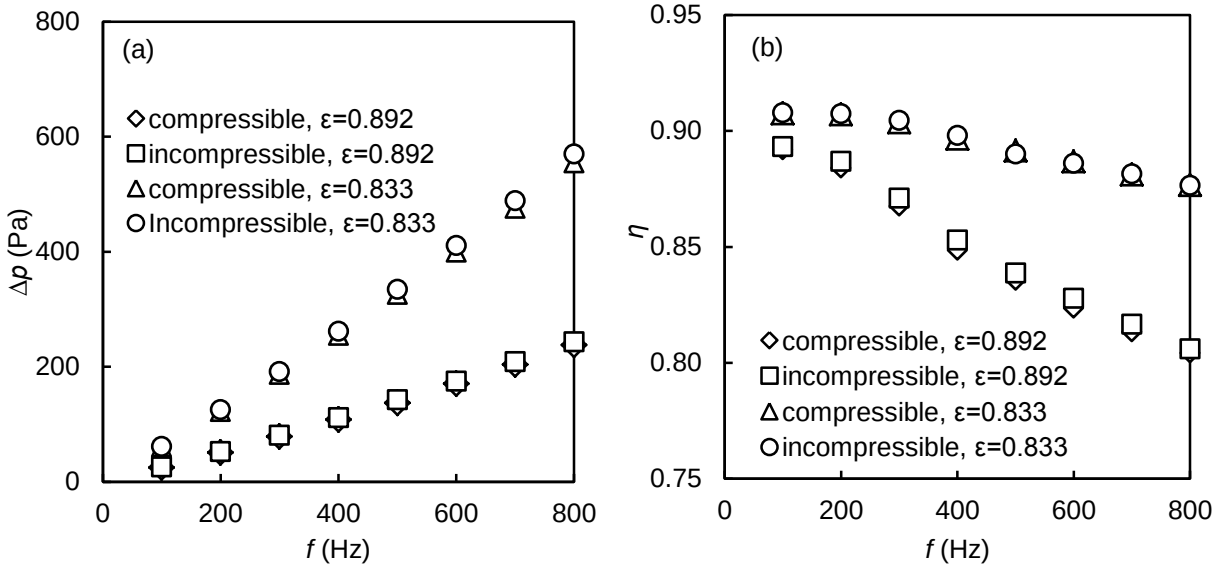

Figure 3.2 Frequency-dependence of (a) time-averaged pressure drop across the regenerator and (b) regenerator effectiveness for S_L / S_T = 0.289 and ε = 0.892 and 0.833. The differences between considering compressible or incompressible flow are small.

3.2.2 Porosity optimization

With T_H = 313.15 K and T_C = 288.15 K, the Carnot *COP* is 11.5. The regenerator pressure drop and effectiveness as a function of the porosity and operating frequency are plotted in Figs. 3.3(a) and 3.3(b).

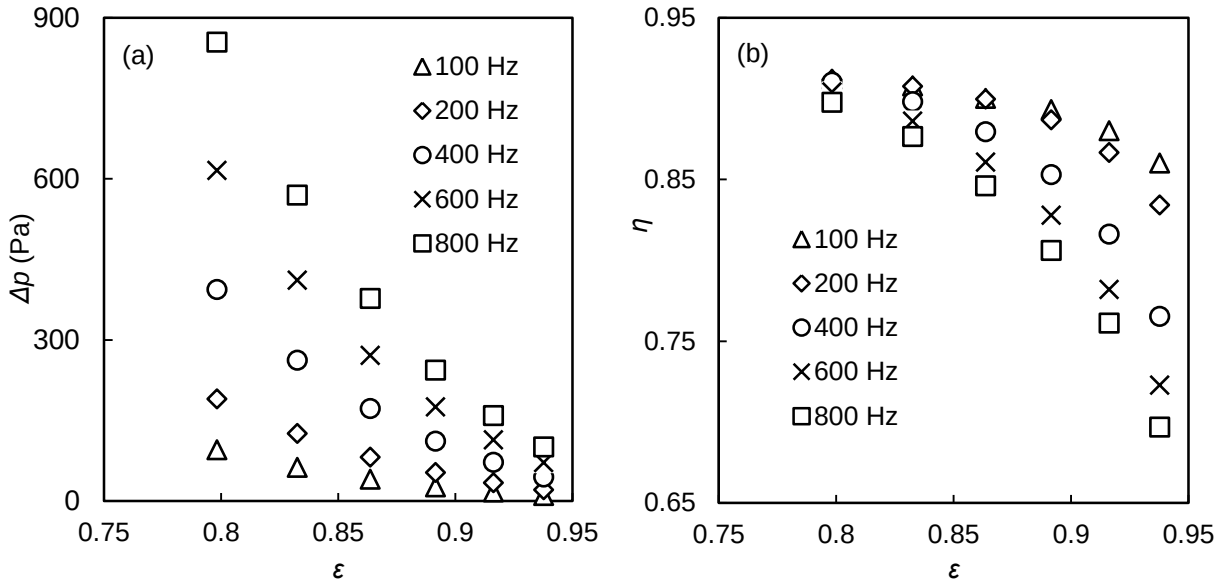

Figure 3.3 Effect of operating frequency and porosity for S_L / S_T = 0.289 on (a) time-averaged pressure drop across the regenerator and (b) regenerator effectiveness.

The work loss per cycle is

$$W_{loss} = 2\Delta p \cdot V_C. \tag{3.7}$$

The insufficient heat transfer loss per cycle is

$$Q_{loss} = (1-\eta) \times (c_p m)_g \times (T_H - T_C). \tag{3.8}$$

Here, *m* is the maximum gas mass in the hot chamber. Using Eq. (3.1), the actual *COP* is plotted in Figs. 3.4(a) and 3.4(b) for two different pitch ratios.

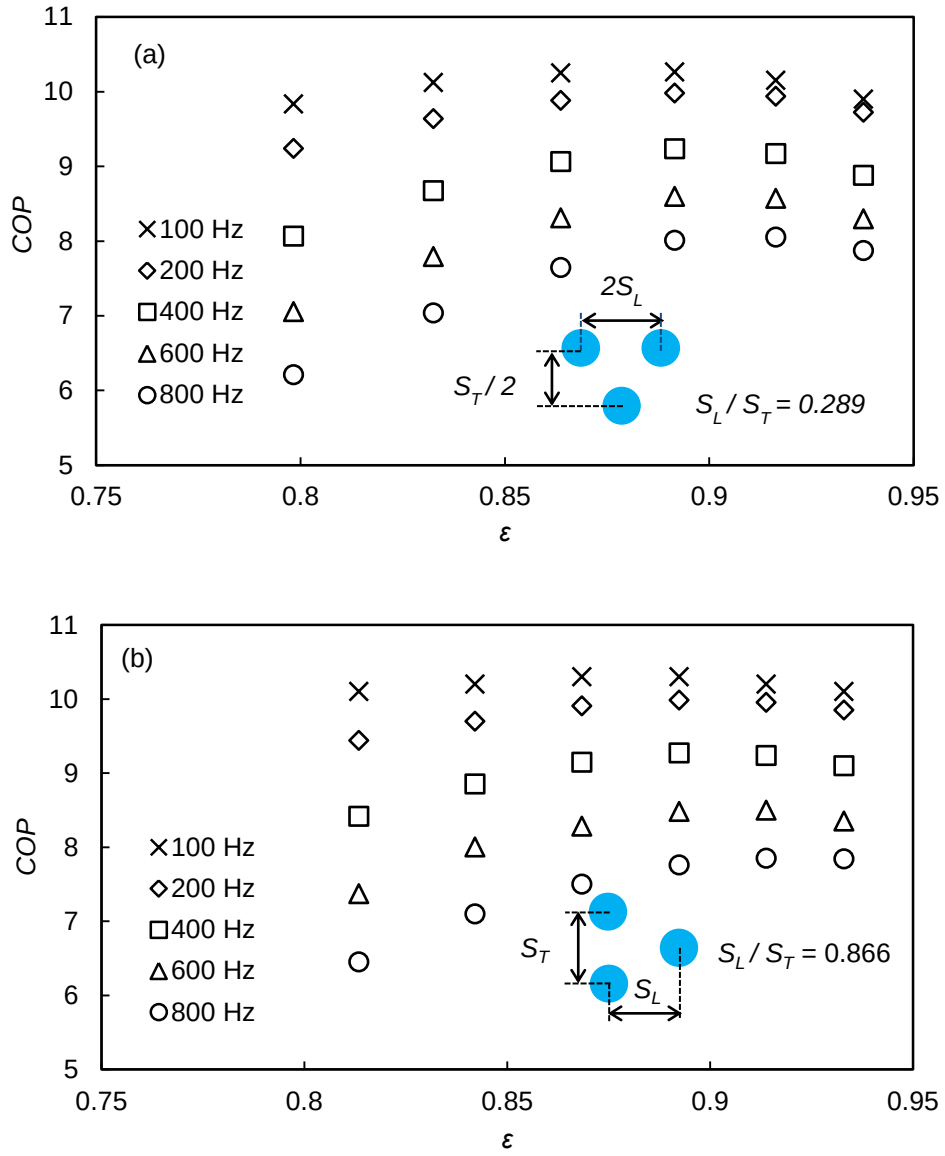

Figure 3.4 Predicted *COP* as a function of operating frequency and porosity for (a) $S_L / S_T = 0.289$ and (b) $S_L / S_T = 0.866$.

The results in Fig. 3.3 indicate that the pressure drop increases with decreasing porosity and increasing frequency, and that the heat transfer between the solid and the gas decreases with increasing porosity and frequency. An optimal porosity, as seen in Fig. 3.4, exists due to the large work loss at small porosities and the large heat transfer loss at high porosities. Even though the arrangements of the regenerator are significantly different ($S_L / S_T = 0.289$ and 0.866), the

optimal porosity is always near 0.9. Therefore, the key parameter in the regenerator that affects the system *COP* is the porosity. We note that the *COP* at $S_L / S_T = 0.289$ is slightly bigger than that at $S_L / S_T = 0.866$ at higher frequency. As the gas temperatures in the chambers are assumed to be the same as the heat source/sink temperatures, meaning that the convection coefficients in the chambers are taken to be infinite, the *COPs* obtained here are overestimated.

3.3 System evaluation

In the previous section, the micro-Stirling cooler regenerator was modeled and it was found that the optimal porosity is near 0.9. In this section, a porosity of 0.892 at $S_L / S_T = 0.289$ was chosen as a case study and the full system performance was evaluated. It is not computationally feasible to build a model that includes the full details of the regenerator geometry (i.e., all the pillars). To overcome the computational complexity brought about by the fine pillar structure in the regenerator and in the dead space, a porous medium model was used to replace the pillars, allowing for a full-system finite element calculation.

3.3.1 Porous medium governing equations

As the Stirling cooler works by gas expansion and compression processes, the main physics in the system are the compressible laminar flow and heat transfer. In the porous medium region, a non-equilibrium model is used [57]. The governing equations for the gas phase are

$$\frac{\partial \rho}{\partial t} + \frac{\nabla \cdot (\rho \mathbf{u})}{\varepsilon} = 0, \tag{3.9}$$

$$\frac{\rho}{\varepsilon}\left[\frac{\partial \mathbf{u}}{\partial t} + (\mathbf{u} \cdot \nabla)\frac{\mathbf{u}}{\varepsilon}\right] = -\nabla p - \frac{\nabla \cdot \bar{\bar{\tau}}}{\varepsilon} - \left(\frac{\mu}{\kappa} + \beta_F |\mathbf{u}|\right)\mathbf{u}, \tag{3.10}$$

$$\rho c_p \left[\varepsilon \frac{\partial T}{\partial t} + (\mathbf{u} \cdot \nabla)T\right] = \nabla \cdot (\mathrm{k}\nabla T) + \frac{\bar{\bar{\tau}}:\nabla \mathbf{u}}{\varepsilon} + \varepsilon \frac{Dp}{Dt} + h_{fs} a_{fs}(T_s - T). \quad (3.11)$$

Here p is the pressure, μ is the dynamic viscosity, κ is the permeability, β_F is the Forchheimer coefficient, T_s is the solid temperature, h_{fs} is the convection coefficient between the solid and the fluid, and a_{fs} is the solid surface area per unit volume, and $\bar{\bar{\tau}}$ is the viscous tensor,

$$\bar{\bar{\tau}} = \mu[\nabla \mathbf{u} + (\nabla \mathbf{u})^T] - \frac{2}{3}\mu(\nabla \cdot \mathbf{u}). \quad (3.12)$$

Assuming the gas to be ideal, the state equation is

$$\rho = \frac{pM_g}{RT}, \quad (3.13)$$

where *R* is the ideal gas constant and M_g is the molar mass.

In the solid phase, the energy equation is

$$(1-\varepsilon)\rho_s c_{p_s} \frac{\partial T_s}{\partial t} = \nabla \cdot \left(\overline{\overline{k_e}} \cdot \nabla T_s\right) - h_{fs} a_{fs}(T_s - T), \quad (3.14)$$

where ρ_s and c_{p_s} are the density and specific heat of the solid. $\overline{\overline{k_e}}$ is the effective thermal conductivity tensor of the solid phase in the porous medium.

3.3.2 Specifying the permeability and Forchheimer coefficient

The permeability κ and Forchheimer coefficient β_F can be obtained based on the one-dimensional Darcy-Forchheimer equation [58], which is

$$-\frac{\partial p}{\partial x} = \frac{\mu}{\kappa} u + \beta_F u^2. \quad (3.15)$$

The relationship between the pressure drop and the velocity for the regenerator with pillars is obtained by steady-state simulation and is plotted in Fig. 3.5(a). The permeability and Forchheimer coefficient are then calculated by the least squares method according to Eq. (3.15), which is also plotted in Fig. 3.5(a). The best-fit permeability is 9.77×10^{-11} m^2 and the best-fit Forchheimer coefficient is 9823 kg/m^4.

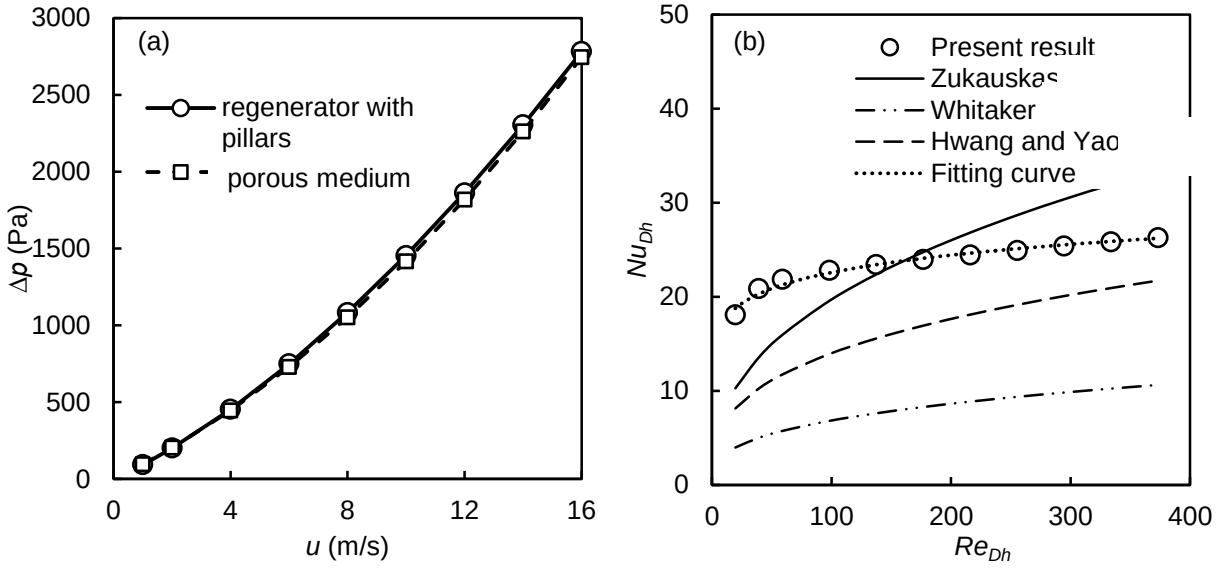

Figure 3.5 (a) Pressure drop across the regenerator as a function of average fluid velocity between (i) the full pillars structure and (ii) the porous medium model. (b) Regenerator Nusselt number as a function of Reynolds number for the current calculations and from existing correlations [49,59,60]. The current simulation results are used for the system modeling.

3.3.3 Convection coefficient

The convection coefficient of the regenerator is also evaluated from steady-state simulations. The Nusselt number and Reynolds number are defined as

$$Nu_{D_h} = \frac{h_{fs} D_h}{k}, \tag{3.16}$$

$$Re_{D_h} = \frac{\rho \bar{u} D_h}{\mu}, \tag{3.17}$$

where

$$D_h = \frac{4\varepsilon}{a_{fs}}. \tag{3.18}$$

D_h is the hydraulic diameter and $\bar{u}$ is the average velocity through the regenerator. The flow in the system is laminar as the Reynolds number in the regenerator is smaller than 200. The Nusselt number is calculated using the log-mean temperature difference when a constant temperature is applied to the pillar walls and is plotted in Fig. 3.5(b). Fitting the raw data gives

$$Nu_{D_h} = 13.389\ {Re_{D_h}}^{0.1135}, \tag{3.19}$$

which is used for the system modeling. Some available experimental correlations [49,59,60] of the Nusselt number for a tube bank are plotted in Fig. 3.5(b). These correlations focus on the flow in a larger Reynolds number range (Re_{D_h}>300 in the present study). The convection coefficient is also influenced by the arrangement of pillars in the regenerator. Thus, differences between the calculation results and correlations are observed.

3.3.4 Computational domain and boundary conditions

The computational domain for the full system model is shown in Fig. 3.6. The porous medium was used to replace the regenerator and the dead-space structure. For the solid phase of the porous medium in the dead space, an isotropic thermal conductivity $(1-\varepsilon)k_{silicon}$ is assumed. The thermal conductivity of the solid phase in the regenerator is anisotropic due to the vertical array of silicon pillars, as illustrated in Fig. 2.2. The out-of-plane thermal conductivity is the same as that of the porous medium of the dead space. The in-plane thermal conductivity is taken to be that of air.

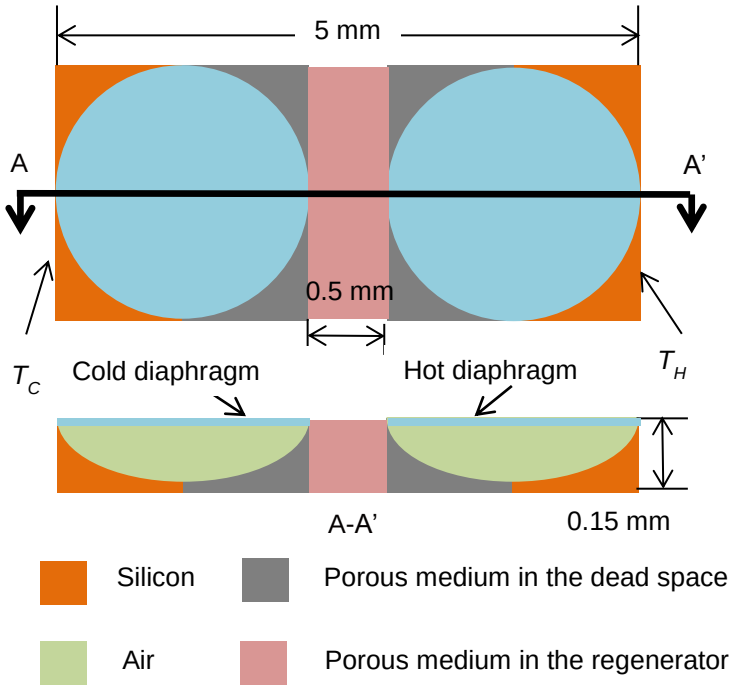

Figure 3.6 Computational domain and geometry for the three-dimensional full-system model. The hot and cold diaphragms, which have a 90° phase lag, prescribe the moving boundaries of the fluid flow. The regenerator and the dead space are replaced by the porous medium.

As the diaphragms are driven electrostatically, their actual motions are complicated and require detailed study. To simplify the model and the analysis, a sinusoidal motion with a 90° phase lag is applied for the cold and hot diaphragms. The displacement of the cold diaphragm is

$$z(x,y,t) = Z_{max}(x,y)\sin(2\pi f t). \tag{3.20}$$

The displacement of the hot diaphragm is

$$z(x,y,t) = Z_{max}(x,y)\sin\left(2\pi f t - \frac{\pi}{2}\right), \tag{3.21}$$

where f is the operating frequency and $Z_{max}(x,y)$ is the vibration amplitude of the diaphragm. The gas space in the chamber is assumed to be a spherical cap. The cap base is a circle with a 2.25 mm diameter and the maximum height of the cap is 120 μm. So, $Z_{max}(x,y)$ represents the

cap height at different positions. The hot and cold diaphragms prescribe the moving boundaries of the fluid flow. The arbitrary Lagrangian-Eulerian (ALE) moving-mesh method [61] was used to handle the gas domain where there is a mesh deformation. The no-slip condition is applied to the solid-gas interfaces. The initial pressure in the system is 2 bar. The temperature of the end surface of the cold side is constant and is T_C = 288.15 K. The end surface in the hot side has a constant temperature of T_H = 313.15 K. The remaining surfaces are thermally insulated. The initial temperature for the whole region is 293.15 K. The number of mesh elements for the system model is 347,773. Parallel computation was performed by using 4 nodes, each of which has 16 CPUs and 16 GB of memory. Each computation took about 20 hours. The solver used for the computation is MUMPS [62].

3.3.5 Results and discussions

The effect of the operating frequency on the cooling capacity and *COP* is now explored. The frequency range is 100 - 800 Hz. Steady-state is reached after four cycles of the diaphragm operation at a operating frequency of 100 Hz, as shown in Fig. 3.7.

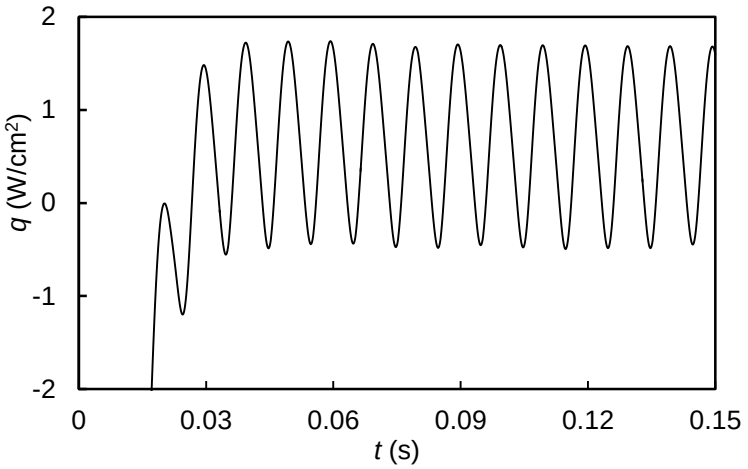

Figure 3.7 Space-averaged cooling capacity as a function of time at an operating frequency of 100 Hz when the porosity is 0.892. Steady state is achieved after four cycles.

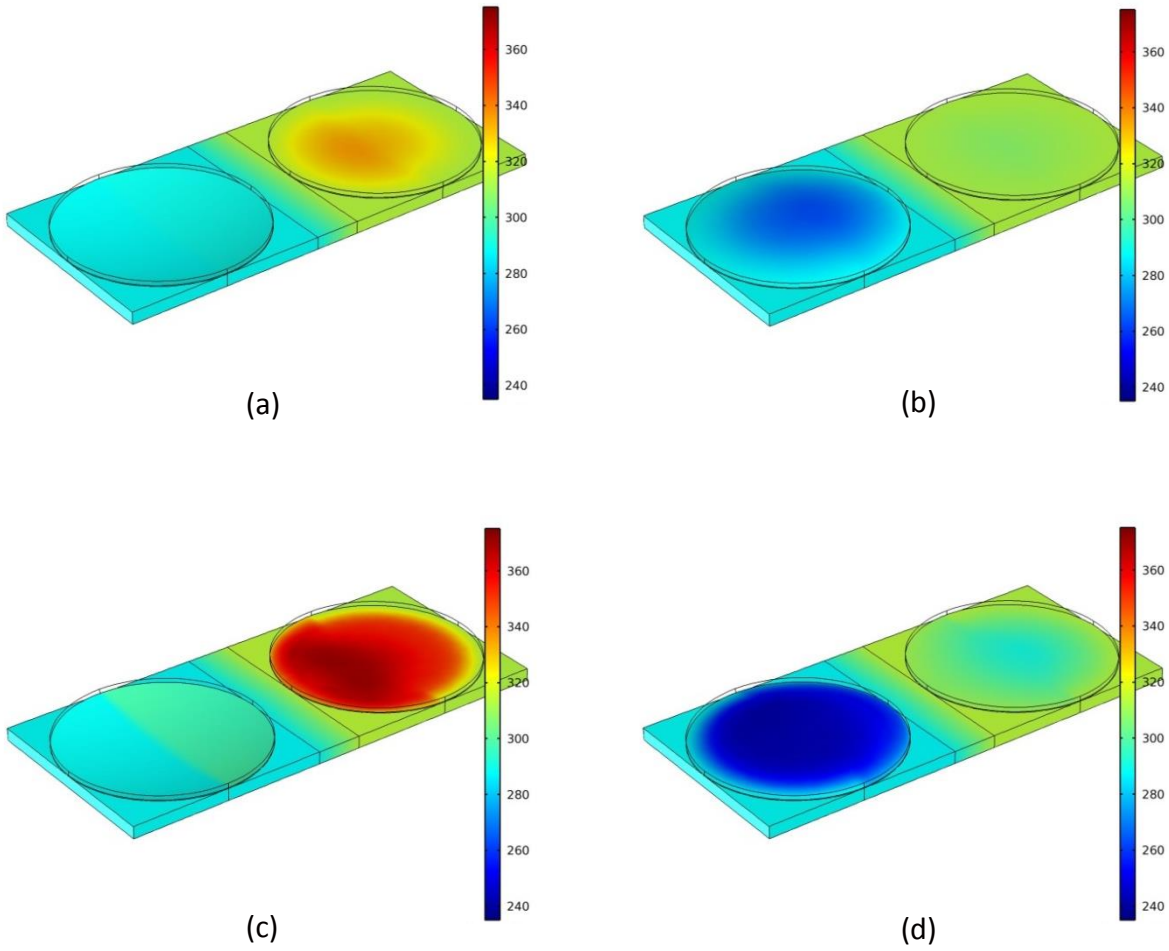

Figure 3.8 The temperature contours for the full Stirling cooler system simulation. (a) One quarter of the cycle at an operating frequency of 100 Hz. (b) Three quarters of the cycle at an operating frequency of 100 Hz. (c) One quarter of the cycle at an operating frequency of 800 Hz. (d) Three quarters of the cycle at an operating frequency of 800 Hz.

At steady-state, the temperature contours of the gas in the system and the silicon around the chamber at one quarter and three quarters of one cycle are shown in Figs. 3.8(a) and 3.8(b) when the frequency is 100 Hz. In Fig. 3.8(a), the cold diaphragm is completely compressed and the hot gas space has its highest temperature at this point in the cycle. During the compression process, the heat is released from the hot gas and transferred to the heat sink. In Fig. 3.8(b), the cold gas space is expanded. At this time, the cold gas space has its lowest temperature. This

process is an expansion in which the heat from the heat source is absorbed by the gas in the cold space. Through cyclings, the heat is transferred to the heat sink and absorbed from the heat source continually, as we require. The temperature contours at one quarter and three quarters of one cycle at a frequency of 800 Hz are shown in Figs. 3.8(c) and 3.8(d). The heat transfer process is similar compared to the results at 100 Hz. However, the maximum temperature in the hot gas space is much higher and the minimal temperature in the cold gas is much lower at 800 Hz.

The heat flux coming into the cold side from the end surface represents the cooling power density of the Stirling cooler. The time-dependent pressure and volume variations in the element are obtained from this simulation. The *PV* work can be therefore be calculated and the *COP* can be evaluated. The results of cooling power sensity is shown in Figs. 3.9(a). The analytical cooling power densities from Chapter 2 are also provided in Fig. 3.9(a). A good agreement between the analytical result and modeling result is observed. The cooling power density increases almost linearly from 0.7 to 5.1 W/cm^2 when the frequency increases from 100 Hz to 800 Hz. The *COP* with respect to the cooling capacity is plotted in Fig. 3.9(b). The *COP* decreases from 7.4 to 2.4 when the operating frequency and the cooling capacity increase. The reason is that even though the cooling power increases when the frequency increases, the thermodynamic work in the system increases more quickly, making the *COP* lower. An appropriate frequency should be considered according to the requirement of the real situation. When the operating frequency is 600 Hz, the *COP* is 2.93, which is about 25% of the Carnot *COP*, and the cooling capacity is 4.2 W/cm^2. In a standard design of a thermoelectric cooler (i.e., the material thickness is larger than 1 mm), the maximum cooling capacity is about 2 W/cm^2 and the best *COP* is 2.85 when the *ZT* of the material is 1 and the temperature difference is 15 K [5].

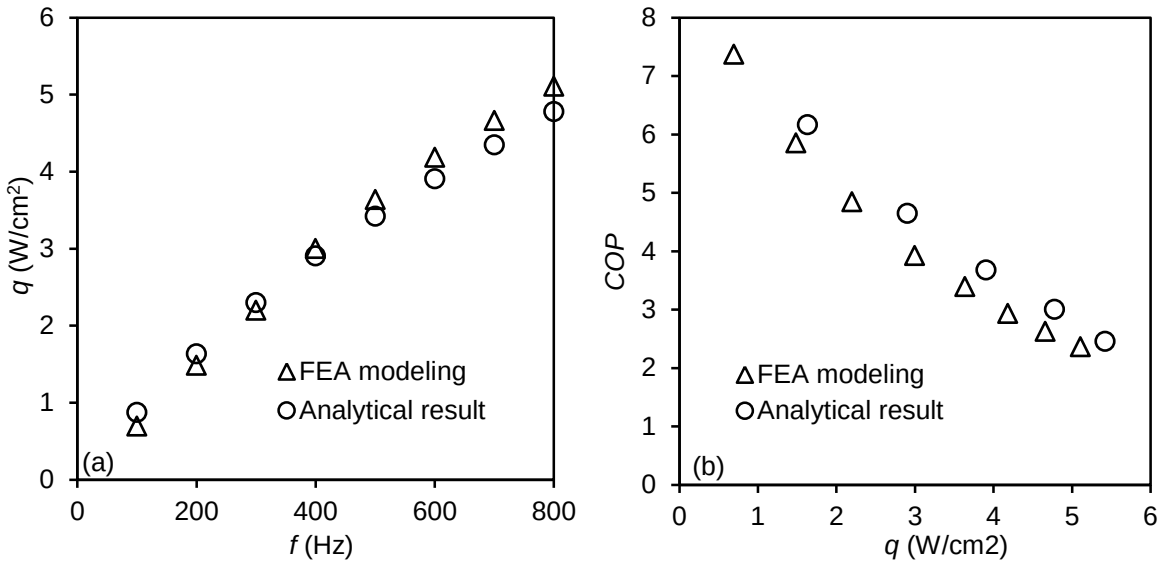

Figure 3.9 (a) System cooling power density as a function of the frequency from the multiphysics simulations and the analytical calculation from Chapter 2. With the increase of the operating frequency, the cooling capacity increases. (b) Multiphysics simulation prediction of the system *COP* and the analytical result as a function of the cooling power density. The theoretical *COP* is 11.5 With T_H = 313.15 K and T_C = 288.15 K.

3.4 Modeling of diaphragm actuation and thermal evaluation

In the previous sections, the thermal performance of the Stirling cooler was evaluated without considering the diaphragm actuation. In this section, the modeling of the diaphragm that is actuated electrostatically in each chamber will be discussed to identify the voltage requirement for the actuation. The chamber acting as the bottom electrodes is designed to be an axisymmetric spline cross-sectional shape. The electrodes gap between the diaphragm and chamber substrate near the anchored edge of the diaphragm is small, reducing the required pull-in voltage to initiate the actuation. With the applied voltage, the diaphragm moves down and contacts the substrate. The snap-in phenomenon occurs and moves towards the center. As the diaphragm pulls in, it follows the profile of the silicon chamber substrate. To acquire an accurate evaluation result, finite element analysis is performed to investigate the physics for large deformation of the diaphragm. This section is a joint work part with Jinsheng Gao.

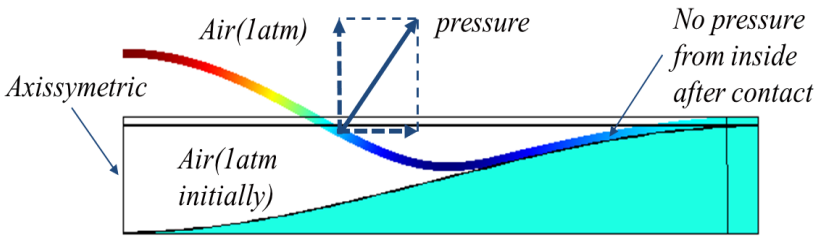

Figure 3.10 Computation domain and configuration for finite-element analysis.

The 2D axisymmetric model is shown in Fig. 3.10. The coupled multiphysics used in the modeling include the solid mechanics, electrostatic, and moving mesh technique. The gas pressure during the compression inside the chamber is estimated by adding the isothermal ideal gas. The contact force is calculated by adding a spring force on the diaphragm after contact. After contact, the distance of the gap becomes negative in the simulation, giving rise to a positive valued normal force acting on the diaphragm. The Hyperplastic Model (Mooney-Rivlin model) is used for simulating the deformation of the PDMS diaphragm. The detailed information about the contact model and Mooney-Rivlin model is shown in Section 5.4.

The simulation results for the pressure increase in the chamber as a function of applied voltage are shown in Fig. 3.11 (a) using the Mooney-Rivlin coefficients C_1 = 6 MPa, C_2 = 0.5 MPa for the diaphragm. From the figure, the differential pressure due to the compression at 100 V is only 340 Pa. At 200 V, the pressure increase is 1041 Pa. An optimization of diaphragm Young's modulus for realizing larger pressure difference is conducted, and the result at 200 V is shown in Fig 3.11 (b). A peak of pressure difference is observed, and the maximum value is 1620 Pa when the effective Young's modulus of the diaphragm is 280 MPa. The pressure difference obtained from the finite element analysis is much smaller than the required values (higher than 1 bar) from the thermodynamic analysis for maximizing the cooling performance.

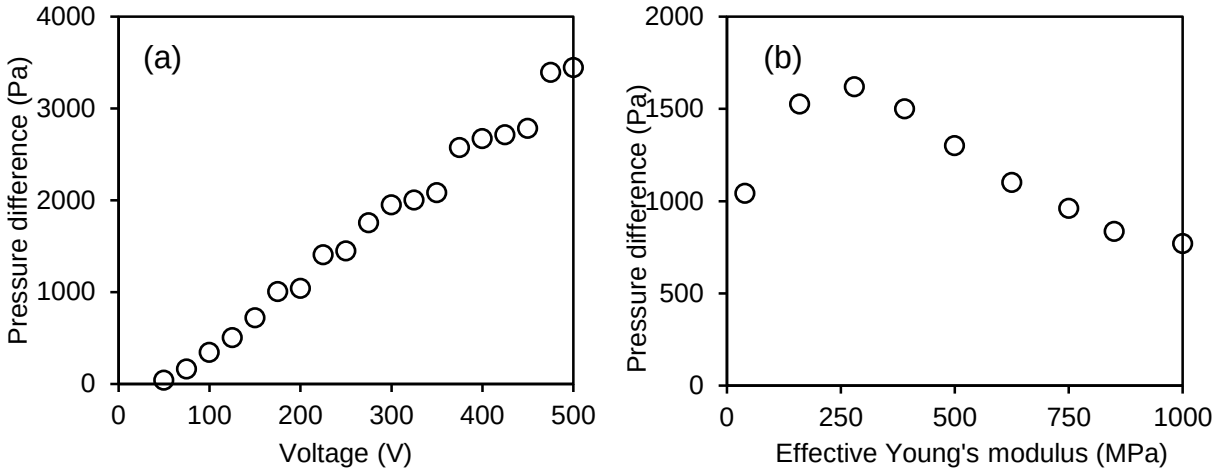

Figure 3.11 (a) Pressure increase in the chamber vs. the applied voltage on the diaphragm. (b) Pressure increase in the chamber vs. effective Young's Modulus of the diaphragm at 200V.

The thermodynamic performance of the Stirling cooler system is then evaluated based on the pressure difference calculated from the above diaphragm modeling result. Here it is assumed that no heat source is applied on the cold side, and only the heat conduction loss across the regenerator is included. The hot side temperature remains at room temperature, 293.15K, and the charge pressure is 1 bar. According to the thermal analysis in Chapter 2, the temperature drop in the cold side as a function of the maximum pressure difference in the system with different chamber volume (V_0 = 0.14 mm^3, $2V_0$, and $4V_0$) is obtained and shown in Fig. 3.12. In this analysis, the dead volume is equal to the chamber volume. The no-load heat transfer is less than 0.1W, and maximal temperature drop is less than 2 K employing the nominal chamber volume, V_0, at the pressure of 1600 Pa. The temperature drop has a large nonlinear dependence on the pressure differential. For example, if micro-actuation methods could achieve 5000 Pa differential pressure, then the temperature drop becomes 12 K in the no-load scenario with the nominal chamber volume.

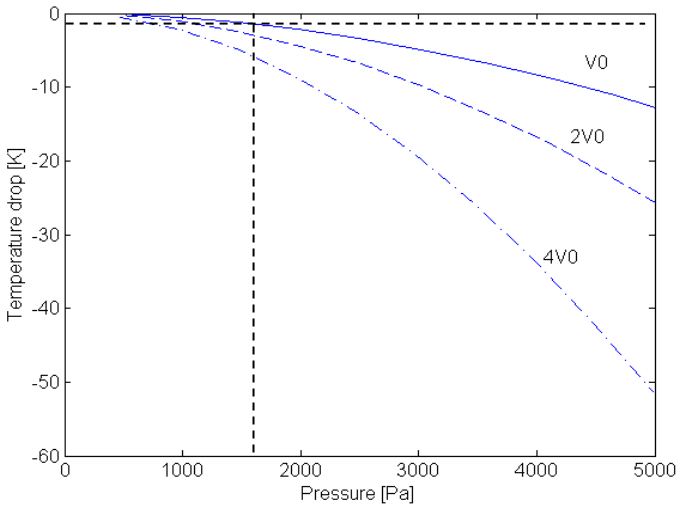

Figure 3.12 Temperature drop vs. pressure differential. The maximum pressure of 1600 Pa is indicated by vertical black dotted line.

3.5 Summary

In this chapter, the new Stirling micro-scale cooler has been modeled and simulated. The computations of multiphysics processes, incorporating compressible fluid flow, heat transfer, porous medium, solid mechanics, and moving mesh, have been successfully implemented.

The regenerator performance in the Stirling cooler was studied and the effects of pressure drop and heat transfer were analyzed. Optimizations indicated that the optimal porosity of the regenerator is near 0.9. The complete system modeling predicted the system-level thermal performance. Parametric studies of the design demonstrated the effect of the operating frequency on the cooling capacity and the *COP* of the system. When the system is operated at 600 Hz, the cooling capacity is 4.2 W/cm^2 and the system *COP* is 2.93 when the temperatures of the heat sink and heat source are 313.15 K and 288.15 K.

The diaphragm modeling results indicated that the electrostatic force is not large enough to compress the gas for achieving the desired cooler performance. Other actuation technologies may be onsidered for the further development of the micro Stirling refirgeration system.

Chapter 4 Experimental investigation of laminar flow across short micro pin fin arrays

4.1 Introduction

Recently the fluid flow across a bank of micro pillars has been demonstrated to be essential for many MEMS devices and systems, such as micro-scale heat exchangers, micro heat sinks, micro chemical reactors, micro bio-MEMS devices and also the micro regenerator in the refrigeration system [63-65]. Therefore the knowledge of the flow characteristic across a bank of micro pillars under various hydrodynamic conditions is critical for optimally designing these systems.

Over the last century, experimental estimations for the fluid flow across tube bundles at the conventional scale have been studied extensively in numerous literatures, and many correlations for predicting the friction factor have been established. Chilton and Generaux [66] summarized a general correlation to predict the friction factor when the air flows across long tube bundles in laminar and turbulent flow regions for both inline and staggered configurations. Based on the previous experimental data, Gaddis and Gnielski [67] suggested a new correlation for long tubes bundles considering the different configurations and various geometrical tube parameters. Intermediate size pin fins, which have a height-to-diameter (H/d) of 0.5 - 4, are commonly used for turbine blade internal cooling. Damerow [68] studied the turbulent flow for the short tubes ($2< H/d<4$), and found that the friction factor does not dependent on tube aspect ratio. The end wall effect is negligible in the turbulent flow regime. Morres and Joshi [69] measured the pressure drop of water across short staggered tubes ($0.5<H/d<1.1$) when the traverse pitch-to-diameter ratio (S_T/d) is 1.3-1.36. It is shown that the end wall effect is dominated at $100<Re<1000$, and the effect starts to diminish when Re exceeds 1000. Short et al.

[70] investigated the laminar flow across the circular staggered tubes bundles when the H/d is in a range of 1.88 - 7.25 and S_T/d is 2-6.4, and they indicated the end wall effect plays a critical role for the intermediate size tubes.

Recently experimental studies on the fluid flow in micro scale devices have attracted interest. Vanapalli et al. [71] experimentally examined the friction factors for gas flow across long pillar matrices (the aspect ratio is 10) with various shapes in the Reynolds number between 50 and 500, and no significant microfluidic effects were presented. Typically intermediate size pin fins ($0.5<H/d<4$) are employed in MEMS devices [72], and the Reynolds number in these devices can be smaller than 100, which is much lower than the Reynolds number range in the conventional scale. In such a low Reynolds number range, the end wall effect is expected to be more significant compared with the flow at a high Reynolds number due to the strong pillar-wall interaction. Thus the conventional friction factor correlation may not be able to predict the data in the micro-scale device accurately. Kosar [73] conducted the experiments for the pin fins with $1<H/d<2$, and proposed a correlation considering the end wall effect at $Re<100$. However, only 4 samples were tested in the paper to obtain their correlation, and the limited experimental database may affect the applicability of the correlation [74]. In addition, most of the studies focus on the flow in the dense pillar array. However, the sparse pillar array is frequently applied for the regenerator in the micro refrigeration system [1,34,35]. The pin fin spacing effect on the friction factor at the micro scale is to be determined.

Many researchers have performed a large number of modeling and experiments to quantify the roughness effect on the fluid flow in the micro-channel [75-79]. However, the roughness effect of micro pillar in the low Reynolds number flow is rarely found in the literature, especially for the large artificial roughness. Gao et al. [80] presented a fabrication process to

build micro pillar array for the regenerator in a Stirling micro-cooler. In their work, the ratio of the roughness amplitude to the pillar diameter is more than 0.1, due to the existence of the oxide mesh on top of the regenerator as shown in Fig. 4.1. It is unknown that how the large roughness affects the fluid flow and the regenerator performance. In some other applications, such as micro-reactors, the solid-fluid interface area is essential for the mixing and catalytic chemical reactions [64]. The existence of the artificial roughness may increase the interface area and enhance the thermal and mass transfer characteristics. Hence, there is a strong need to conduct experimental studies to establish the fundamental knowledge of the large artificial roughness effect of the pillar arrays in micro fluid systems.

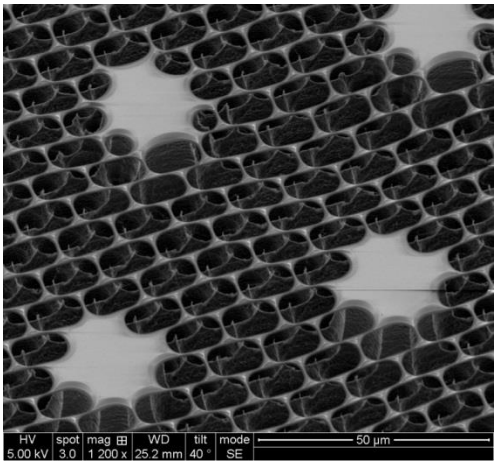

Figure 4.1 SEM of a fabricated regenerator with rough pillars [80]. The silicon oxide mesh layer is on the top.

In this chapter, a comprehensive experimental investigation on gas flow across circular pillar arrays with different pitch-to-diameter ratios and height-to-diameter aspect ratios for Re<100 were performed. Various artificial pillar roughness was created for the circular pillars and the frictional effect was investigated to compare with the results for circular pillar array. Unlike the scatted database of different experiments of various researchers at the conventional scale, large number of test devices were fabricated on the same silicon wafer and operated at the

same flow condition to conduct systematical measurements by taking advantage of the flexibility and low cost of micro-fabrication techniques.

The rest of the chapter is organized as follows. In Section 4.2, the preparation of devices and the experimental details are described. The geometric parameters and dimensionless variables are defined. In Section 4.3, the results are presented. The current data for circular pin fins are compared with the data of conventional flows, and the existing correlations of friction factor are compared. A new correlation, considering the coupled effects of the pin fin aspect ratio and pillar spacing, is proposed for predicting the friction factor. Finally, the comparison between the circular pillars and various pillars with artificial roughness is shown.

4.2 Experimental details

4.2.1 Device description

The top view of a sample device is shown schematically in Fig. 4.2 (a), and the fabricated contour is in 4.2 (b). A 2 mm wide channel containing a staggered micro-pillar array is fabricated on a 300 μm thick silicon wafer. Nitrogen gas is fed into the channel from the inlet and passes through the micro pin fin array. Two pressure ports are created at proper positions near the inlet and outlet of the pillar array. A 3 mm thick layer of polydimethylsiloxane (PDMS) is bonded with the silicon wafer device containing the channel after oxygen plasma treatments of both surfaces of the PDMS layer and the device. Holes in the PDMS layer are punched through by needles for tubing connection, and silicone rubber is used to seal between the tubing and the hole.

The geometric dimensions of the staggered pin fin array are shown in Fig. 4.2(c). The longitudinal spacing (S_L) is equal to the transverse spacing (S_T). The diameter of the circular silicon pillar is d, and the height of the pillar is H, which is not shown in the figure. Circular

micro silicon pin fin arrays with different diameters, transverse spacing, and heights are etched by the deep reactive ion etch (DRIE) process. Complex pillar structures with different artificial roughness are also fabricated on the same wafer by DRIE based on various mask designs. As shown in Fig. 4.2(d), two types of rough pillars (Type I: coarse roughness with 6 teeth and II: fine roughness with 8 teeth) are designed and manufactured in this study. Rough pillars with less than 6 teeth lead to rather irregular shape, and it appears not much different when artificial roughness has more than 8 teeth. The outer diameter of the rough pillar is d and the amplitude of the roughness is δ.

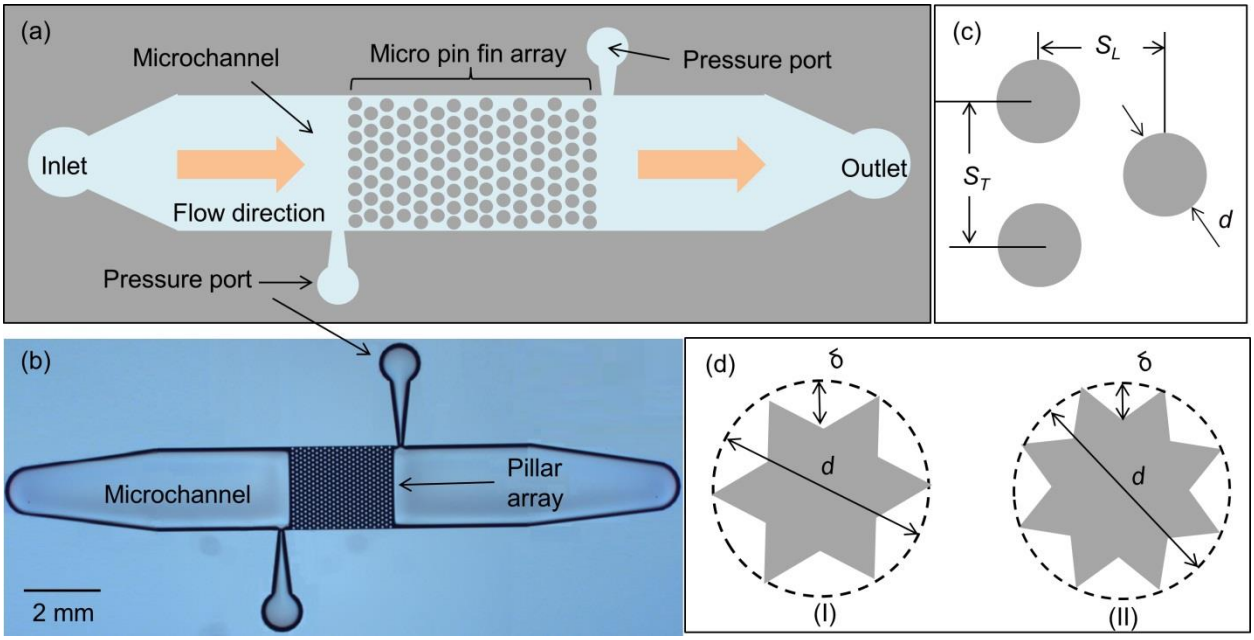

Figure 4.2 (a) Top view of a sample device including micro pin fin array, pressure ports, inlet and outlet. (b) View of one device under microscope. (c) Geometrical dimensions of the micro-pillar array. (d) Types of the rough pillar. Type I: coarse roughness with 6 teeth and II: fine roughness with 8 teeth.

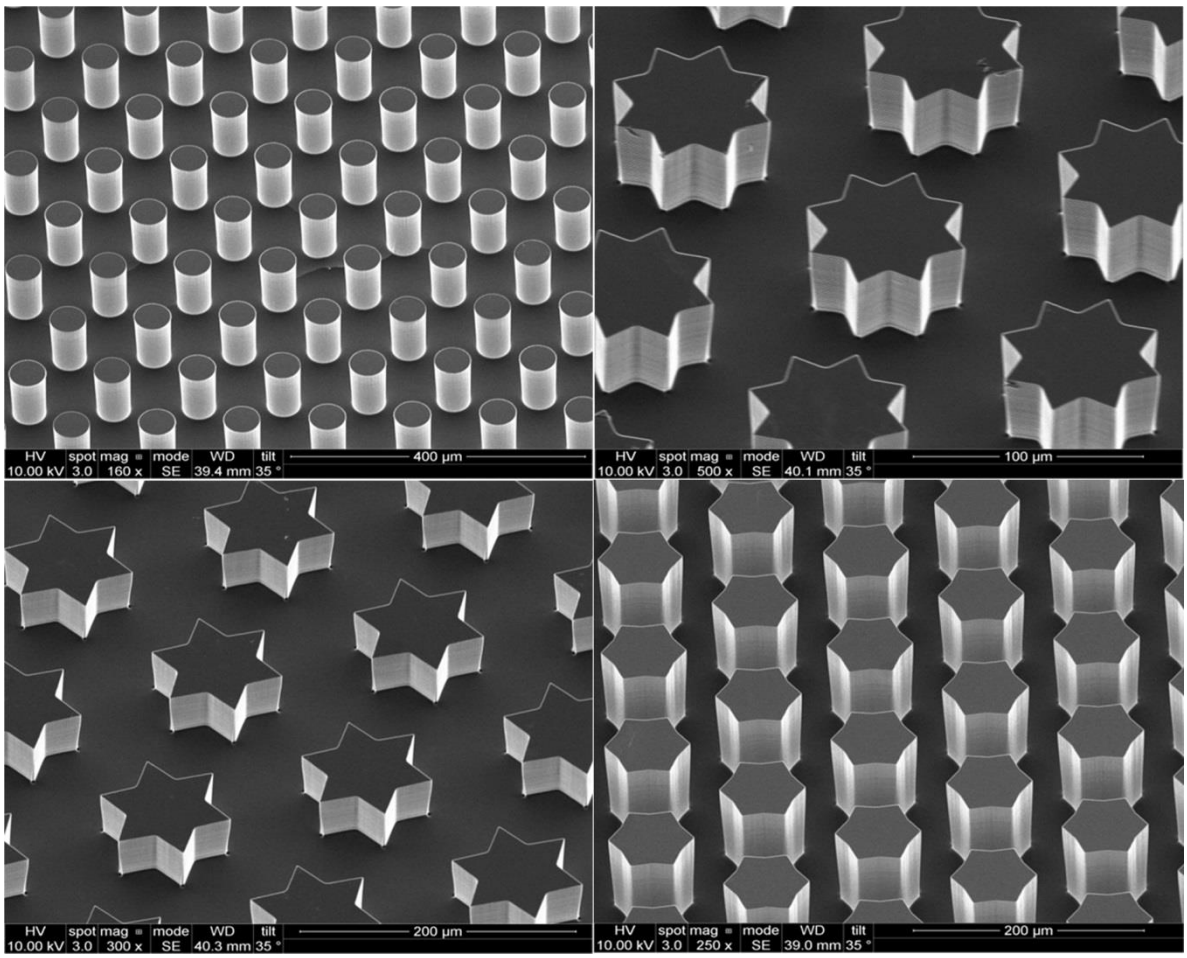

Figure 4.3 Typical SEM images of micro silicon pillar array with or without roughness.

The range of the diameters of the micro pillars are 50 µm, 75 µm and 100 µm, and the pitch-to-diameter ratios are 1.5 and 2.3. Total two wafers are fabricated, with different heights of 48 µm and 114 µm for each micro-channel. Typical SEM images of the micro pin fin array with or without artificial roughness are shown in Fig. 4.3 at various scales. The geometric parameters for all the test devices are summarized in Table 4.1. N is the number of the pillar rows along the stream, and δ / d is the roughness amplitude to diameter ratio. For the tests of small pitch-to-diameter ratio, S_T/d =1.5, the number of the pillar row is 25. For the large pitch-to-diameter ratio

of S_T/d =2.3, the pressure drop is smaller. To increase the pressure drop and reduce the data error at small Reynolds numbers, the number of the pillar rows is set to be 101. Totally, 22 devices were fabricated for the pressure drop measurements.

Table 4.1 A summary of the geometric parameters of test devices

Device	d (μm)	S_T / d	H / d	δ / d	N	Pillar Type
1	50	1.5	2.28	-	25	Circular
2	75	1.5	1.52	-	25	Circular
3	100	1.5	1.14	-	25	Circular
4	50	1.5	0.96	-	25	Circular
5	75	1.5	0.64	-	25	Circular
6	100	1.5	0.48	-	25	Circular
7	50	2.3	2.28	-	101	Circular
8	75	2.3	1.52	-	101	Circular
9	100	2.3	1.14	-	101	Circular
10	50	2.3	0.96	-	101	Circular
11	75	2.3	0.64	-	101	Circular
12	100	2.3	0.48	-	101	Circular
13	75	1.5	1.52	0.1	25	I: coarse roughness
14	75	1.5	1.52	0.15	25	I: coarse roughness
15	75	1.5	1.52	0.2	25	I: coarse roughness
16	75	1.5	1.52	0.1	25	II: fine roughness
17	75	1.5	1.52	0.15	25	II: fine roughness
18	75	1.5	1.52	0.2	25	II: fine roughness
19	100	1.5	0.48	0.2	25	I: coarse roughness
20	100	1.5	0.48	0.2	25	II: fine roughness
21	75	2.3	1.52	0.2	101	I: coarse roughness
22	75	2.3	1.52	0.2	101	II: fine roughness

All the in-plane geometric dimensions are determined using a calibrated optical microscope for accurate determinations of the Reynolds numbers and friction factors. The pillar diameter uncertainty is less than 2%. The pillar height is evaluated by a white light interferometer Wyko NT3300, as shown in Fig. 4.4, and the height variation for different pin fin structures is less than 5%. The gas supply is a nitrogen gas tank with a pressure regulator and the gas flow rate is controlled by a mass flow-meters and controller (FMA-A2403, Omega Engineering), which has a flow range of 0-100 cc/min and an accuracy of ±1%. A differential pressure transducer (MMDDU001V10K2A0T1A1CE, Omega Engineering), which has a maximum pressure response of 7000 Pa at 10 V with an accuracy of ±0.05%, is used to measure the pressure drop between the inlet and the outlet of the pressure ports on the device.

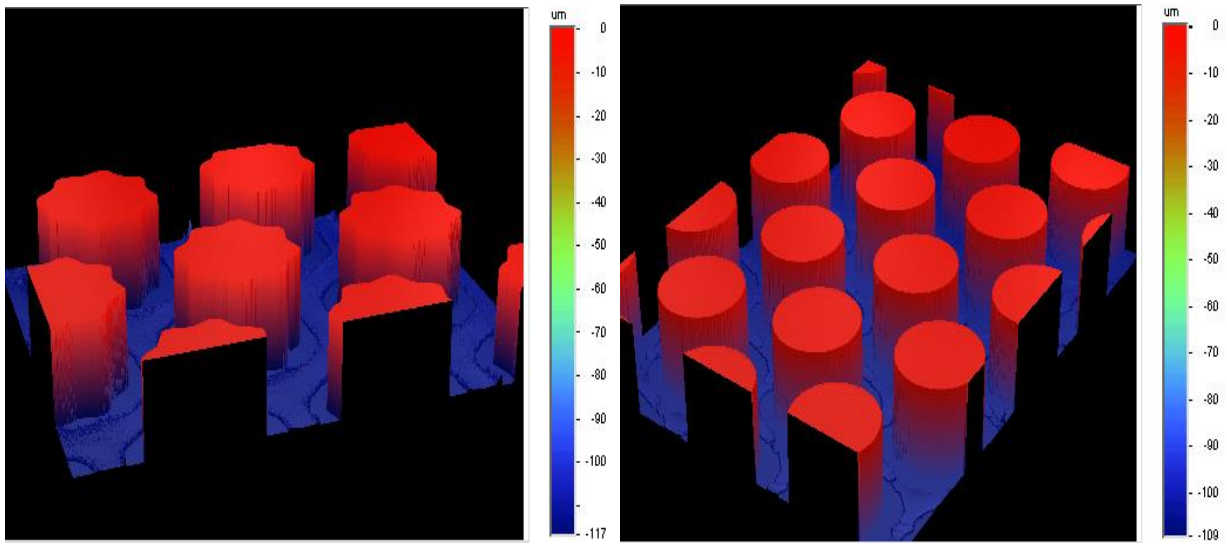

Figure 4.4 Wyko images for quantifying the height of micro silicon pillars.

4.2.2 Data reduction

There are several types of definitions of experimental correlation of pressure drop for the flow across tube bundle. The most commonly used friction factor is defined by Zukauskas and Ulinskas [81]

$$f = \Delta p/(\tfrac{1}{2} N \rho {u_{max}}^2) \,, \tag{4.1}$$

where N is the row number along the stream, and u_{max} is the maximum velocity in the pillar array, which is

$$u_{max} = Q/A_{min} \,. \tag{4.2}$$

Here Δp is the pressure drop across the pin fin array, ρ is the density of the gas, Q is the volume flow rate, A_{min} is the minimum cross-sectional area, and is expressed as

$$A_{min} = wH(S_T - d)/S_T \,, \tag{4.3}$$

where w is the total width of the flow channel.

The Reynolds number is defined as

$$Re = \rho u_{max} d_h/\mu \,, \tag{4.4}$$

where μ is the viscosity of the gas, and d_h is the hydraulic diameter of the fin, which is equal to the diameter for the circular pillars. The outer diameter of the pillar is used in Eq. (4.4) for the pillar with artificial roughness.

4.3 Results and discussions

As mentioned in Section 4.1, the friction factor across the pillar array is affected by the pillar aspect ratio and spacing significantly for short pin fins in the laminar flow region. The detailed test results for pin fin arrays with various types of artificial roughness are given at below.

4.3.1 Coupled effect of height-to-diameter ratio and pitch-to-diameter ratio

It has been reported that the height-to-diameter ratio of the short pin fin strongly affects the friction factor of the pillar array in the laminar flow region [73]. In this study, a detailed examination of this phenomenon is conducted and it is found that the effect of height-to-diameter ratio on the friction factor is different when the pin fin spacing varies. The friction factors at different height-to-diameter ratios are plotted in Fig. 4.5 when the *Re* is less than 100. The results of pitch-to-diameter ratio at 1.5 are in Fig. 4.5(a) and 2.3 in Fig. 4.5(b). The friction factor for the infinite long pin fin array is obtained from a 2D numerical modeling computation. Generally a larger friction factor is observed for a smaller *H/d* ratio. Compared to the friction factor for the infinite long pillar, the end wall effect diminishes when *H/d* is larger than 0.64 at S_T/d = 1.5. However, at S_T/d = 2.3, the end wall effect is still not negligible even at *H/d*=2.28. When *H/d* is varied from 0.48 to 2.28, the friction factor difference is about 5 times at S_T/d = 2.3. In a sparse pillar array (S_T/d = 2.3), the pressure drop contribution due to the hydraulic boundary layer effect induced by end walls is larger than that in a dense pin fin array (S_T/d = 1.5). Thus, the *H/d* effect is more significant at sparse pillar array (S_T/d = 2.3) than that at a dense array (S_T/d = 1.5).

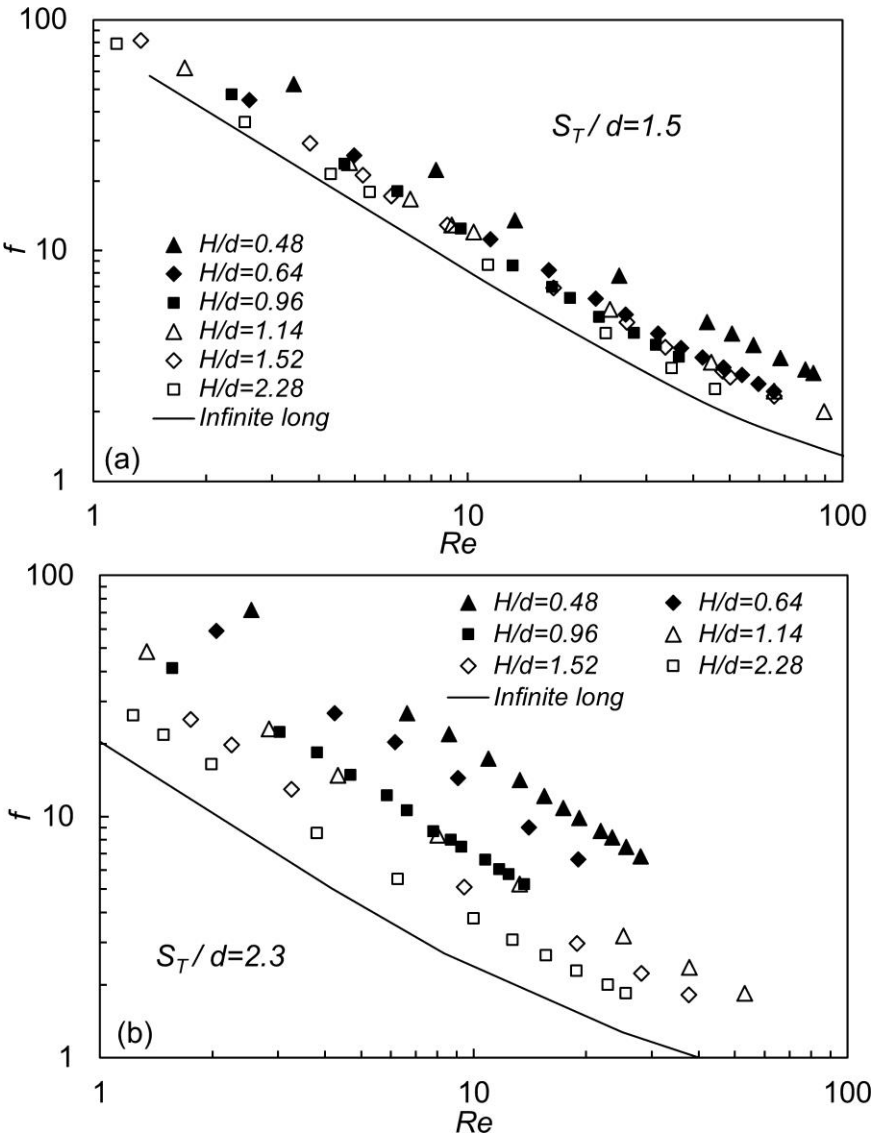

Figure 4.5 Friction factors as a function of *Re* for the circular staggered pillar array with different height-to-diameter ratios (a) S_T/d=1.5 (b) S_T/d=2.3. The result for infinite long pillar is from numerical simulation.

Conversely, the pin fin spacing effect on the friction factor also depends on *H/d*. As shown in Fig. 4.6, dense pillar arrangement results in higher friction factor when *H/d* is 0.96 and 2.28. However, at *H/d*=0.48, the end wall effect is so strong that there is almost no difference for the friction factor even though the pitch-to-diameter ratio changes from 1.5 to 2.3.

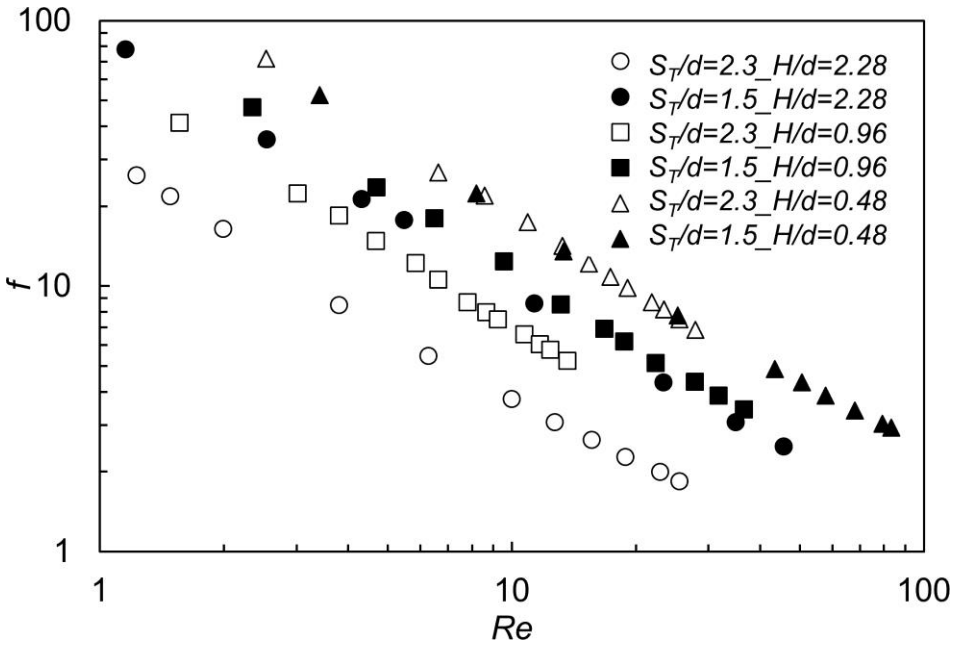

Figure 4.6 Friction factors for the circular staggered pillar array with different pitch-to-diameter ratios (S_T/d=1.5 and 2.3) when H/d is 0.48, 0.96, and 2.28.

Several correlations for friction factors have been developed from the experimental data for the flow across staggered circular pin fin array. The correlations of Chilton & Generaux [66], Gaddis & Gnielski [67], and Sparrow & Grannis [82] are well known and are used to predict the friction factor for long tubes at the conventional scale. The correlation from Short et al. [70] and Moores & Joshi [69] address the end wall effect. The mean absolute error (MAE) of the friction factor between the current experimental data and the predictions from a correlation is defined as

$$MAE = \frac{1}{n}\sum_{i=1}^{n}\frac{|f_{exp}-f_{correlation}|}{f_{exp}} \times 100\%. \quad (4.5)$$

where n is the number of data points. The results of MAE of present data and those established correlations are presented in Table 4.2.

Table 4.2 Mean absolute error of friction factors between the present experimental data and values calculated from available correlations for circular pillar array

Devices	S_T/d	H/d	MAE (%)				
			Chilton & Generaux	Gaddis & Gnielski	Sparrow & Grannis	Short et al.	Moores & Joshi
1	1.5	2.28	9.85	8.11	3.08	33.4	63.4
2	1.5	1.52	12.9	15.4	15.1	36.6	52.2
3	1.5	1.14	20.9	23.2	18.5	47.8	40.3
4	1.5	0.96	9.77	12.4	14.2	109	25.7
5	1.5	0.64	24.0	26.2	21.4	108	25.5
6	1.5	0.48	49.2	50.7	44.4	76.0	15.2
7	2.3	2.28	188	42.2	155	20.9	26.2
8	2.3	1.52	113	56.7	92.0	24.4	34.9
9	2.3	1.14	43.4	70.9	35.5	21.2	32.2
10	2.3	0.96	52.4	69.1	34.2	16.3	27.4
11	2.3	0.64	14.4	82.6	23.8	38.0	41.6
12	2.3	0.48	43.6	88.6	47.3	40.7	35.2

The current experimental data agrees well with conventional correlations of Chilton & Generaux, Gaddis & Gnielski, and Sparrow & Grannis, for the dense pillar array (S_T / d = 1.5) when H/d is 2.28 (the maximum MAE of these three correlations is less than 10%). At S_T/d = 1.5, with the decrease of H/d, MAE becomes larger as these correlations do not consider the effect of

end walls. Generally, MAE is less than 25% when *H/d* exceeds 0.64 by using these correlations to predict the friction factor. However, the MAEs of these correlations are 49.2%, 50.7% and 44.4% at *H/d*=0.48, respectively. For the sparse pillar array (S_T/d = 2.3), the existing correlations poorly predict the friction factor. As mentioned above, the correlations from Short et al. and Moores & Joshi include the end wall effect of pillar array. However, the overall MAE between the present data and their correlations for all the devices exceeds 30% and a large deviation of these correlations is also reported by other researchers [73,74]. In general, these existing correlations are applicable for long tubes and the dense pin fin array. However, a new correlation which considers the end wall and pillar spacing effects is necessary to be proposed for the evaluation of laminar flow across short pin fin array.

From the experimental data shown in Fig. 4.5, the effects of the end wall and the pillar spacing are coupled. Thus a term which includes this coupled effect should be included in the new correlation for a reasonable prediction. The correlation proposed in this paper has a form as follows,

$$f = C_1 Re^{C_2} \left(\frac{S_T}{d} - 1\right)^{C_3} \left[\frac{(H/d)}{(H/d)+1}\right]^{C_4\left(\frac{S_T}{d}-1\right)}, \tag{4.6}$$

where C_1, C_2, C_3, C_4 are constants, and determined by the least square fit method. Their values are found to be C_1=24.1, C_2= -0.906, C_3= -1.40, C_4= -1.50. Then the final correlation is

$$f = 24.1 Re^{-0.906} \left(\frac{S_T}{d} - 1\right)^{-1.40} \left[\frac{(H/d)}{(H/d)+1}\right]^{-1.50\left(\frac{S_T}{d}-1\right)}, \ (1 < Re < 100). \tag{4.7}$$

In the correlation, the term $\left(\frac{H/d}{H/d+1}\right)^{C_4\left(\frac{S_T}{d}-1\right)}$ describes the coupled effect of pillar spacing and end walls. For a very long pillar, the effect of this term diminishes, and the results converge to the

conventional long tube correlations at Re < 100. This is an empirical correlation obtained from experimental data and other kinds of forms of correlations may also exist. Table 4.3 lists the MAE of the new correlation of this paper. The maximum MAE is 17% and the average MAE for all the devices is 7.80%. The comparison between the present experimental data and the friction factor predicted by the new correlation is displayed in Fig. 4.7, and 97% of the data fall within ±20% of the new correlation as shown.

Table 4.3 Mean absolute error of the new correlation (Eq. (4.7)) for circular pillar array

Device	1	2	3	4	5	6	7	8	9	10	11	12	Overall
MAE (%)	8.09	5.24	6.27	9.91	5.42	7.24	3.55	7.69	5.03	17.0	10.9	7.24	7.80

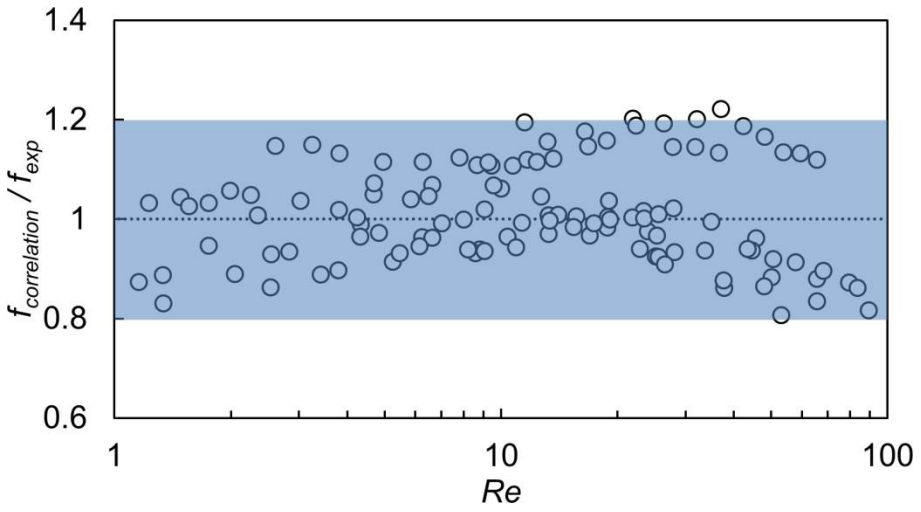

Figure 4.7 Friction factor comparison between experimental data and values calculated from the new correlation.

4.3.2 Effect of artificial roughness

In this section, the various artificial roughness of the pin fin, as shown in Fig. 4.2 and Table 4.1, is considered to explore their effects on friction factors. The friction factor as a function of Reynolds number for Devices 13-18 with different roughness amplitudes (δ/d) are

plotted in Fig. 4.8, where the pitch-diameter-ratio is 1.5 and the height-diameter-ratio is 1.52. The results for pillars with coarse roughness (6 teeth) are in Fig. 4.8(a) and the fine roughness (8 teeth) results are shown in Fig. 4.8(b).

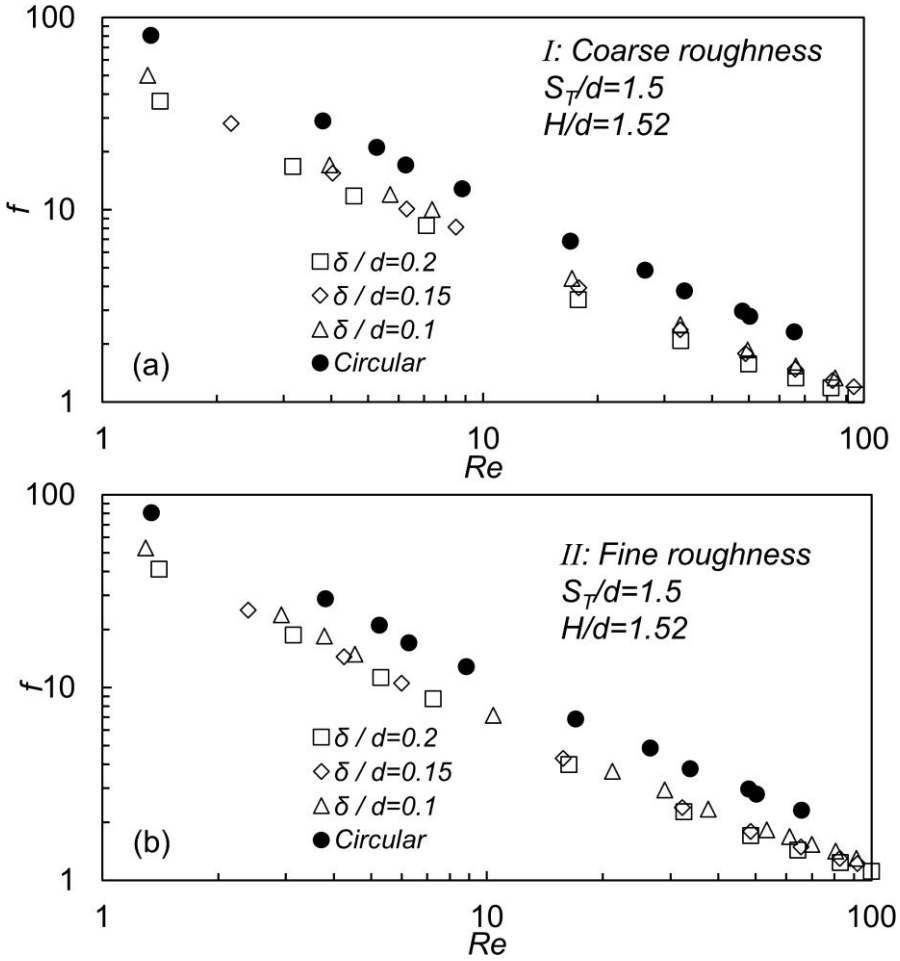

Figure 4.8 Friction factors for circular pin fins and rough pillars with different roughness amplitudes. (a) Type I: coarse roughness (b) Type II: fine roughness. The pitch-to-diameter ratio is 1.5 and the height-to-diameter ratio is 1.52.

For both types of roughness, the friction factor demonstrates a same trend of decreasing from the circular pillar array in a Reynolds number range of 1-100. With the increase of the roughness amplitude, the reduction of the friction factor is growing. For example, when the Reynolds number is 1.35, the friction factors of circular pillar, coarse roughness pillar with δ / d

= 0.1, 0.2, and fine roughness pillar with δ / d = 0.1, 0.2 are 80.8, 50.2, 39.1, and 51.3, 41.2 respectively. More than 50% reduction of the friction factor is observed for the rough pillar at δ / d = 0.2. At higher Reynolds numbers, such as at *Re* = 66, friction factors of circular pillar, coarse roughness pillar with δ / d = 0.2, and fine roughness pillar with δ / d = 0.2 are 2.30, 1.34 and 1.41 respectively. About 40% of the friction factor decrease is presented.

In Fig. 4.9, the effect of the height-to-diameter ratio is demonstrated for different types of roughness at δ / d = 0.2. Due to the strong wall-pillar interaction at a low aspect ratio, the roughness effect tends to diminish as the end wall effect becomes dominate. In addition, comparing the friction factors between the coarse roughness and fine roughness, the friction factor of coarse roughness shows more reduction; however, it is only about 10% lower than that of fine roughness.

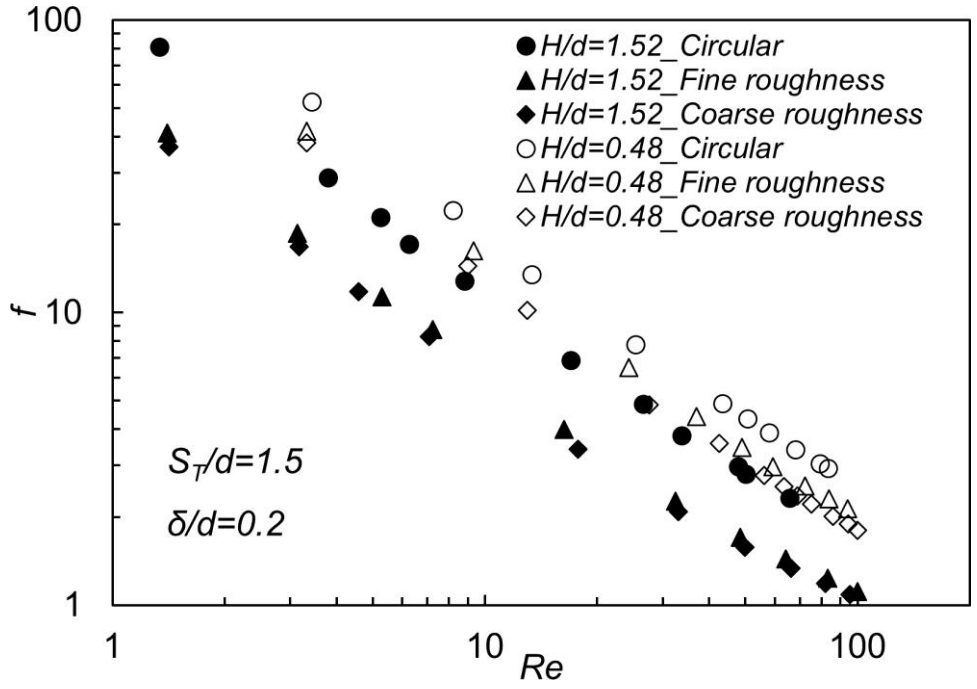

Figure 4.9 Friction factor of rough pillars for different roughness types (coarse roughness and fine roughness). The pitch-to-diameter ratio is 1.5 and the roughness amplitude ratio is 0.2.

The roughness effect with different pitch-to-diameter ratios is also investigated and the results are plotted in Fig. 4.10. For example, at S_T / d = 2.3, friction factor is f = 25.3 at Re = 1.75 for circular pillar, and f = 19.8 at Re = 1.81 for coarse roughness pillar with δ / d = 0.2. The friction factor difference between the circular pillar and coarse roughness pillar is only about 20%, which is much less than the difference for the dense pillar array (S_T / d = 1.5) as shown in Fig. 4.10. Thus, the roughness effect is much less important for the sparse pillar array (S_T / d = 2.3) compared with the effect on the dense pillar array (S_T / d = 1.5).

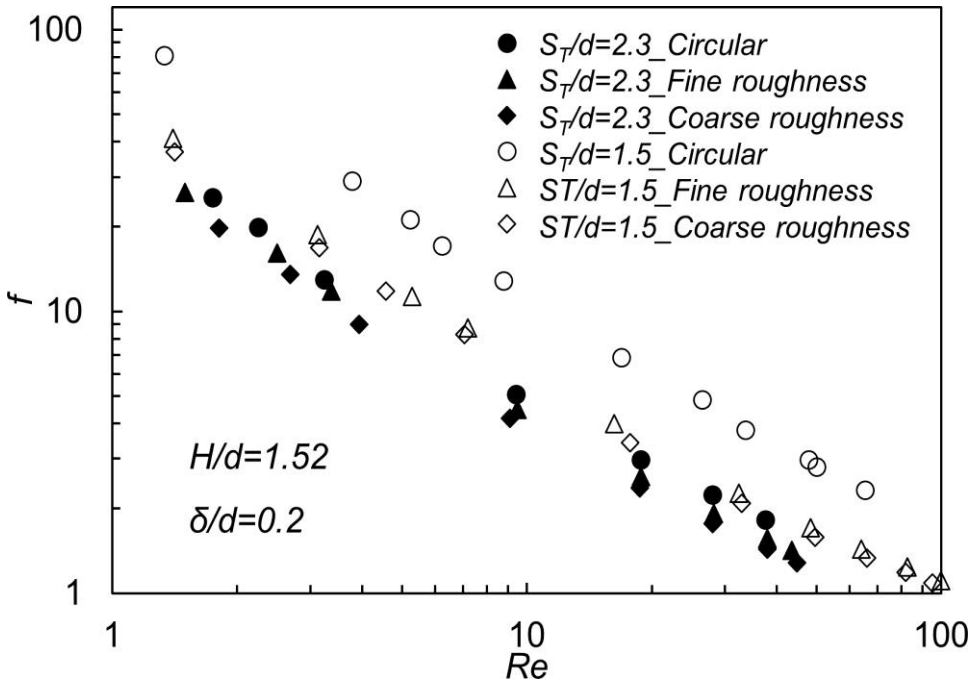

Figure 4.10 Friction factor comparisons of circular and rough pillar arrays with different pitch-to-diameter ratios (1.5 and 2.3). The height-to-diameter ratio is 1.52 and the roughness amplitude ratio is 0.2.

From the above discussions, when a large artificial roughness is created while maintaining the outer diameter same as the circular pillar diameter, the maximum fluid velocity across rough pillars becomes smaller as the effective minimum cross section area increases. Thus the pressure drop and the friction factor will reduce compared to the flow across circular pillars.

This effect is relatively stronger when the pillar spacing is smaller as shown in Fig. 4.10. Therefore, the existence of the pillar roughness can reduce the pressure drop of the pin fin array significantly. This could be an effective method, which is easily realized by the mask design in lithography process, to improve the efficiency of the micro regenerators, micro reactors or other related applications.

4.4 Summary

In this chapter, experimental investigations of the friction factors for gas flow across staggered circular and rough pin fin arrays have been performed in the range of Reynolds number between 1 and 100. Friction factor comparisons between the present experimental data and values from existing correlations were performed. A new correlation, Eq. (4.7), was proposed to predict the friction factor for the circular pin fin array, including the coupled effect of height-to-diameter ratio ($0.48 < H / d < 2.28$) and pitch-to-diameter ratio ($1.5 < S_T / d < 2.3$). The main conclusions are summarized as follows:

The existing conventional correlations predict the friction factor of dense ($S_T / d = 1.5$) and relatively long ($H / d = 2.24$) pin fin arrays well in the laminar flow region. However, for the sparse and short pin fin array, large deviations between the experimental data and correlation values are observed. The application of those existing correlations in many micro-scale devices needs special caution.

The pin fin spacing and pillar aspect ratio have a significant effect on the friction factor, and their effects are coupled. The pillar aspect ratio effect is more essential for a sparse pillar array.

The new correlation, considering the coupled pin fin spacing and pillar aspect ratio, for

the circular pillar array predicts the friction factor more accurately, and the average MAE of the correlation is 7.80%.

The rough pillar array leads to smaller friction factors than a corresponding circular pillar array, and larger artificial roughness amplitude results in smaller friction factors. The reduction of the friction factor could exceed 50% compared with the circular pillar array when the artificial roughness amplitude to the pillar diameter ratio is 0.2, which demonstrates the potential of this structure in the application of micro-regenerators, micro-reactors or other related MEMS devices for improving the efficiency.

The difference between the coarse and fine roughness is negligible and the roughness effect is more pronounced for the dense pillar array.

Chapter 5 Design and modeling of a fluid-based electrocaloric refrigeration system

5.1 Introduction

Stirling cooler is operated based on a thermodynamic cycle. In recent years, some other new cooling technologies that take advantage of magnetocaloric [83] and electrocaloric (EC) [31-33] effects also have attracted interest. The electrocaloric (EC) effect is a phenomenon in which reversible temperature and entropy changes appear in certain materials under the application and removal of an electric field. Applying the electric field orients the dipoles and reduces the entropy associated with the polarization. This process happens so fast (on the order of milliseconds [27]) that it can be considered to be adiabatic. The temperature of the material therefore increases, as required by the entropy decrease. Reversely, removing the electric field disorders the dipoles, increases the entropy, and cools the material. The main advantage of EC cooling over magnetocaloric cooling (which operates on an analogous principle) is that the high electric field required for the process is much easier and less expensive to generate than the high magnetic field required for magnetocaloric cooling [26].

EC effect was first reported by Kobeco and Kurtschatov in 1930 [28], potential applications have been limited by the relatively low entropy and temperature changes for most ferroelectric materials [the highest value reported before 2006 was 2.6 K at an electric field of 3 V/μm and a temperature of 434 K for bulk $Pb_{0.99}Nb_{0.02}(Zr_{0.75}Sn_{0.20}Ti_{0.05})_{0.98}O_3$ [84]]. Recently, materials with a large EC effect have been discovered [29,30], suggesting practical applications in cooling devices. Some EC materials and their performances are listed in Table 5.1. Among these materials, a P(VDF-TrFE-CFE) terpolymer, poly(vinylidene fluoride-trifluoroethylene-

chlorofluoroethylene), demonstrates an adiabatic temperature change of 15.7 K under an electric field of 150 V/μm over temperatures between 270 K and 320 K [85].

Table 5.1 Summary of EC materials and their performances

Year	Material	Reference temperature (˚C)	Electric field (V/μm)	ΔT (K)	$\Delta T / \Delta E$ [(K· μm)/V]
1963[86]	Rochelle Salt	22.2	0.14	0.0036	0.0257
1977[87]	$SrTiO_3$	269	0.542	1	1.85
1981[84]	$Pb_{0.99}Nb_{0.02}(Zr_{0.75}$-$Sn_{0.20}Ti_{0.05})O_3$	161	3	2.6	0.867
2006[29]	$PbZr_{0.95}Ti_{0.05}O_3$	226	48	12	0.25
2010[88]	P(VDF-TrFE)	80	209	12	0.0574
2011[85]	P(VDF-TrFE-CFE)	30	150	15.7	0.105

In this chapter, a refrigeration system based on the EC effect of the P(VDF-TrFE-CFE) terpolymer is designed that uses a dielectric fluid to transfer the heat between the EC material and the heat sink/source, as shown in Fig. 5.1. In the design, each cooling element includes two diaphragm actuators fabricated on a silicon wafer. A set of five terpolymer layers are placed between the two diaphragm chambers. Each element is designed such that the fluid flow direction is within the plane of the wafer.

The remainder of this chapter is organized as follows. In Section 5.2, the design concept of the fluid-based EC micro-scale cooler is presented. In Section 5.3, finite element modeling is used to evaluate the full system thermal performance with an assumption of a sinusoidal diaphragm motion. The design philosophy is discussed in detail. In Section 5.4, multiphysics simulations of the system coupled thermal modeling and modeling of the diaphragm driven by electrostatics are performed and the results are compared with that in Section 5.3.

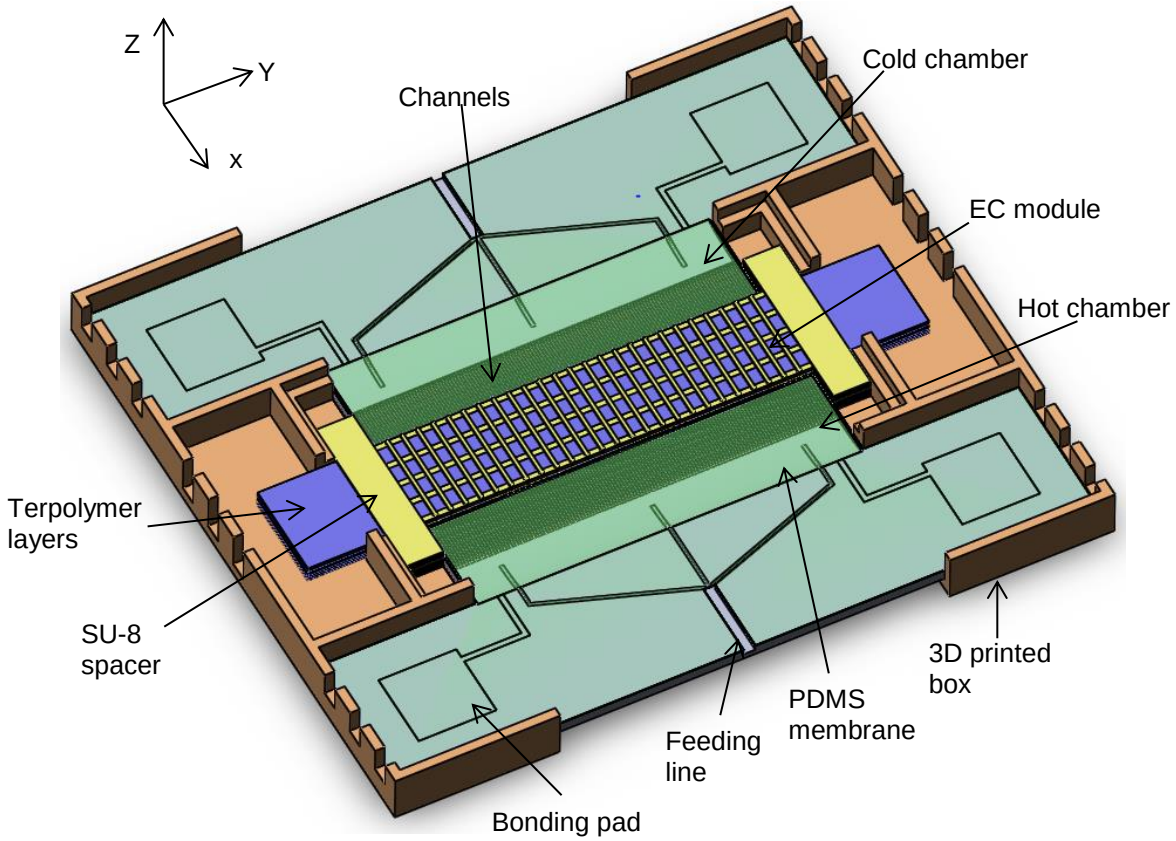

Figure 5.1 Solid-model view of the EC cooler element. The two diaphragm actuators are driven electro-statically. The EC module, which includes multiple terpolymer layers, is located between two diaphragm actuators. The fluid flow is within the plane of the wafer (Courtesy of Andrew Slippey).

5.2 Design concept

5.2.1 Overall design

The cooling element is includes two chambers made of cavities and diaphragms that are fabricated on a silicon wafer, as shown in Fig. 5.1. Several terpolymer layers (20 μm thickness for the middle layers and 10 μm thickness for the top and bottom layers) are located between the two chambers. The diaphragms have a diameter of 2 mm, are made of a polydimethylsiloxane (PDMS) layer embedded with electrodes, and are driven electro-statically. Spacers made of SU-8 photodefinable epoxy (MicroChem Corp., 2000 series) are placed between the terpolymer layers

to form channels for the fluid flow. The working fluid is HT-70, which is a heat transfer liquid and an electrical insulator. It does not chemically react with the PDMS or the terpolymer.

As illustrated schematically in Fig. 5.2, the EC-based thermodynamic refrigeration process in our cooler design includes four steps: A. Heat absorption: the fluid absorbs heat from the cold side (heat source); B. Polarization: the hot diaphragm moves up and the cold diaphragm moves down, the EC material is heated by applying the electric field and the fluid absorbs the heat from the EC material as it flows from the cold side to the hot side; C. Heat rejection: the heat carried by the fluid is rejected to the hot side (heat sink) while the electric field is on; D. Depolarization: the cold diaphragm moves up and the hot diaphragm moves down, then the fluid moves from the hot side to the cold side and releases heat to the EC material when the electric field is turned off. Through periodic cycling, heat is extracted from the cold fluid chamber and released to the hot chamber, and the fluid reaches its lowest temperature in the cold side.

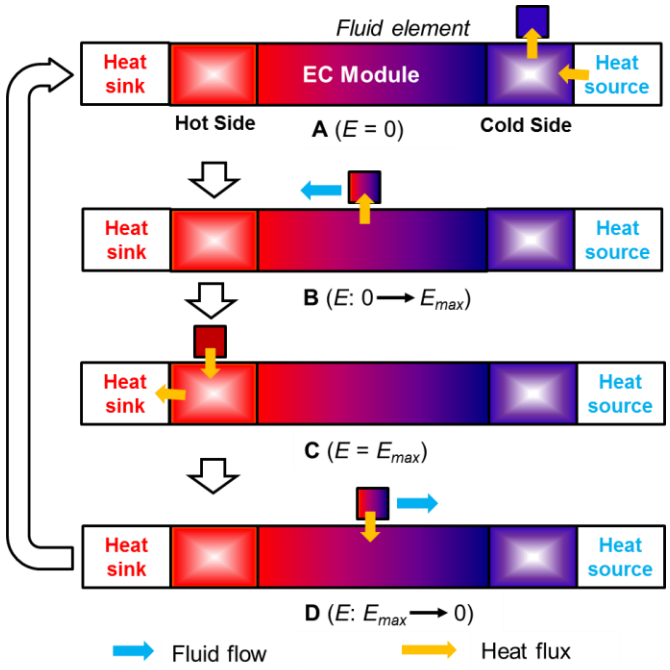

Figure 5.2 The thermodynamic refrigeration cycle of a fluid element based on the EC effect. The process includes four steps: (A) heat absorption, (B) polarization, (C) heat rejection, and (D) depolarization.

5.2.2 Hot and cold chambers

The in-plane design offers efficient thermal isolation by enabling the EC module between the two diaphragm actuators. The diaphragms are actuated electro-statically in the hot and cold chambers to drive the working fluid, which transfers heat between the two chambers. In this design, the bulk silicon substrate on which the device is grown is etched with "zipping" shaped chambers under the diaphragms. The silicon enables efficient heat transfer between the fluid and the heat source/sink to improve the performance of the cooling element. The "zipping" shaped substrate reduces the pull-in voltage required to actuate the diaphragms. Fins are built at the outlet of the chambers to guide the fluid and improve the heat transfer between the fluid and heat sink/source, as shown in Fig. 5.1.

5.2.3 Working fluid and thermal penetration

The relevant properties of the working fluid HT-70 are provided in Table 5.2.

Table 5.2 Properties of HT-70 and P(VDF-TrFE-CFE) terpolymer

Material	ρ (kg/m^3)	μ (Pa·s)	k (W/(m·K))	c (J/(kg·K))
HT-70 [89]	1680	8.4×10^{-4}	0.065	970
P(VDF-TrFE-CFE) terpolymer [90]	1800	-	0.2	1500

The height of the channels between the EC polymer layers and the space between the fins at the outlet of the chambers are determined according to the thermal penetration depth, which is defined by Eq. (2.1). For HT-70, the thermal penetration depth at a temperature of 298 K is 25 μm at an operating frequency of 20 Hz, which is near the maximum practical operating frequency of the device. The channel height and fin space are therefore chosen to be 50 μm for the design. The properties of the terpolymer are also listed in Table 5.2. The maximum thickness

of the terpolymer layer is 20 μm, which is smaller than its thermal penetration depth of 34 μm at an operating frequency of 20 Hz and a temperature of 298 K.

5.3 Thermal evaluation of the system

5.3.1 Governing equations

The fluid flow is incompressible and described by the Navier-Stokes equations. The energy equation within the EC material is

$$\rho c \frac{\partial T}{\partial t} = k\nabla^2 T - \dot{Q}, \tag{5.1}$$

where T is the temperature and t is time. $\dot{Q}$ is the heat source term due to the EC effect of the material, which is described by

$$\dot{Q} = \rho T (\frac{\partial S}{\partial E})_T \frac{\partial E}{\partial t}, \tag{5.2}$$

where S is the entropy and E is the applied electric field [91]. The relationship between the entropy change and the electric field is obtained from experimental data [85]. For the P(VDF-TrFE-CFE) terpolymer, the entropy in Eq. (5.2) can be modeled as

$$S = C_1 E^2 + C_2 E, \tag{5.3}$$

where C_1 = - 2.71×10^{-15} J•m^2/(kg•K•V^2) and C_2 = - 6.85×10^{-8} J•m/(kg•K•V). While the relationship between entropy and electric field is generally temperature-dependent, the EC effect of this terpolymer does not demonstrate a large deviation when the temperature changes from 270 K to 320 K [85]. Therefore, the entropy change is assumed to be temperature independent for simplicity within this temperature range. We note that the reported dielectric loss of the terpolymer is small and is ignored in the modeling. At 150 V/μm, the input electric energy

density calculated from the electric displacement - electric field hysteresis loop is 3 J/cm^3 [92], which is less than 7% of the material cooling energy density (43.2 J/cm^3).

5.3.2 Computational setup

The computational region is shown in Fig. 5.3. By taking advantage of symmetry, only a single slice of the device is modeled. The temperature at the hot end of the element is constant and is T_H = 300.15 K. The cold end also has a constant temperature. The remaining surfaces are thermally insulated. The initial temperature for the whole system is a linear profile in the *x*-direction (see Fig. 5.3). The no-slip condition is applied to the solid-liquid interfaces. As the diaphragms are driven electro-statically, their actual motions are complicated and are discussed in Section 5.4. In this section, to simplify the model and the analysis, a sinusoidal motion with a 180° phase lag is applied for the cold and hot diaphragms. The displacement of the cold diaphragm is $z(x, y, t) = Z_{max}(x, y)\sin(2\pi f t)$. The hot diaphragm and the cold diaphragm oscillate 180˚ out of phase but with the same amplitude. Here, $Z_{max}(x, y)$ is the amplitude of the diaphragm vibration. The substrtate shape is a cubic curve, and the maximum height is 150 μm. So, $Z_{max}(x, y)$ represents the height between the diaphragm and the substrate at different positions. The hot and cold diaphragms prescribe the moving boundaries of the fluid flow. The arbitrary Lagrangian-Eulerian (ALE) moving-mesh method is used to handle the gas domain where there is a mesh deformation. The maximum electric field applied to the material is limited by the breakdown of the film, which occurs at fields larger than 400 V/μm [93]. The maximum amplitude of the electric field here is 150 V/μm, which reduces the chance of the film's breakdown due to the existance of defects. The detailed effect of the electric field on the system performance is discussed in the following section.

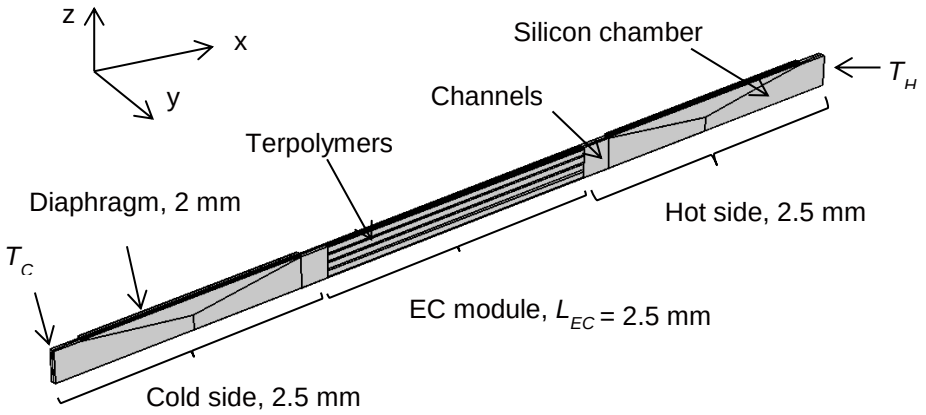

Figure 5.3 Computational region of the EC cooling device.

5.3.3 Results and discussions

In this section, the effects of the electric field applied to the EC module, the operating frequency, and the temperature span are investigated. The geometry design is also discussed for improving the cooling capacity of the cooler.

For the electric field, a smooth trapezoidal waveform is used, as shown in Fig. 5.4. Two parameters are important: (i) Δt_1 is the transit time when the electric field rises from zero to E_{max} or drops from E_{max} to zero. (ii) Δt_2 is the time lag between the diaphragm motion and the electric field applied to the EC material.

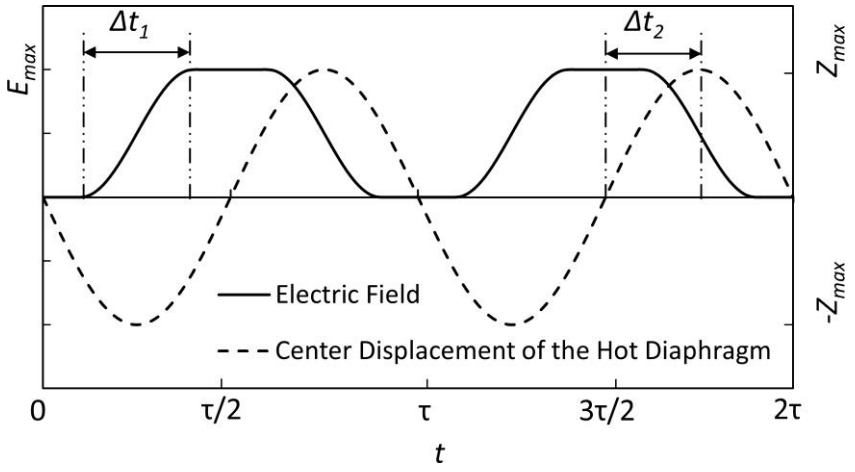

Figure 5.4 The smooth trapezoidal waveform of electric field applied to the EC module and the motion of the center point for the hot diaphragm. τ is the period of a cycle. E_{max} is the amplitude of the electric field. Z_{max} is the maximum amplitude of the hot diaphragm motion. Δt_1 is the transit time when when the electric field rises/drops. Δt_2 is the time lag between the diaphragm motion and the electric field in the EC module.

The cooling power density of the EC element is the space-averaged heat flux coming into the cold side from the cold end of the system. One example of the cooling power density as a function of time is shown in Fig. 5.5. Steady state is reached after 7 cycles when the operating frequency is 10 Hz, heat source temperature T_C = 295.15 K, Δt_1 = 0.02 s, and Δt_2 = 0.025 s. The temperature contours at two different times in the tenth cycle are shown in Fig. 5.6. The results when the time is 0.925 s (9.25τ, where τ is the period of the cycle), are shown in Figs. 5.6(a) and the results at t = 0.975 s (9.75τ) are shown in Figs. 5.6 (b). At t = 0.925 s, the hot diaphragm achieves the minimum displacement and the cold diaphragm moves to the top position. The electric field applied to the terpolymer is turning on, the temperature of the terpolymer is increasing, and heat is being transferred to the fluid from the terpolymer. At t = 0.975 s, the diaphragm positions are reversed, and the electric field applied to the terpolymer is turning off. Thus, the temperature of the polymer is dropping, and the heat is being transferred to the polymer from the fluid.

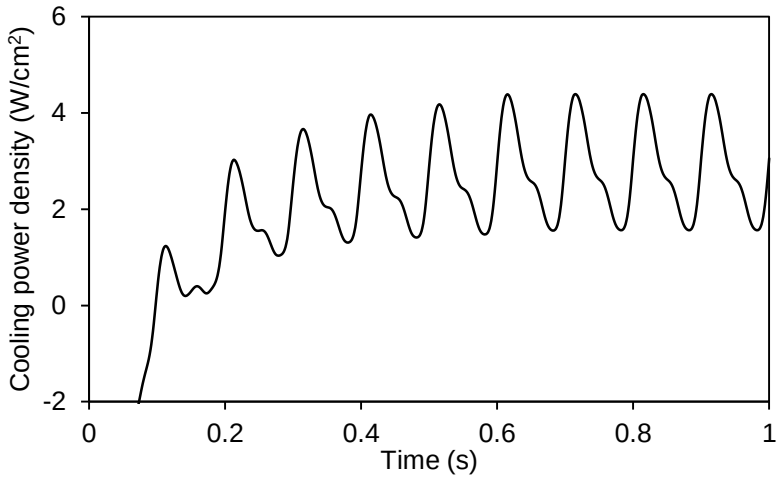

Figure 5.5 Cooling power density, which is space-averaged on the cold end surface of the element, versus time. The operating frequency is 10 Hz, heat source temperature T_C is 295.15 K, Δt_1 is 0.02 s, and Δt_2 is 0.025 s. The heat flux is positive, which indicates the heat flow direction is from the cold side to the hot side.

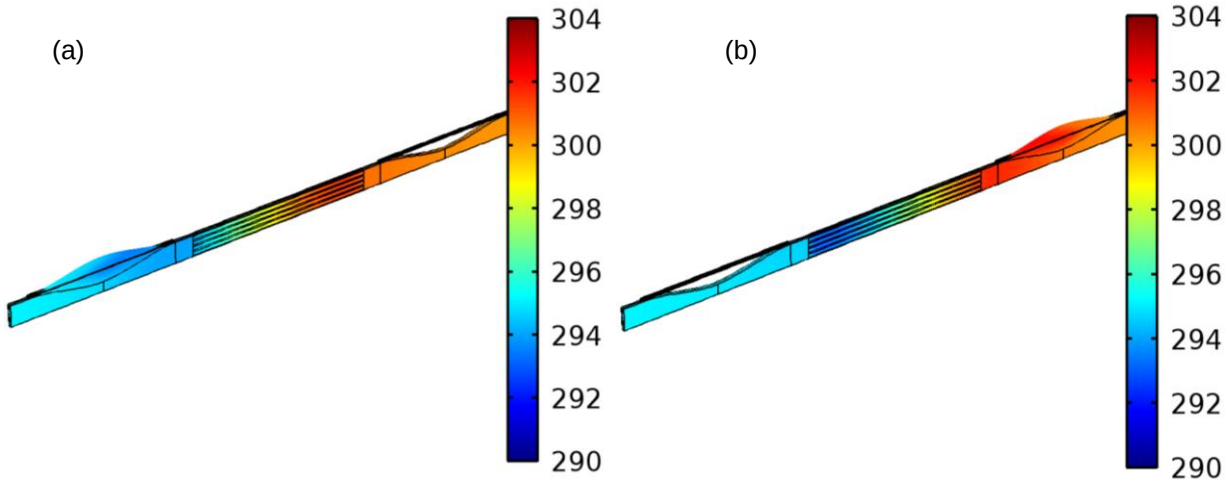

Figure 5.6 Distributions of temperature in the x direction in the element: (a) t = 0.925 s; (b) t = 0.975 s. At t = 0.925 s, the hot diaphragm is at the minimum displacement, and the cold diaphragm is at the maximum displacement. At t = 0.975 s, the diaphragm positions are reversed. The operating frequency is 10 Hz, heat source temperature T_C is 295.15 K, Δt_1 is 0.02 s, and Δt_2 is 0.025 s.

5.3.3.1 Effect of the applied electric field

It is found that reducing the transit time Δt_1 inceases the cooling power, as shown in Fig. 5.7 (a). At T_C = 295.15 K, when Δt_1 is reduced from 0.3 τ to 0.1 τ and Δt_2 is 0.25 τ, the cooling power density increases from 0.3 W/cm^2 to 0.36 W/cm^2 at 1 Hz, and increases from 3.22 W/cm^2 to 3.61 W/cm^2 at 20 Hz. In Fig. 5.7 (b), the effect of the time lag between the diaphragm motion and the electric field applied to the EC module is shown. When Δt_2 changes from 0.15 τ to 0.35 τ, a maximum value of the cooling power density is found to be 0.34 W/cm^2 at Δt_2 = 0.25 τ for a 1 Hz operating frequency. At 20 Hz, the maximum cooling power density is 3.48 W/cm^2 and still occurs at Δt_2 = 0.25 τ. A 90˚ phase lag between the diaphragm motion and the electric field gives the best cooling power of the system. The reason is that at a 90˚ phase shift, when the flow direction starts to change, the electric field applied to the EC material is turning on/off at the same time. The temperature of the EC material changes simultaneously and thus the fluid transfers the heat with the EC material more effectively, achieving a larger cooling power.

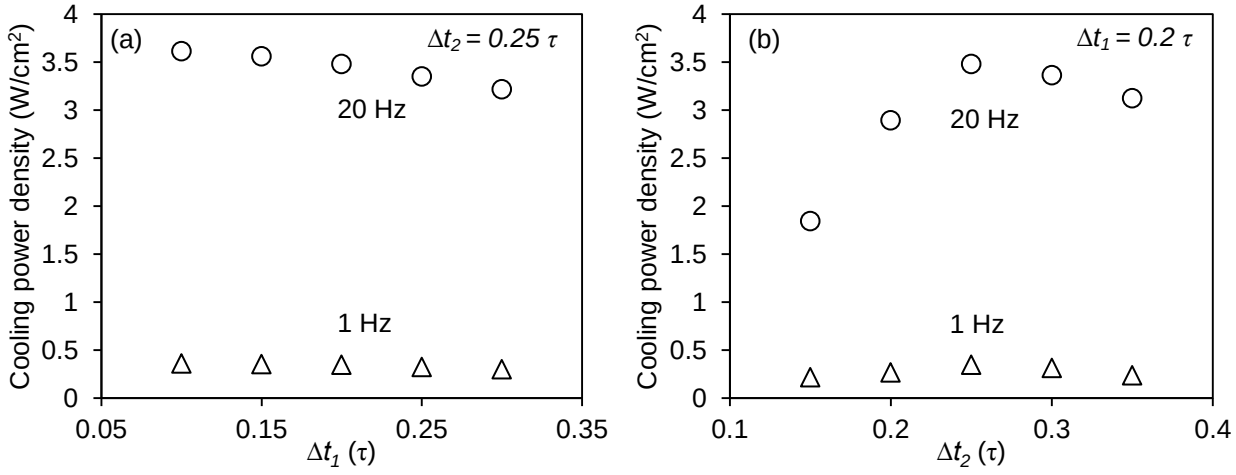

Figure 5.7 Time-averaged cooling power densities due to the change of (a) transit time (Δt_1) (b) time lag between the diaphragm and the electric field (Δt_2). The operating frequency is 1 Hz or 20 Hz. T_C is 295.15 K.

5.3.3.2 Geometric design

- *EC material thickness*

The EC terpolymer layer thickness is optimazied in this part to achieve a large cooling power. The EC channel height is 40 μm, the EC length is 2 mm, the fin width is 25 μm and the channel width at outlet of chanbers is 50 μm. Five EC channels and six EC polymer layers are placed in the EC module. The ratio of chamber depth to EC module height is fixed to be 0.577, as shown in Table 5.3.

Table 5.3 The chamber depths and EC module heights with different EC polymer thickness

EC polymer thickness (μm)	Chamber depth(μm)	EC module height (μm)
10	150	260
20	185	320
30	219	380
40	254	440

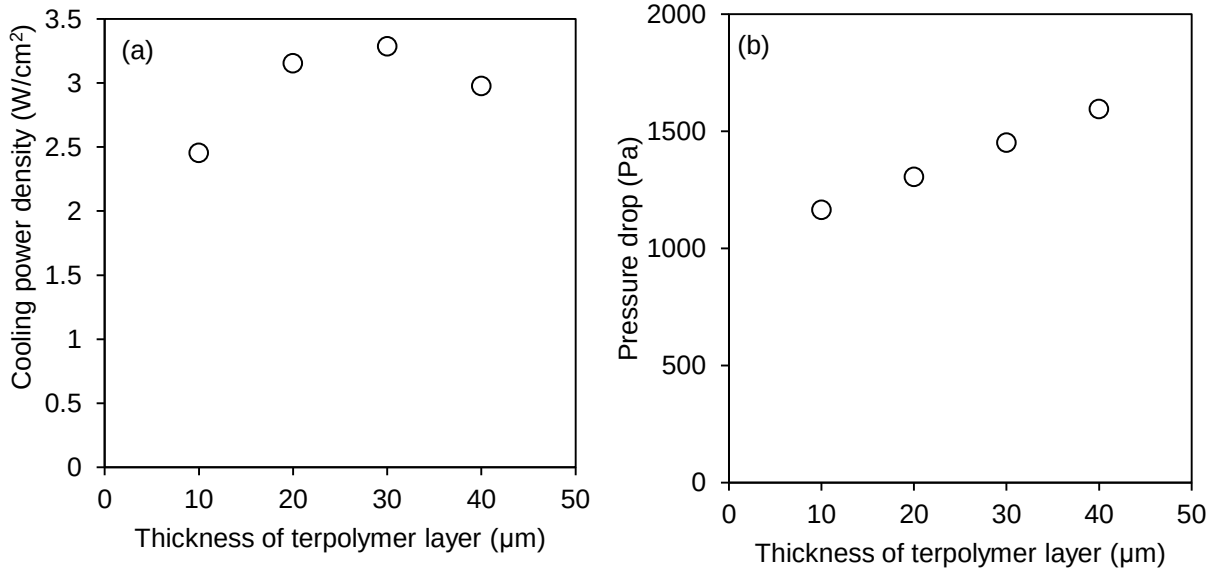

Figure 5.8 (a) The cooling power density and (b) pressure drop with different EC layer thickness at a frequency of 10 Hz.

The cooling power densities and pressure drop with different EC layer thickness at a frequency of 10 Hz are plotted in Fig. 5.8(a) and (b). With the increase of the EC polymer thickness, the pressure drop is increasing, while the cooling power has an optimal value. In this design, a 20 μm thick terpolymer is chosen for the EC module.

- *EC module length*

Cooling power densities and pressure drop with different EC module lengths are plotted in Fig. 5.9 (a) and (b). With the increase the EC module, the cooling power and pressure drop are increased. However, the cooling power comes to saturate when the EC module length exceeds 2.5 mm.

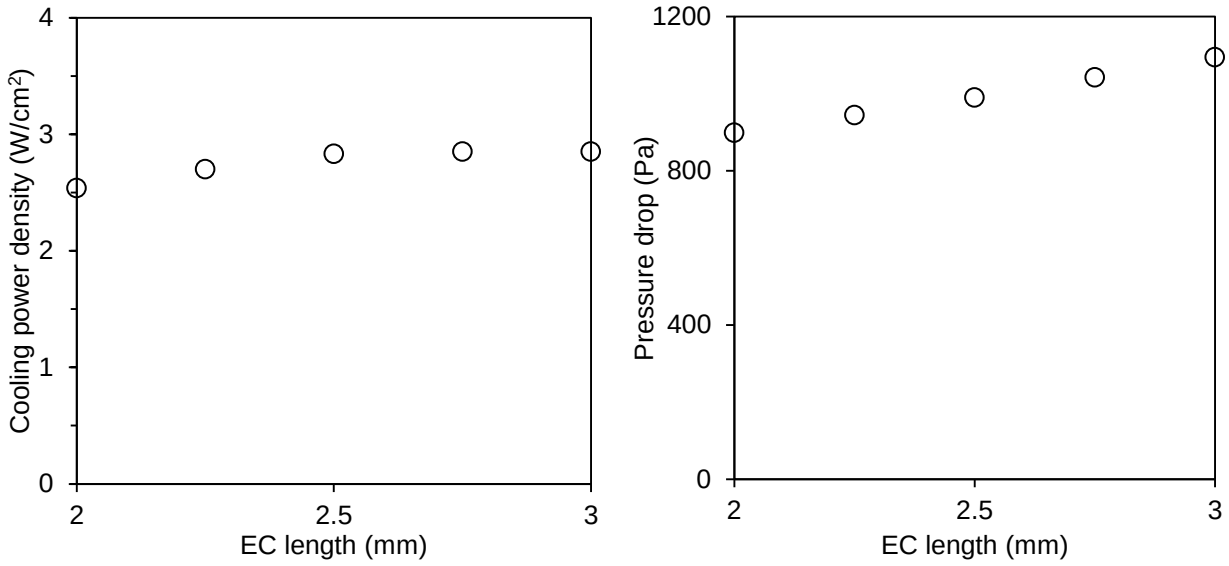

Figure 5.9 (a) The cooling power density and (b) pressure drop with different EC module lengths at a frequency of 10 Hz. The EC channel height is 50 μm, the fin width is 50 μm and the channel width at outlet of chambers is 50 μm. Four EC channels and five EC polymer layers are placed in the EC module. The middle layer thickness of EC material is 20 μm and the top and bottom layers thickness are 10 μm.

- *Widths of fins and channels at the outlet of chambers*

Channels are openned at the outlet of chambers for allowing the fluid to pass. The fins between channels are connected to the silicon substrate to provide a sufficient heat transfer

between hot/cold chambers and the pumped fluid. The widths of fins and channels are crictical to affect the cooler performance, including the thermal performance and electrostatic pump behavior. As shown in Fig. 5.10 (a), the cooling power densities with fin and channel widths of 40 - 60 μm at a frequency of 10 Hz are shown. The channel width effect on the cooling power density in this range is small. However, from Fig. 5.10 (b), the pressure drop at a channel width of 40 μm is much higher.

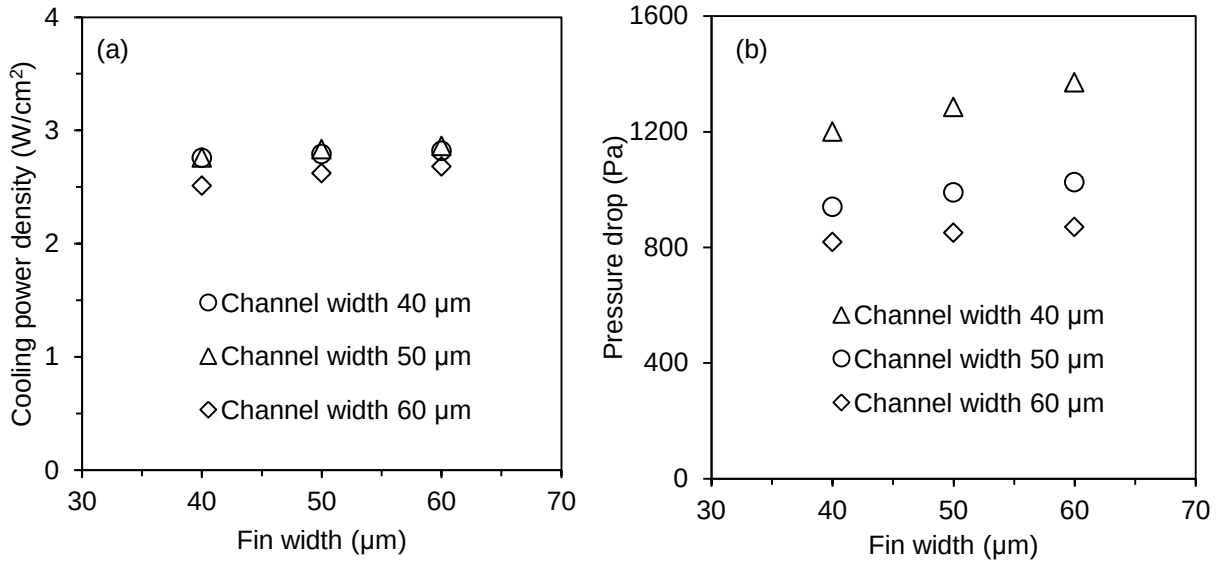

Figure 5.10 (a) Cooling power density (b) Pressure drop vs width of fins at outlet of chambers with different channel widths. The frequency is 10 Hz. Temperature span is 5 K. EC module length is 2.5 mm. EC channel height is 50 μm.

- *EC channel height*

Two designs with different EC channel heights are compared. For the EC channel height of 50 μm, the number of EC channels is 4 and the number of EC polymer layers is 5. The middle layer thickness of EC material is 20 μm and the top and bottom layers thickness are 10 μm. The total height of EC module is 280 μm. For the channel height of 40 μm, the number of EC channels is 5 and the number of EC polymer layers is 6. The total height of EC module is 300 μm. For both cases, the fin width is 50 μm and the channel width at outlet of chanbers is also 50

μm. The EC module length is 2.5 mm. The cooling power densities for 40 and 50 μm EC channel heights at a frequency of 10 Hz are 3.10 W/cm^2 and 2.83 W/cm^2. The pressure drops are 1270 Pa and 990 Pa, respectively. When the EC channel height is reduced from 50 μm to 40 μm, the cooling power increases about 9.5 %, while the pressure drop increases about 28.3 %. The EC channel of 50 μm is chosen for the later analysis.

5.3.3.3 Effect of the operating frequency

The effect of the operating frequency on the cooling power density is shown in Fig. 5.11 (a). The transit time Δt_1 is 0.2τ, the time lag Δt_2 is 0.25τ, and T_C is 295.15 K. From this figure, we can see that the cooling power density increases from 0.34 W/cm^2 to 3.48 W/cm^2 when the operating frequency increases from 1 Hz to 20 Hz. After 20 Hz, the cooling power tends to decrease. The system *COP* is degfined by

$$COP = \frac{Q_C}{Q_H - Q_C}, \tag{5.4}$$

where Q_H and Q_C are the heat fluxes at the hot and cold ends. The variation of *COP* with operating frequency is plotted in Fig. 5.11 (b). The *COP* first increases and then drops when the operating frequency is increased from 1 Hz to 30 Hz. When the frequency is higher than 10 Hz, the cooling power tends to saturate, as shown in Fig. 5.11(a), which hurts the *COP*. The maximum *COP* is 4.6 and occurs aroung a frequency of 10 Hz.

The main input work from the diaphragm actuators is to overcome the fluid pressure drop in the system. The maximum pressure drop is 990, 2000, and 3040 Pa when the operating frequency is 10, 20, and 30 Hz. Below 30 Hz, the work loss caused by the pressure drop is small, thus the pressure drop does not affect the *COP* of the system much (less than 1%). However,

when the pressure drop is higher, the voltage required to drive the diaphragms is larger. When the operating frequency is more than 10 Hz, the benefit of further increase to the cooling power is small and the penalty of the pressure drop is large.

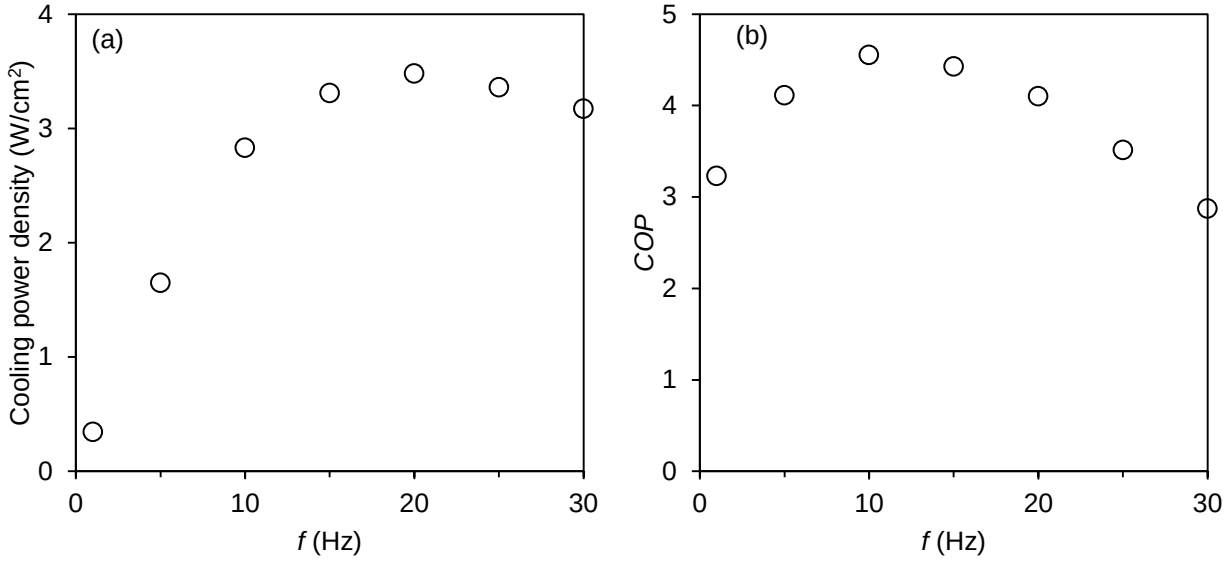

Figure 5.11 (a) Time-averaged cooling power density (b) *COP* as a function of operating frequency. The transit time Δt_1 is 0.2τ, the time lag Δt_2 is 0.25τ, and T_C is 295.15 K.

5.3.3.4 Effect of the temperature span and the electric field amplitude

From the previous section, the maximum cooling power of the system comes to saturation around a frequency of 20 Hz and the maximum *COP* occurs at 10 Hz. In this section, the effect of the temperature span (i.e., the externally-imposed temperature difference between the heat sink and the heat source) is studied. We consider different electric field amplitudes when the heat sink temperature is fixed at 300.15 K and the operating frequency is 10 Hz, which is near the frequency where the maximum cooling power and *COP* occur. In addition, the operating frequency is directly related with the voltage to drive the diaphragm, and the driven voltage can not exceed the breakdown voltage of PDMS. According to the analysis of diaphragm modeling in the next section, the operating frequency is designed to be 10 Hz.

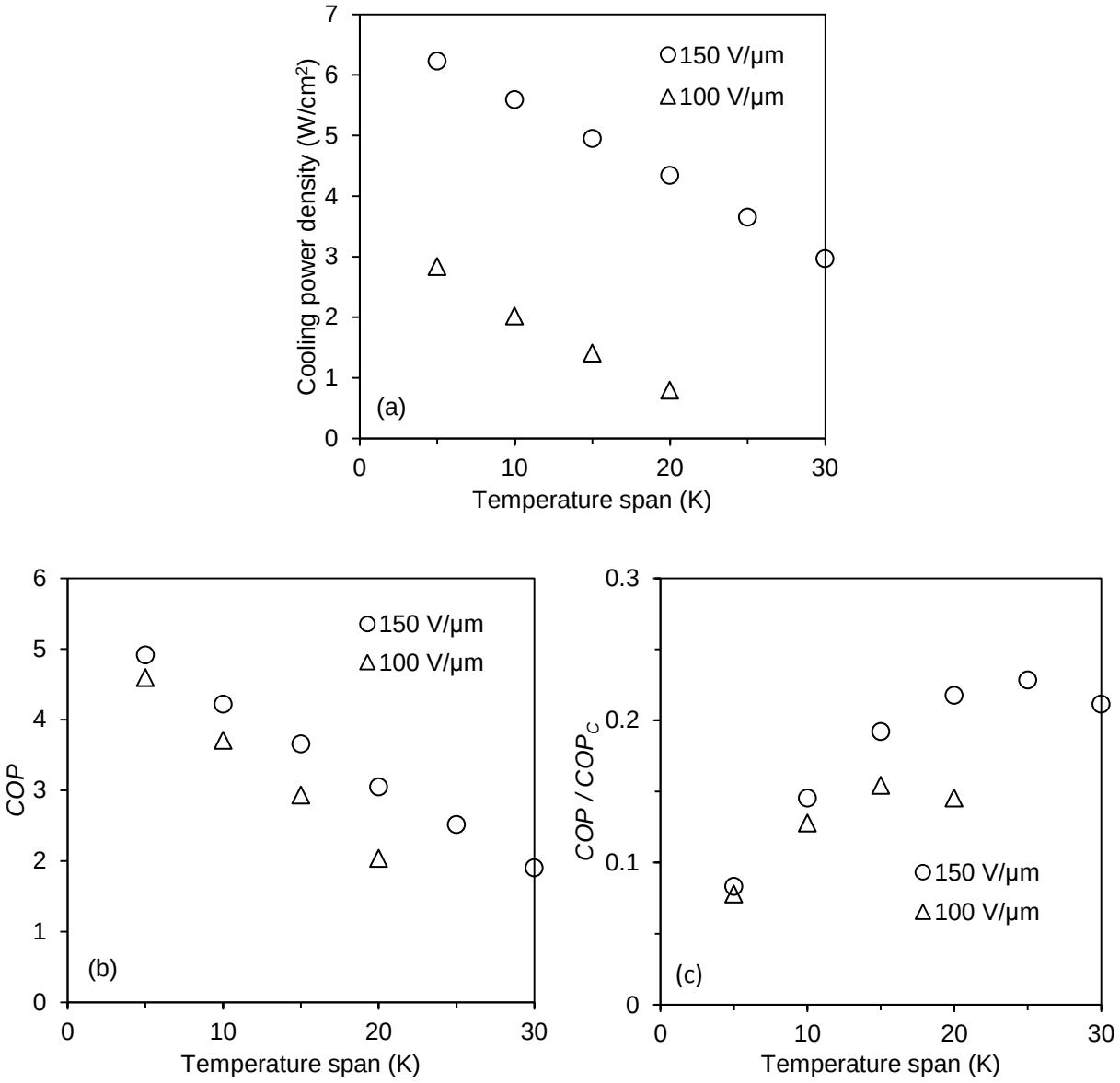

Figure 5.12 (a) Time - averaged cooling power density, (b) system *COP* and (c) percent of Carnot *COP*: COP/COP_C vs. the temperature span between the heat sink and the heat source at different electric field amplitudes. The transit time Δt_1 is 0.2τ and the time lag Δt_2 is 0.25τ. The operating frequency is 10 Hz.

The results for the cooling power density, *COP*, and the percent of Carnot *COP* are plotted in Fig. 5.12. As the temperature span increases for a given electric field amplitude, the cooling power and *COP* decrease, and the percent of Carnot *COP* has a peak value. As the electric field amplitude increases, the percent of Carnot *COP* increases and the maximum occurs

at a larger temperature span. With an increase of the electric field, the cooling power and *COP* increase. At 100 V/μm, the maximum percent of Carnot *COP* is 15.4% for a temperature span of 15 K. There is no cooling load when the temperature span exceeds around 25 K. If the electric field is 150 V/μm, a *COP* of 3.65 and a cooling power density of 4.95 W/cm^2 are achieved for a temperature span of 15 K. Generally, the efficiency loss is mainly due to the thermal resistance from the heat source/sink to the chamber region, as shown in the temperature distribution in Figs. 5.6. For comparison, in a standard design of a thermoelectric cooler (i.e., the material thickness is larger than 1 mm), the cooling power density is 4 W/cm^2 and the best *COP* is 2.85 when the *ZT* of the material is unity and the temperature difference is 15 K [5].

5.4 Diaphragm modeling and multiphysics simulation

In the previous section, the diaphragm motion is assumed to be sinusoidal for the thermal system modeling. However, in this design, the diaphragm is made of PDMS membrane embedded with electrodes, and is driven by electrostatic force. Thus, the detailed motion of diaphragm is investigated here and the effect of the diaphragm motion on the system performance is explored by finite element simulations. This part is a joint work with Jinsheng Gao.

5.4.1 PDMS Diaphragm modeling

5.4.1.1 Mooney Rivlin model

In the linear elastic model, a linear relationship between the stress and strain is assumed. PDMS is a rubber-like material and can not be described by linear elastic models. For this material, which is defined as a hyperelastic material [94], the stress-strain relationship is non-linear and incompressible, and it is derived from a strain energy density function,

$$\boldsymbol{S} = \frac{\partial W}{\partial \boldsymbol{E}}, \tag{5.5}$$

where W is the strain energy density function, $\boldsymbol{S}$ is the second Piola–Kirchhoff stress, and $\boldsymbol{E}$ is the Lagrangian Green strain.

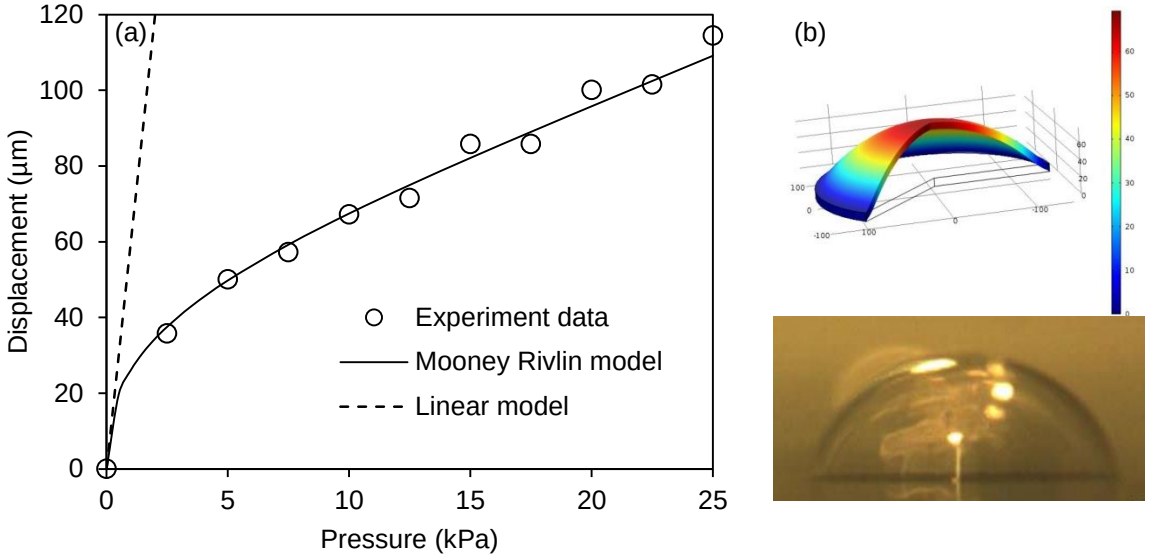

Figure 5.13 (a) Displacement vs pressure comparisons between the linear elastic model, Mooney Rivlin model, and experimental values [97]. (b) Comparison of PDMS membrane deformation shape between the finite element simulation based on Mooney Rivlin model and experimental result [97].

Mooney Rivlin model [95,96] is a recognized hyperelastic model to describe the strain-stress behavior of a rubber material, such as PDMS. The comparison between the linear elastic model result, Mooney Rivlin model result, and the experimental result [97] for a PDMS membrane is shown in Fig. 5. 13 (a). Displacement vs pressure relationship is obtained when a uniform pressure is applied to a circular PDMS membrane. The membrane diameter is 286 μm, and the thickness is 10 μm. For the linear elastic model, the Young's modulus is 0.5 MPa, and the Poisson's ratio is 0.5. The material constants used for the Mooney Rivlin model are C_1 = 75.5 kPa, C_2 = 5.7 kPa [97,98]. From the figure, the result based on the Mooney Rivlin model agrees

well with the experimental data. However, the result from the linear elastic model has a large deviation. The PDMS membrane deformed shapes between the finite element simulation based on Mooney Rivlin model and the experimental result are similar, as shown in Fig. 5.13 (b). Therefore, the Mooney Rivlin model is used to describe the behavior of PDMS membrane in this work.

5.4.1.2 Contact model

The substrate in hot and cold chambers are curved shapes. When the PDMS membrane is driven by electrostatic force, the PDMS membrane is going to snap in from the edge to the center. This means the PDMS membrane will contact the substrate gradually. Thus for this diaphragm modeling, a contact force model is added to act against the diaphragm after contact phenomenon. This contact force is defined by a spring force,

$$F_c = -k_c\, g, \text{ if } g < 0, \tag{5.6}$$

where F_c is the contact force, k_c is the spring constant, and g is the gap between the diaphragm and substrate. The spring constant is determined by the diaphragm Young's modules and the insulating layer thickness between the electrode and the diaphragm contact surface.

5.4.2 Porous medium model

For simplying the multiphysics simulation of the system coupled the thermal modeling and the diaphragm modeling with the electrostatics and the contact models, a 2D model is feasible. For capturing the features of channels at the outlet of chambers, a porous medium model is employed in this modeling. The detailed information about the porous medium model has been discussed in Section 3.4. In this design, both the widths of fins and channels are 50 μm,

and the porosity is 0.5. The key parameters for the fluid flow and heat transfer are two parameters, permeability κ and convection coefficient h_{fs}. Based on the simulation results for fins and channels, the permeability in this design is 1.87 $\times 10^{-10}$ m^2, and the convection coefficient is determined by

$$Nu_{D_h} = 3.18\, Re_{D_h}{}^{0.127}. \tag{5.7}$$

The defination of variables are shown in Section 3.4.

5.4.3 Multiphysics modeling

5.4.3.1 Computational setup

The computational region is shown in Fig. 5.14. The multiphysics modeling is coupled with electrostatics, solid mechanics (Mooney Rivlin model), contact model, fluid-solid interaction, porous medium, heat transfer models and moving mesh technique. The substrtate shape is a cubic curve, and the maximum height is 150 μm. The diaphragm diameter is 2 mm, and the thicknes is 13 μm. The material constants used for the present Mooney Rivlin model of PDMS membrane are C_1 = 321 kPa, C_2 = 0 kPa, and the Young's modulus is 1.93 MPa [99]. The diaphragms are driven electrostatically. The insulating layer thickness between the electrodes and the diaphragm contact surface is 2 μm. The EC module length is 2.5 mm, including 5 layers of terpolymer. For the middle terpolymers, the thickness is 20 μm. The thickness of top and bottom layers is 10 μm. The channel width between EC layers is 50 μm. The electric field amplitude applied to the EC material is 100 V/ μm. The thermal boundary conditions are similar to the thermal modeling in Section 5.3. The temperature at the hot end of the element is constant and is T_H = 300.15 K. The cold end has a constant temperature of T_C = 295.15 K. The remaining surfaces are thermally insulated. The initial temperature for the whole system is a linear profile in the x-direction (see Fig. 5.3). The no-slip condition is applied to the solid-liquid interfaces.

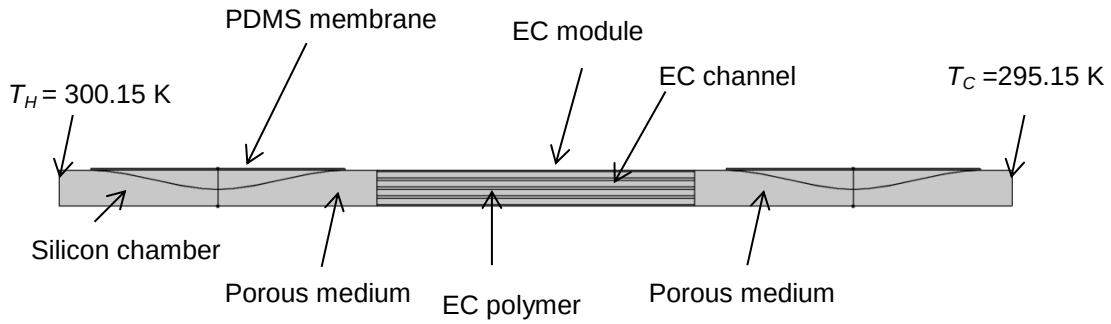

Figure 5.14 2D computational region of the EC cooling device coupled with multiple physics phenomena.

5.4.3.2 Results and discussions

When the voltage is applied to PDMS membrane, the membrane starts to snap in. The fluid in the chamber is pumped out and passes the EC channels. One example of the tempeature distributions of the system is shown in Fig. 5.15. The diaphragm motion and deformation are also displayed in these figures.

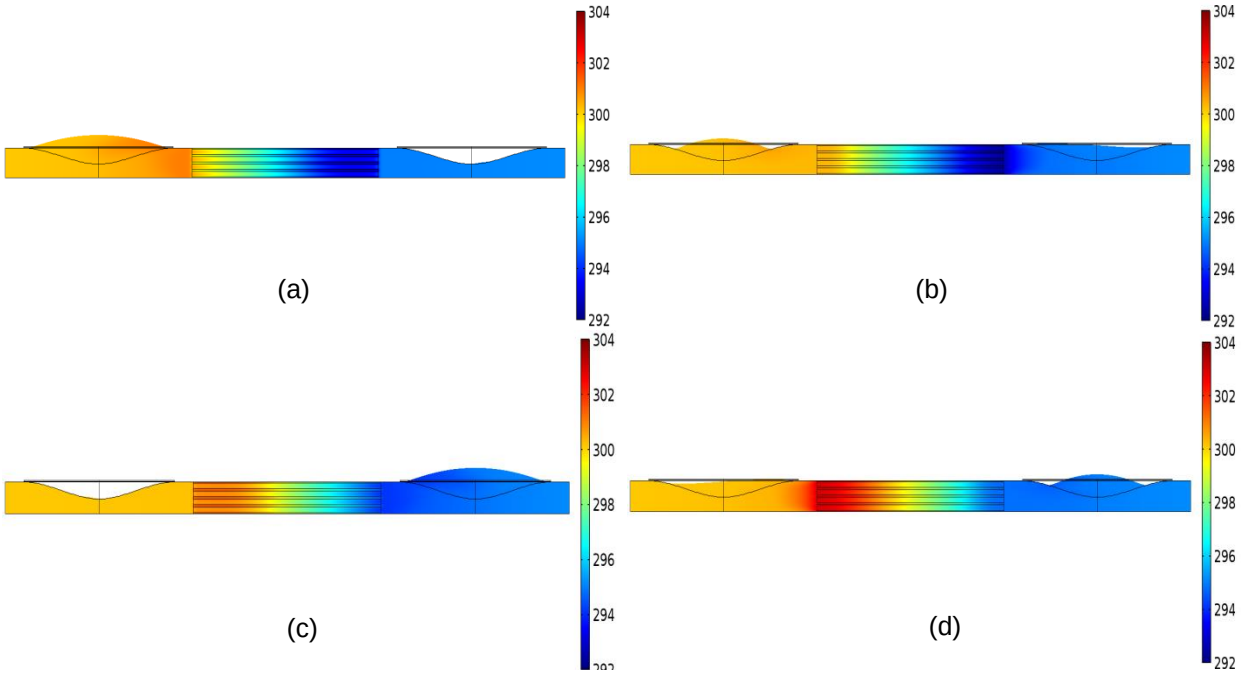

Figure 5.15 Temperature contours at different time when the diaphragm is driven electrostatically at an operating frequency of 5 Hz. (a) t = 1 s (b) t = 1.05 s (c) t = 1.1 s (d) t = 1.15 s.

The voltage applied to PDMS membrane in this case is 170 V and the operating frequency is 5 Hz. The spring constant k_c for the contact force is 5×10^{10} Pa/m. The volume variations of hot and cold chambers and the electric filed applied to EC materials are plotted in Fig. 5.16. A 90˚ phase lag is maintained between the chamber volume variations and the EC electric field, which is consistent with the condition set in Section 5.4.2. The volume variations of hot and cold chambers, corresponding to the driven voltage of hot and cold diaphragms, are plotted in Fig. 5.17. A phase lag of 270˚ is observed between them.

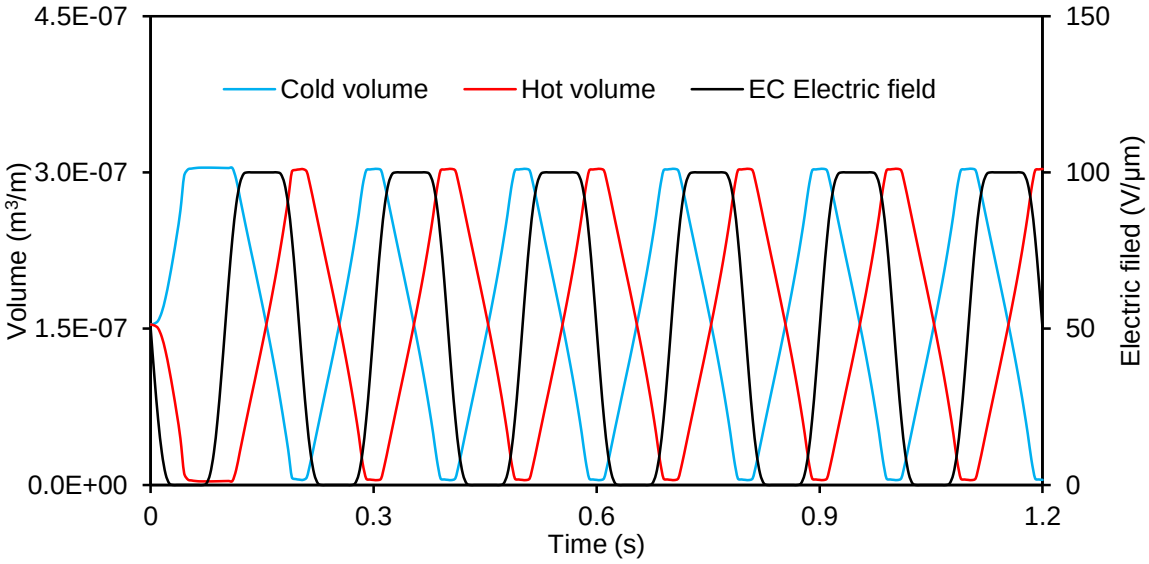

Figure 5.16 The volume variations of hot and cold chambers and the electric filed applied to EC materials.

The cooling power densities and the maximum pressure drop in the element in a frequency range of 1 to 10 Hz are plotted in Fig. 18 (a) and (b). A comparison between the current data and the thermal modeling data in Section 5.4.2 is also displayed and a good agreement is indicated between them. This means the diaphragm deformation and displacement do not have a significant effct on the thermal performance of electrocaloric cooler. The reason is that the fluid in the element is not compressed and the main function of the fluid is to transfer the heat between the heat source/sink and EC materials. Thus the thermal modeling modeling results

in Section 5.4.2 are reasonable even the diaphragm motion is assumed.

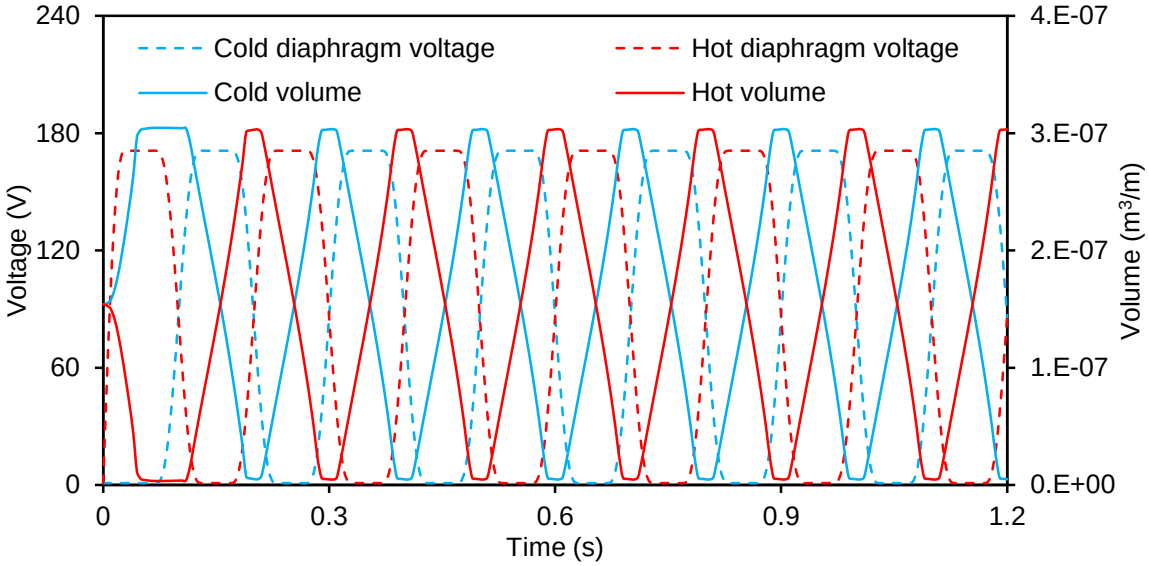

Figure 5.17 The volume variations of hot and cold chambers, corresponding to the driven voltage of hot and cold diaphragms.

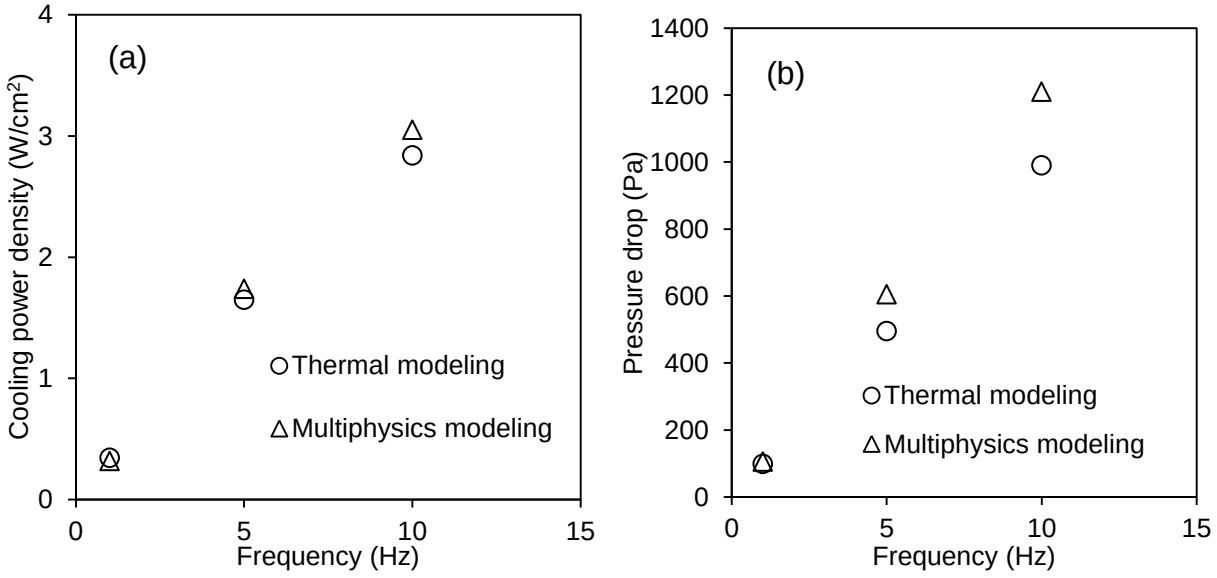

Figure 5.18 Comparisons of (a) the cooling power density and (b) pressure drop in a frequency range of 1 to 10 Hz between the thermal modeling results and multiphysics modeling results.

5.5 Summary

In this chapter, a new micro-scale refrigeration system based on EC effect has been designed. Finite element simulations were used to evaluate the system thermal performance that assumes that the hot and cold diaphragms have a sinusoidal motion with a 180˚ out of phase. The effect of the applied electric field was studied. The transit time over which the electric field changes has a small effect on system cooling power, while the time lag between the electric field and the diaphragm motion is found to play an important role. The geometric dimensions of EC module were studied to improve the cooling power of the system. The maximum cooling power density tends to saturate above an operating frequency of 20 Hz and the best *COP* occurs at 10 Hz. The results of effects of temperature span and electric field amplitude applied to EC materials, indicates that a cooling power density of 4.95 W/cm^2 and a *COP* of 3.65 are achieved when the system is operated at a temperature span of 15 K. Larger temperature difference between the heat sink and heat source or higher cooling power density could be achieved by increasing the magnitude of the electric field applied to the EC material. The multiphysics modeling that considers the PDMS diaphragm deformation and displacement was successfully performed to validate the thermal modeling results. It is demonstrated that the system performance is not influenced by the diaphragm local behaviors.

Chapter 6 Electrocaloric characterization of P(VDF-TrFE-CFE) terpolymer

6.1 Introduction

Recently, a large EC effect was discovered in thin films of $PbZr_{0.95}Ti_{0.05}O_3$ [29], a poly(vinylidene fluoride-trifluoroethylene) [P(VDF-TrFE)] copolymer [30], and a P(VDF-TrFE-chlorofluoroethylene) [P(VDF-TrFE-CFE)] terpolymer [30]. The P(VDF-TrFE-CFE) terpolymer demonstrates a adiabatic temperature change of 7 K at an electric field of 100 V/μm near room temperature [85] and is easily and economically fabricated, making it favorable for mass production [90]. These findings point to the potential of applying EC cooling in micro-devices using polymer thin films.

Direct and indirect techniques can be applied to measure the EC effect. In the indirect measurement, a differential scanning calorimeter is used to measure the heat flow under a high electric field and isothermal conditions [100,101]. This technique is best suited to bulk materials as the output heat flow signal for a thin film sample is very small. Jia and Ju [102] reported an approach for characterizing the EC effect in a thin film sitting on an insulating substrate. In this approach, the temperature response of a resistance thermometer deposited on the bottom of the EC film is monitored as an electric field is turned on and off. In the reported measurements, the temperature change is less than 10% of that expected because the heat loss from the EC film to the substrate is large. Lu et al. [88] employed a specially-designed calorimeter to measure the EC effect in a thin film. In this approach, the heat generated in the EC film is compared with the heat generated from a standard reference resistor. More recently, an infrared camera [90] was used to measure the temperature change in a 50 μm thick polymer film under the direct application of an electric field.

In this chapter, the infrared imaging technique is used to directly measure the transient temperature response of thin films of a P(VDF-TrFE-CFE) terpolymer (11-12 μm thick) under varying electric fields near ambient conditions. For such a thin film, the convection heat transfer between the thin film sample and the air is not negligible and must be included in the analysis. A significant percentage of the adiabatic temperature change (about 50%) is still realized, however, which is much larger than that obtained in other techniques [100-102]. The ramp time of the applied voltage is varied to quantify the heat transfer between the sample and the ambient environment and to obtain the adiabatic temperature change. The frequency dependence of the EC effect is investigated and the film stability is also explored.

6.2 Experimental details

Film samples from (i) Piezotech [France, P(VDF-TrFE-CFE): 62.6/29.4/8 mol.%, 11 μm thick] and Carnegie Mellon University (CMU, same composition as Piezotech samples, 12 μm thick) were tested. The CMU films were fabricated by Ying-Ju Yu in ACM group based on a solution-cast method following instructions from Piezotech. The polymer powder was first completely dissolved into methyl ethyl ketone and then the solution was cast on a silicon wafer and baked at a temperature of 50˚C overnight to evaporate the solvent. After drying, the film was immersed in water for two hours and then peeled off the wafer. The film was then suspended and annealed at a temperature of 100 ˚C for seven hours to improve crystallinity and remove residual solvent [85,90]. A 5 mm diameter circle of gold with a thickness of 100 nm was sputtered on both sides of the sample to act as the electrode, as shown in Fig. 6.1. To obtain the temperature map accurately, a 2 mm diameter circular area at the center of the electrode surface was coated with a 5 μm layer of carbon ink with to increase its emissivity to 0.7.

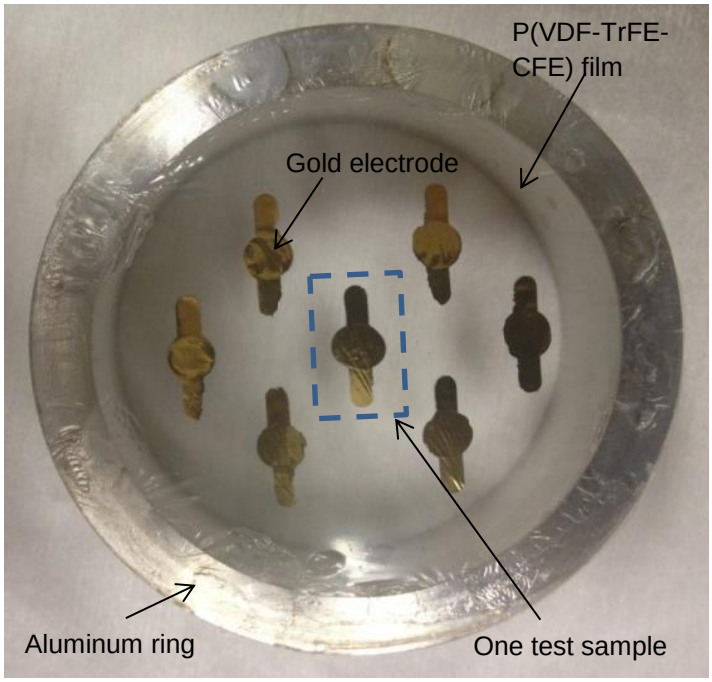

Figure 6.1 P(VDF-TrFE-CFE) terpolymer film with sputtered gold electrodes.

The test bed setup is shown in Fig. 6.2. To measure the EC effect, the film was suspended 1 mm above a thermal stage in air. Voltage pulses were supplied by a function generator (HP 33120a) and amplified by a high-voltage amplifier (Trek 2210). The current and voltage were measured by a source meter (Keithley 2400) and a multimeter (Agilent 34401a), and were collected by LabVIEW. The temperature images were recorded by a QFI InfraScope II system, which has a sample rate of 14 frames per second. The temperature error of infrared camera is ± 0.1 ˚C. The reported temperature is averaged over the ink-coated area.

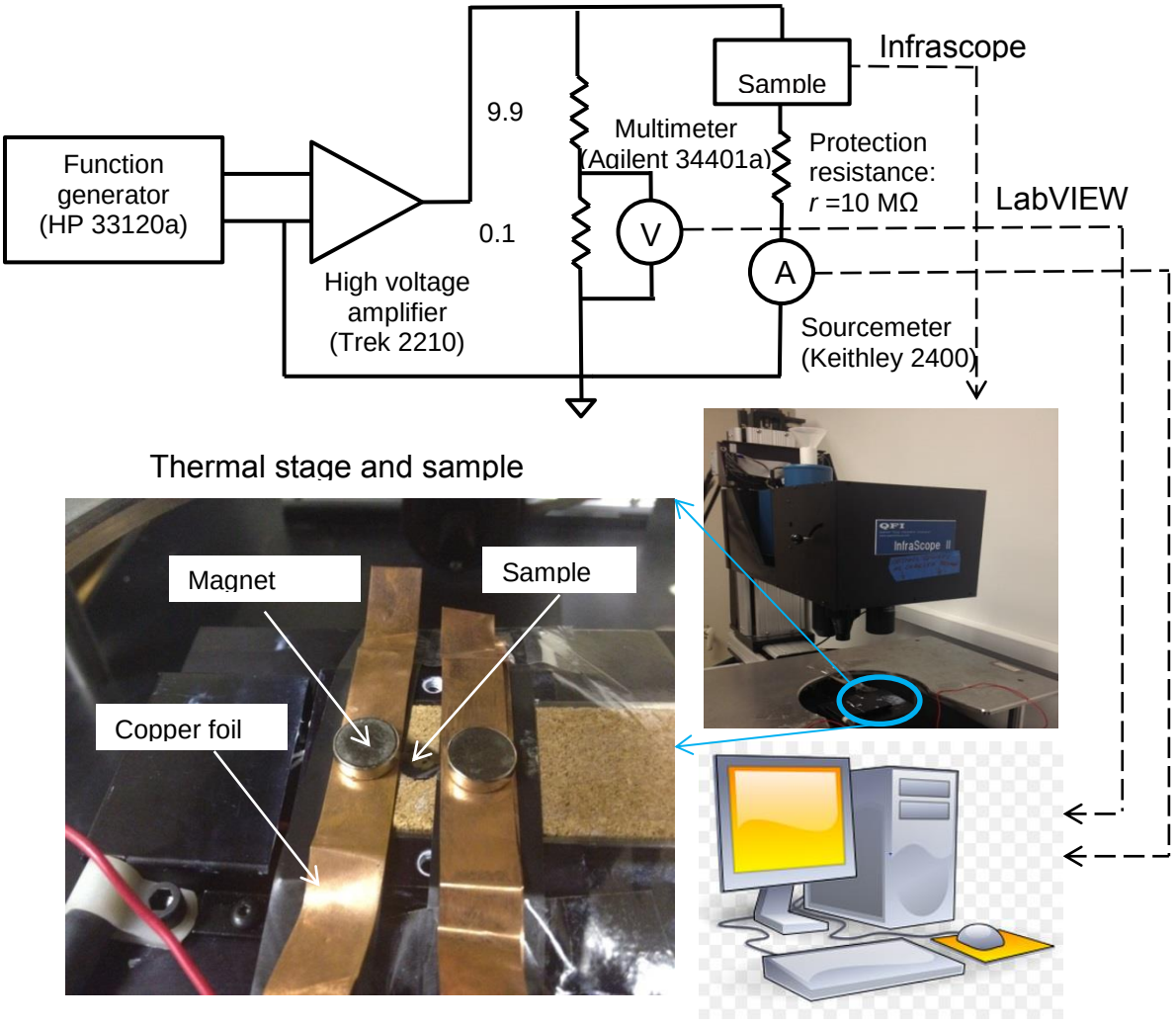

Figure 6.2 Test bed setup for the electrocaloric effect measurement of P(VDF-TrFE-CFE) thin film (joint work with Jinsheng Gao).

6.3 Experimental results

6.3.1 Measured results and the adiabatic temperature change

Three Piezotech samples and three CMU samples were tested at a stage temperature of 25 ˚C for maximum electric fields between 40 and 90 V/μm. For each test, three consecutive trapezoidal pulses with a period of 30 s were applied to check for repeatability. The ramp time of the voltage pulse was varied (0.8, 1.2, and 1.6 s) to quantify the heat transfer between the sample

and the air environment. A typical result of the current and temperature responses are shown in Figs. 6.3(a)-(b) and show a similar behavior. The current leakage for all samples is very small (10 ~ 30 nA when the voltage is applied for 15 s). Joule heating in the film is thus negligible, consistent with the temperature data ($T_3 = T_1$) in Fig. 6.3(b).

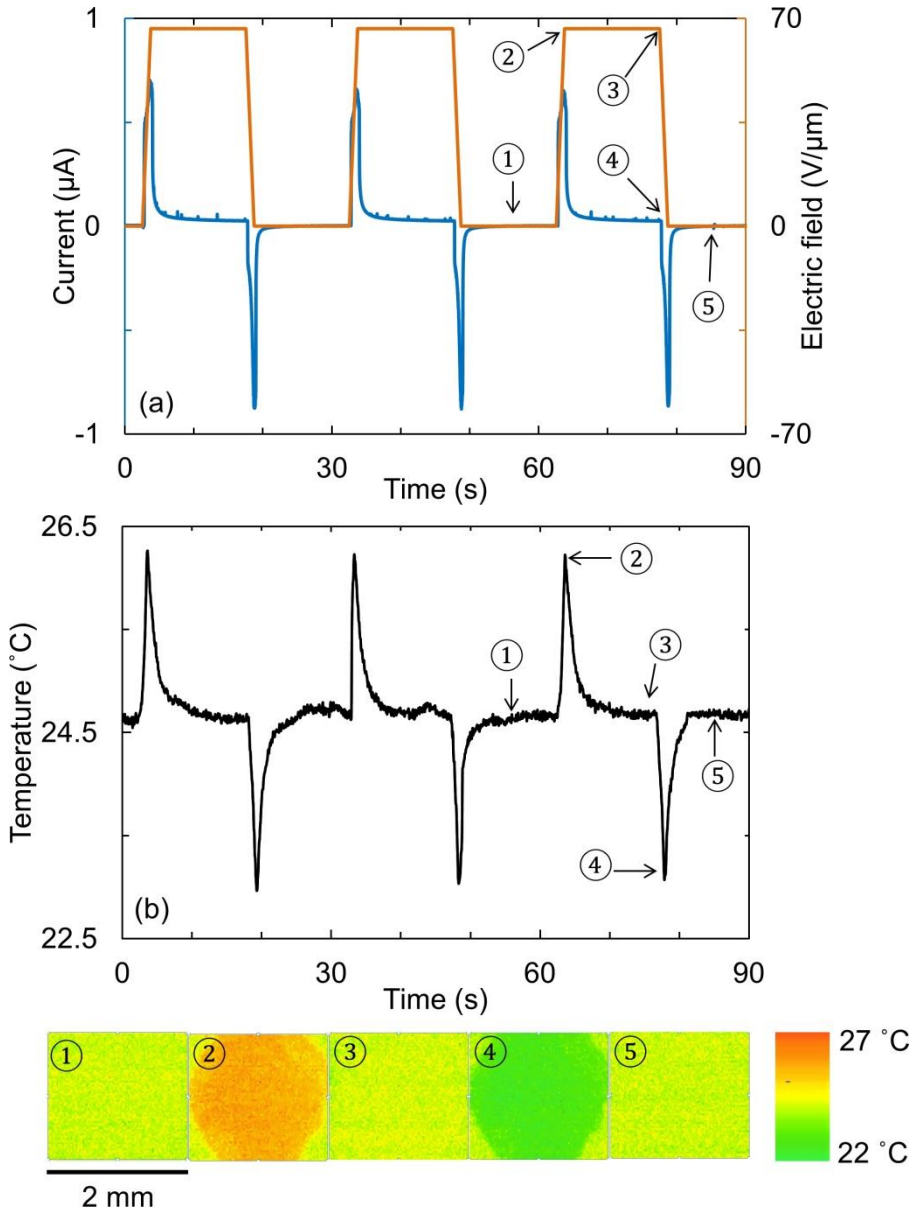

Figure 6.3 (a) Example of a trapezoidal electric field applied to the EC sample and the measured current. The ramp time of the electric field is 1.2 s and its maximum amplitude is 67 V/μm. (b) Infrascope-measured temperature images at different time in a cycle and the temperature as a function of time. The temperature changes abruptly when the electric field is ramping up and down (2 and 4).

The temperature response induced by the electric field change happens very fast (~milliseconds) [27]. The sample temperature thus immediately rises when the electric field is turned on [1 to 2 in Figs. 6.3(a) and 1(b)]. With the electric field still on, the temperature decreases exponentially back to the initial temperature due to the heat exchange between the air and the sample (2 to 3). When the electric field is turned off, the temperature quickly decreases below the initial temperature (3 to 4) and then rises exponentially back to the initial temperature (4 to 5).

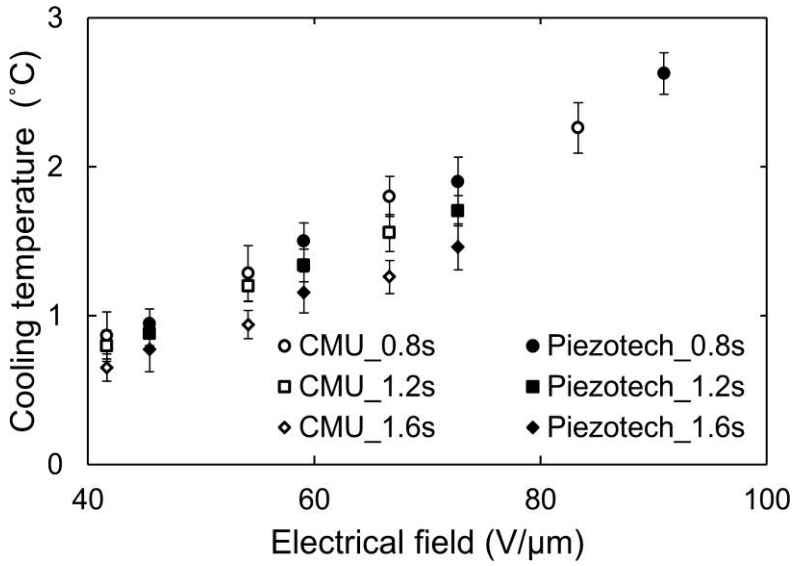

Figure 6.4 Measured cooling temperature for CMU and Piezotech samples as a function of the electric field at different voltage ramp times. The stage temperature is 25 ˚C for all measurements.

The measured cooling temperature induced by the EC effect at different ramp time of the voltages is plotted in Fig. 6.4. Consistent results are observed for the Piezotech and CMU samples from the figure. When the ramp time of the electric field is reduced, the cooling temperature increases as the heat loss due to the air is less in a shorter ramp time. The adiabatic temperature change of the terpolymer was calculated by estimating the heat transfer between the sample and the air. The computational process is describes as follows:

The governing equation when the electric field is changing is

$$cm\frac{\partial T}{\partial t} = hA\left(T_f - T\right) + m_p T\frac{\Delta S}{\Delta t}, (t \le \Delta t) \quad (6.1)$$

When $t > \Delta t$,

$$cm\frac{\partial T}{\partial t} = hA\left(T_f - T\right), \quad (6.2)$$

where T_f is the air temperature, ΔS is the entropy change of the electrocaloric material, Δt is the ramp time of the voltage applied to the electrocaloric material, h is the effective heat transfer coefficient between the sample and the air. A, m, and m_p are the surface area, the total mass of the ink-coated part of the sample, and the mass of polymer coated with ink. c is the effective specific heat of the ink-coated part of the sample. If the thickness of the sample film, the thickness of the ink, the specific heat of the film, the specific heat of the ink, the density of the film, and the density of the ink are th_p, th_i, c_p, c_i, ρ_p, and ρ_i, then the effective specific heat here is

$$c = \frac{c_p\rho_p th_p + c_i\rho_i th_i}{\rho_p th_p + \rho_i th_i}. \quad (6.3)$$

The effective heat transfer coefficient h was determined using the thermal time constant τ, which is expressed as

$$\tau = \frac{cm}{hA}, \quad (6.4)$$

based on Eq. (6.2). The thermal time constant was obtained from the measured temperature profile, as shown in Fig. 6.5.

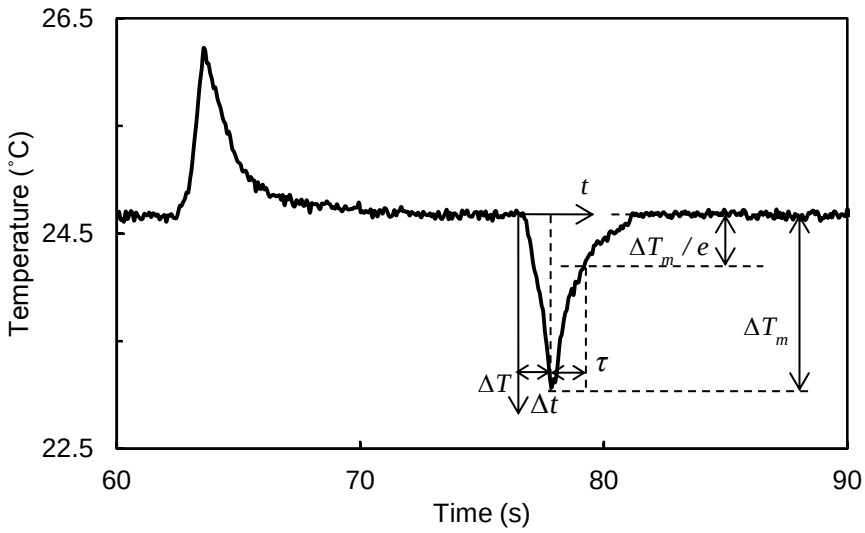

Figure 6.5 Measured temperature profile indicating the thermal time constant and the temperature variation when the electric field changes.

Solving the Eq. (6.1), the temperature of the sample is obtained by

$$\Delta T = \frac{hAT_f}{\left(\frac{m_p \Delta S}{\Delta t} - hA\right)}\left(e^{\frac{\left(\frac{m_p \Delta S}{\Delta t} - hA\right)t}{cm}} - 1 \right). \tag{6.5}$$

At $t = \Delta t$, the temperature change ΔT_m is

$$\Delta T_m = \frac{hAT_f}{\left(\frac{m_p \Delta S}{\Delta t} - hA\right)} \left(e^{(m_p \Delta S - hA\Delta t)/cm} - 1\right). \tag{6.6}$$

From Eq. (6.6), the entropy change ΔS was calculated. One example of the comparison between the measured data and the computational results is plotted in Fig. 6.6. Then the adiabatic temperature change was obtained and is plotted in Fig. 6.7 along with literature results. We found that the adiabatic temperature change over the electric field agrees well with that from Li et al. [85], Jia and Ju [102]. However, obvious deviations are observed with the data from Sebald et al. [90] when the electric field exceeds 70 V/μm.

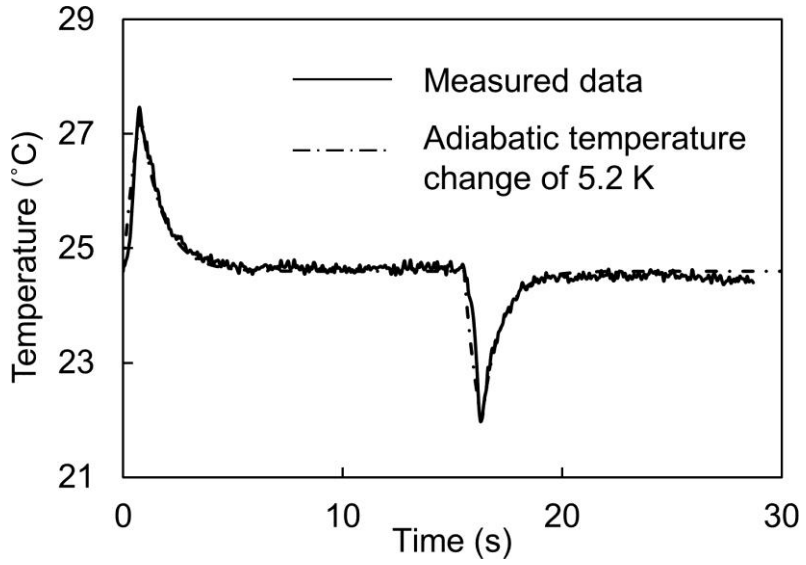

Figure 6.6 The comparison between the measured data and the computational result at an electric field of 90 V/μm.

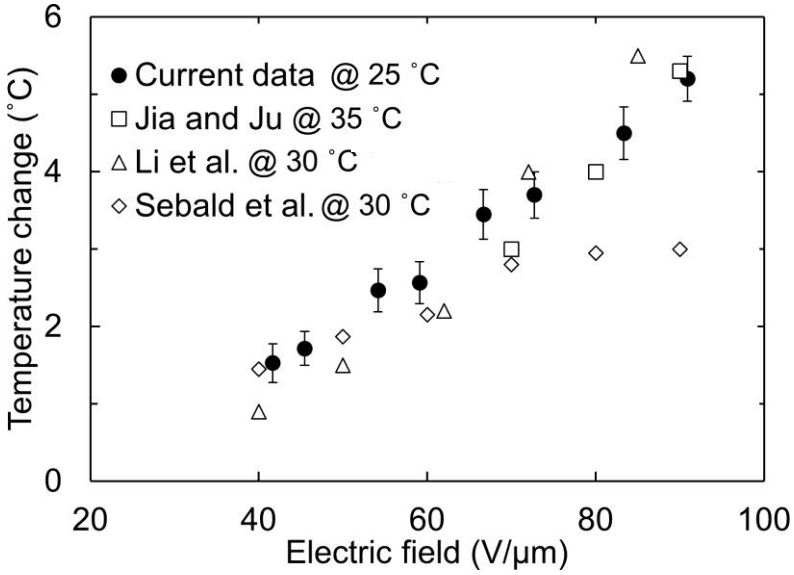

Figure 6.7 Adiabatic temperature change vs. electric field and comparison to literature results.

6.3.2 Effect of stage temperature and operating frequency

The temperature dependence of the EC effect of the P(VDF-TrFE-CFE) terpolymer is plotted in Fig. 6.8 for stage temperatures between 20 and 30˚C. The EC effect is increased by 10 ~ 20 % at a temperature of 30˚C, which consistent with the results reported in Ref. [85].

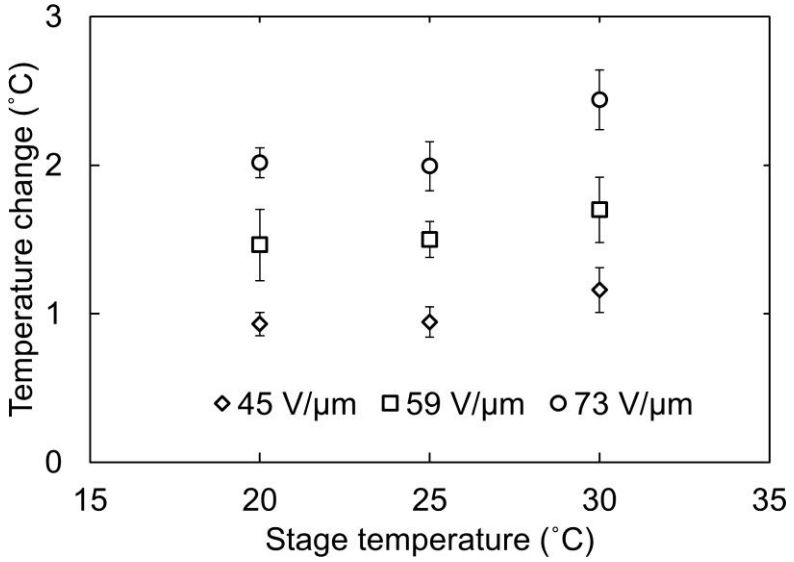

Figure 6.8 Measured cooling temperature at different stage temperatures. The ramp time of the voltage is 0.8 s.

The effect of the electric field frequency on the temperature change is shown in Figs. 6.9(a) and 6.9(b) for frequencies between 0.03 and 0.3 Hz. As shown in Fig. 6.9(a), the minimum temperature (i.e., location 4 in Fig. 6.3) increases with increasing frequency as the thermal time constant (~1 s) becomes larger than the period of the operating frequencies. The inset in Fig. 6.9(b) shows the temperature-time history for a frequency of 0.3 Hz. Note that the temperature does not return to the initial value during the air cooling/heating stages and that an offset average temperature is realized. Thus, the maximum and the minimum temperatures decrease compared to lower-frequency operation. The measured cooling temperature (ΔT) induced by EC effect when switching the electric field off is indicated in the inset figure, and this temperature change

as a function of the frequency is plotted in Fig. 6.9(b). We find that the measured temperature change does not change in the operating frequency range of 0.03 ~ 0.3 Hz, demonstrating that the EC effect in the P(VDF-TrFE-CFE) terpolymer is frequency-independent. The current result is promising, in that a practical device will operate in a frequency range of 1 - 10 Hz. For example, Gu et al. [32] fabricated a solid-state chip-scale electrocaloric cooler using a P(VDF-TrFE) polymer and tested it at 1 Hz.

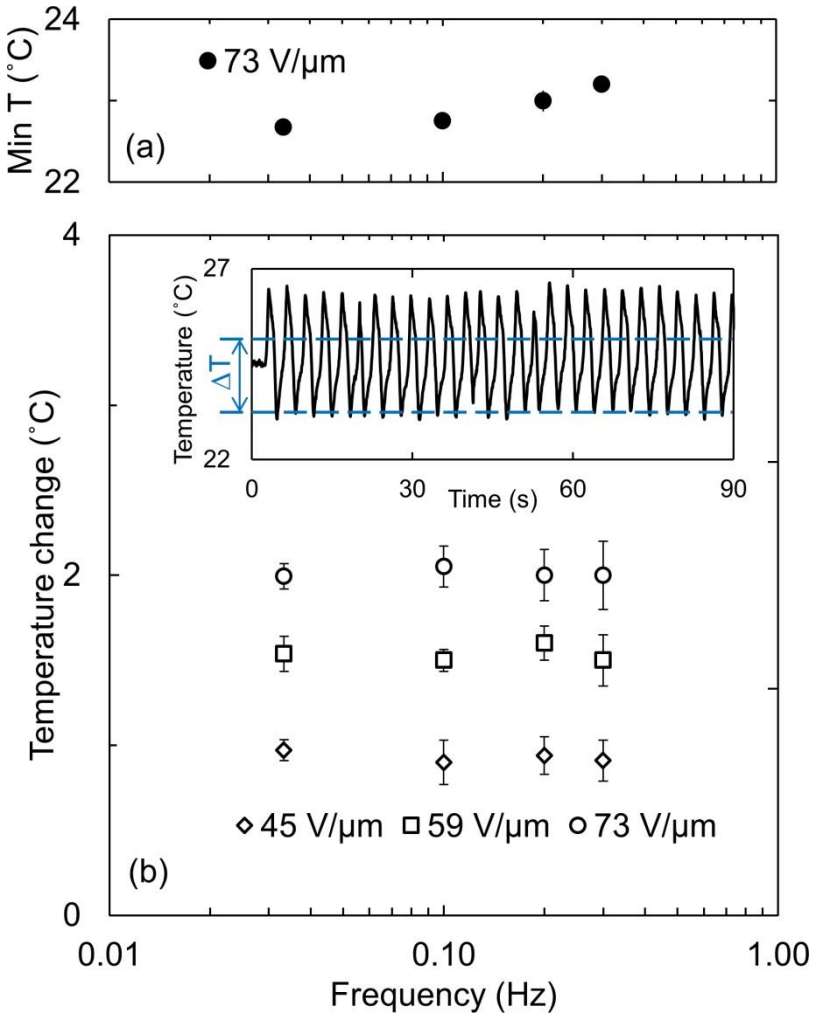

Figure 6.9 (a) Measured minimum temperature as a function of the operating frequency. (b) Measured temperature change when switching off the electric field with the operating frequency. A ramp time of 0.8 s is fixed at different frequencies for a fair comparison. The stage temperature is 25 ˚C. The inset is a plot of measured temperature when the operating frequency is 0.3 Hz and the electric field amplitude is 73 V/μm. ΔT is the temperature change when switching off the electric field.

6.3.3 P(VDF-TrFE-CFE) terpolymer thin film stability

The stability of the material was then assessed by conducting a 30 minute test of a sample. The operating frequency was 0.2 Hz and the amplitude of the electric field was 54 V/μm. The temperature history is plotted in Fig. 6.10. The temperature data was not measured continuously due to the limitation of the infrascope. The time spacing between adjacent data collection periods is 2 minutes. No failure was observed within 30 minutes. The maximum and the minimum temperature measured by the infrared camera are 25.6 ˚C and 23.7 ˚C. The performance is stable and demonstrates the potential of applying the P(VDF-TrFE-CFE) polymer in a microcooler application.

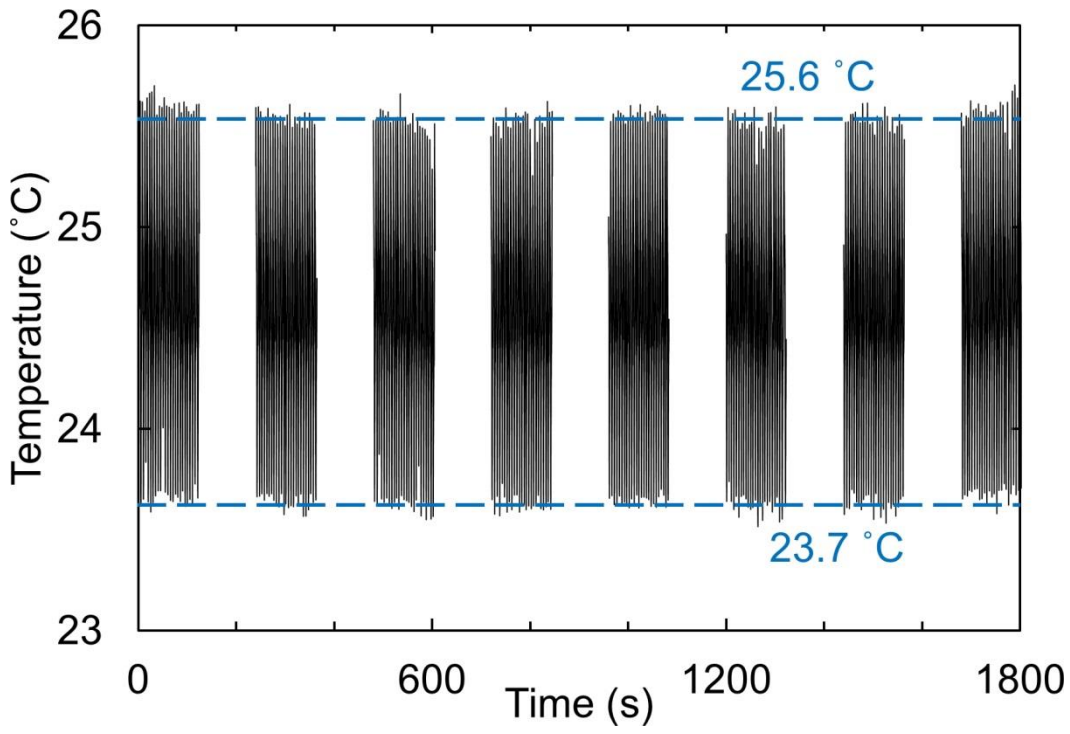

Figure 6.10 Temperature history of a sample for 30 minutes at a stage temperature of 25 °C. The ramp time of the voltage is 0.8 s. The frequency is 0.2 Hz and the electric field amplitude is 54 V/μm. Gaps in the date are due to limitations of the infrascope, the electric field was modulated at all times.

6.4 Summary

In conclusion, the EC effect of a P(VDF-TrFE-CFE) terpolymer was characterized by infrared imaging, which can be conducted conveniently and economically. The heat dissipation of the sample in the air was modeled and used to estimate the adiabatic temperature change at different electric field magnitudes. At an electric field of 90 V/μm, an adiabatic temperature change of 5.2 ˚C is obtained in this work. In an operating frequency range of 0.03 ~ 0.3 Hz, the EC effect was observed to be independent of frequency. The stability of the material was validated by a long time testing. All results suggest that this polymer is a promising material for micro-scale cooling application.

Chapter 7 Summary of thesis work and future research

7.1 Summary of thesis work

The thesis focuses on the development of chip scale refrigeration system. Two different mechanisms are employed and discussed in this work: one is Stirling cooler based on the thermodynamic cycle, the other one is a cooling device using an electrocaloric material. The main conclusions and contributions of this thesis are summarized here.

- Stirling cooler

A new MEMS-based Stirling cooling element was designed. The in-plane design separated the hot and cold chambers by a regenerator, which provides an excellent thermal isolation. A thermodynamic analysis of the system and parametric studies of geometrical parameters demonstrated that the dead volume should be minimized, and the phase lag of the volume variations between the cold side and the hot side should be near 90°. An analytic method by using energy balance was developed and applied to estimate the effects of system non-idealities on the coefficient of performance. Increasing the frequency reduces the *COP* of the system while increases its cooling power density, and the optimal porosity for the *COP* is 0.8~0.9.

The finite element modeling of the new Stirling micro-scale cooler was built and the system performance was evaluated. The computations of multiphysics processes, incorporating compressible fluid flow, heat transfer, porous medium, solid mechanics, and moving mesh, have been successfully implemented. Optimizations of the regenerator indicated that the optimal porosity of the regenerator is near 0.9. Parametric studies of the design demonstrated the effect of the operating frequency on the cooling capacity and the *COP* of the system. When the system

is operated at 600 Hz, the cooling power density is 4.2 W/cm^2 and the system *COP* is 2.93 when the temperatures of the heat sink and heat source are 313.15 K and 288.15 K.

The disadvantages of this Stirling cooler design are mainly from two aspects: the first one is that it is challenging to recover the cold side work and make a high efficiency cooler; the other one that is the electrostatics force is not large enough to compress the gas in the Stirling cooler elements, and some other actuation technologies have to be used to realize the gas compression.

Experimental investigations of the friction factors for gas flow across staggered circular and rough pin fin arrays have been performed in the range of Reynolds number between 1 and 100. The existing conventional correlations predict the friction factor of dense (S_T / d =1.5) and relatively long (H / d = 2.24) pin fin arrays well in the laminar flow region. However, for the sparse and short pin fin array, large deviations between the experimental data and correlation values are observed. A new correlation was proposed to predict the friction factor for the circular pin fin array, including the coupled effect of height-to-diameter ratio ($0.48 < H / d < 2.28$) and pitch-to-diameter ratio ($1.5 < S_T / d < 2.3$). The average MAE of the new correlation is 7.80%. The rough pillar array leads to smaller friction factors than a corresponding circular pillar array, and larger artificial roughness amplitude results in smaller friction factors. The reduction of the friction factor could exceed 50% compared with the circular pillar array when the artificial roughness amplitude to the pillar diameter ratio is 0.2, which demonstrates the potential of this structure in the application of micro-regenerators, micro-reactors or other related MEMS devices for improving the efficiency.

- Electrocaloric cooler

A new chip scale refrigeration system based on EC effect was designed. Finite element simulations with an assumption of sinusoidal diaphragm motions were used to evaluate the

system thermal performance. The effect of the applied electric field was studied. The transit time over which the electric field changes has a small effect on system cooling power, while the time lag between the electric field and the diaphragm motion is found to play an important role. The maximum cooling power density tends to saturate above an operating frequency of 20 Hz and the best *COP* occurs at 10 Hz. A cooling power density of 4.95 W/cm^2 and a *COP* of 3.65 are achieved when the system is operated at a temperature span of 15 K. Multiphysics modeling (joint work with Jinsheng Gao) coupled with Mooney Rivlin hyperplastic model, fluid-solid interaction, heat transfer, porous medium, contact model, electrostatics, and moving mesh technique, is conducted to include the diaphragm deformation and displacement, and validate the results from the thermal modeling.

The EC effect of a P(VDF-TrFE-CFE) terpolymer was characterized by infrared imaging, which can be conducted conveniently and economically. The heat dissipation of the sample in the air was modeled and used to estimate the adiabatic temperature change at different electric field magnitudes. At an electric field of 90 V/μm, an adiabatic temperature change of 5.2 °C was obtained. In an operating frequency range of 0.03 ~ 0.3 Hz, the EC effect was observed to be independent of frequency. The stability of the material was validated by a long time testing. All results suggest that this polymer is a promising material for micro-scale cooling application.

7.2 Future research

- Micro-pump fabrication and characterization

The fluid pump is an essential component for both the Stirling micro cooler and electrocaloric cooler. The fabrication and characterization of the fluid pump are to be accomplished in future. In the design of this thesis, the pump includes a PDMS diaphragm with embedded electrodes and a curve-shaped silicon substrate, and the PDMS membrane is driven

electrostatically. The figures of the PDMS membrane with electrodes and the silicon chamber, which were fabricated by Jinsheng Gao in the ACM group, are shown in Fig. 7.1. After fabrication of the pump, the demonstration of the micro-pump functionality should be verified by the actuation test. The micro-pump performance should be quantified by a series of static and dynamic tests.

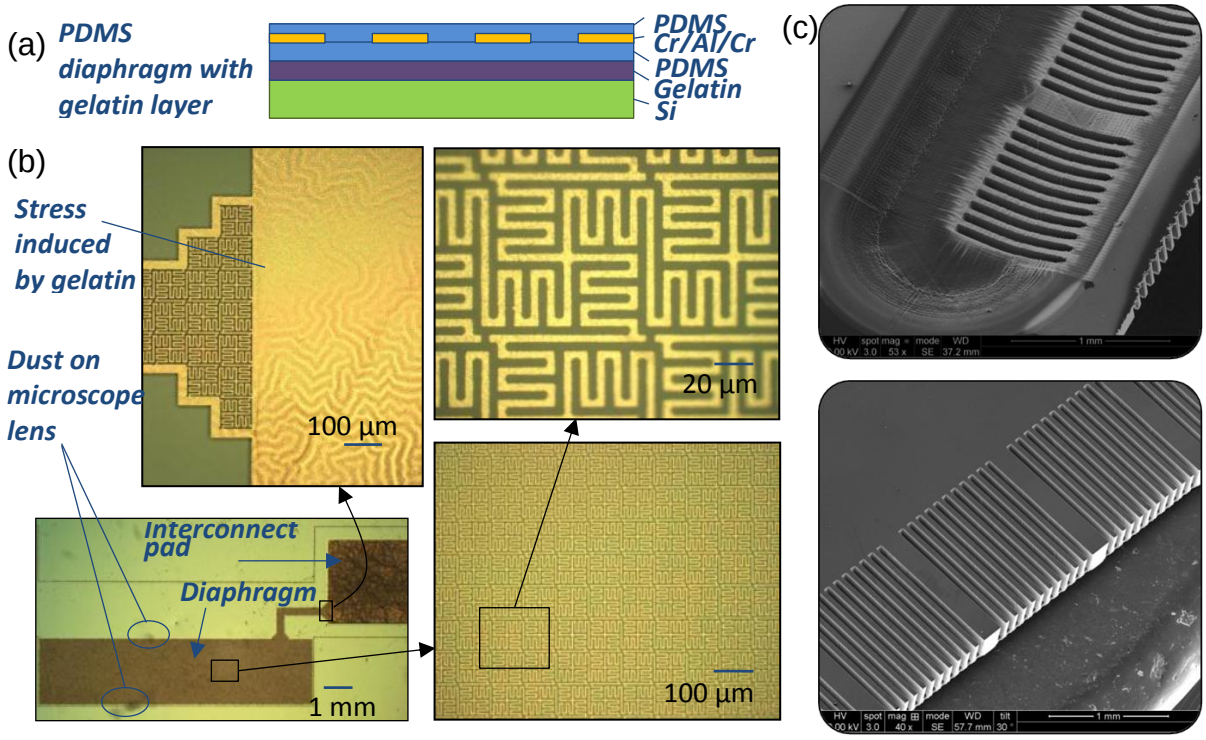

Figure 7.1 (a) Cross section of PDMS diaphragm with embedded electrode fabricated on the gelatin sacrificial layer. (b) Optical microscope photos of the fabricated diaphragm with bonding pad. (c) SEM images of chambers fabricated by grayscale lithography (Courtesy of Jinsheng Gao [103])

- Electrocaloric cooler assembly and testing

The electrostatic fluid pump and the electrocaloric module will be assembled in a 3D printed box, as shown in Fig. 7.2. Dual chambers will be placed face-to-face and PDMS layers are used to seal the device. A preliminary testing will be performed first to characterize the cooler functionality. The test bed is shown in Fig. 7.3. Mechanical pumps are employed to pump

the fluid in the elements back and forth. Then the electrostatic pump will be driven to pump the fluid to measure the cooler performance.

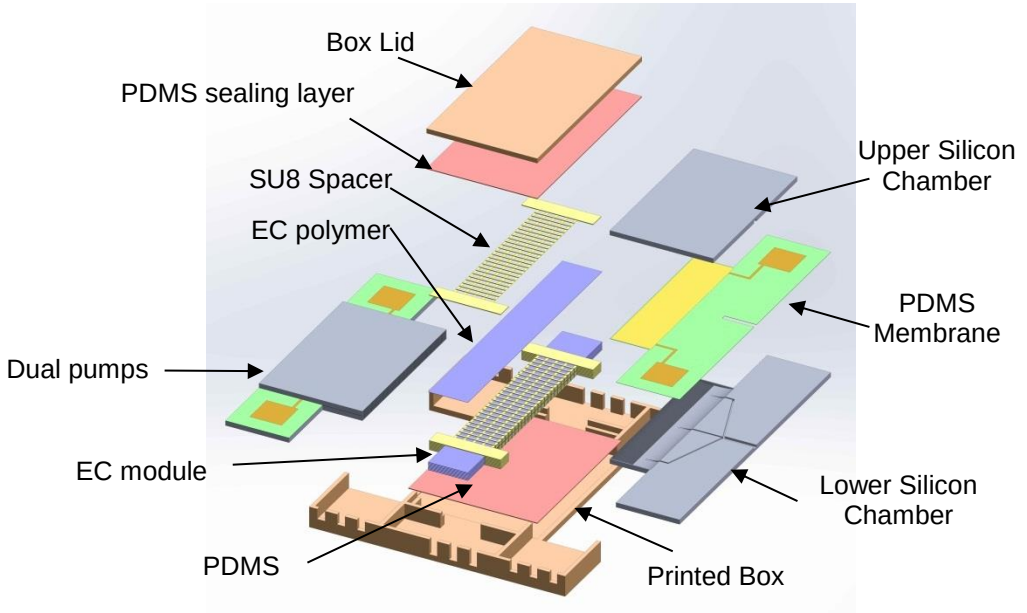

Figure 7.2 Solidworks model for electrocaloric cooler and components for assembly. (Courtesy of Andrew Slippey)

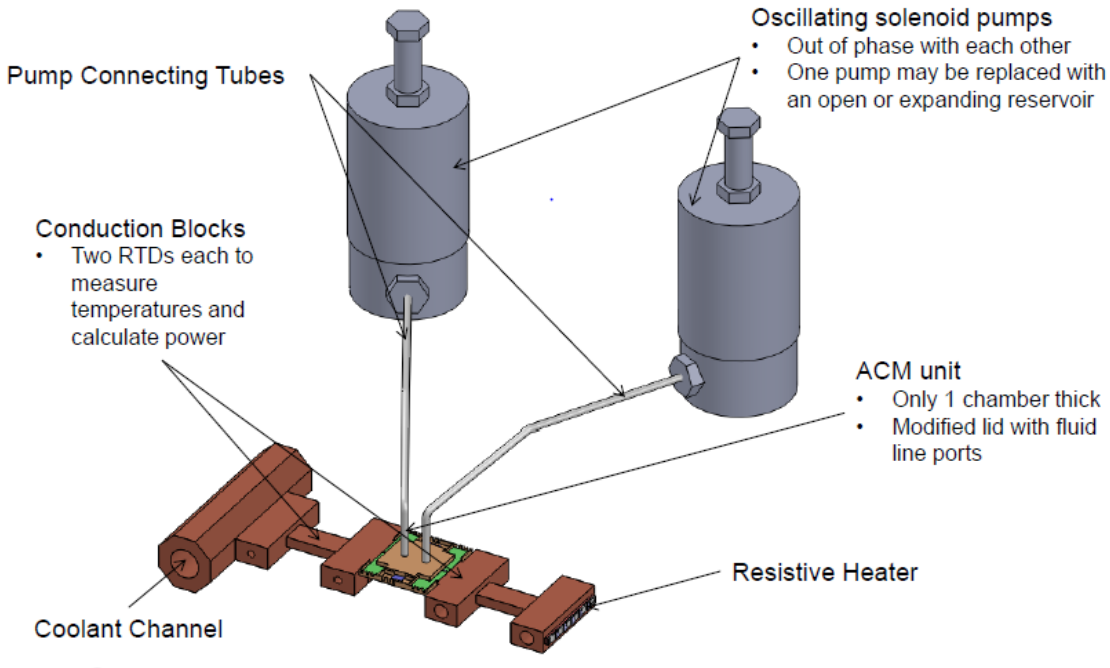

Figure 7.3 Solidworks model of test bed for the electrocaloric cooler. (Courtesy of Andrew Slippey)

Bibliography

[1] J. Burger, "Cryogenic microcooling." *Ph.D. thesis*, 2001, University of Twente, Enschede, The Netherlands.

[2] M. E. Moran, D. M. Wesolek, B. T. Berhane and K. J. Rebello, "Microsystem cooler development", *2nd International Energy Conversion Engineering Conference (IECEC)*, August 16-19, 2004, Providence, RI.

[3] G. Walker, *Stirling cycle machines*, 1976, Clarendon Press, Oxford.

[4] A. Bar-Cohen, J. D. Albrecht and J. J. Maurer, "Near-junction thermal management for wide bandgap devices." *Compound Semiconductor Integrated Circuit Symposium (CSICS), IEEE*, Oct.16-19, 2011, Waikoloa, HI.

[5] J. Sharp, J. Bierschenk and H. B. Lyon, "Overview of solid-state thermoelectric refrigerators and possible applications to on-chip thermal management." *Proc. IEEE* **94**(8) (2006) 1602-1612.

[6] L.W. da Silva and M. Kaviany, "Fabrication and measured performance of a first-generation microthermoelectric cooler." *Journal of Microelectromechanical Systems* **14** (5) (2005) 1110-1117.

[7] R. Venkatasubramanian, E. Siivola, T. Colpitts and B. O'Quinn, "Thin-film thermoelectric devices with high room-temperature figures of merit." *Nature* **413** (2001) 597–602.

[8] C. LaBounty, A. Shakouri and J. E. Bowers, "Design and characterization of thin film microcoolers." *Journal Applied Physics* **89** (7) (2001) 4059–4064.

[9] A. Majumdar, "Thermoelectricity in semiconductor nanostructures." *Science* **303** (5659) (2004) 777-778.

[10] W. Kim, J. Zide, A. Gossard, D. Klenov, S. Stemmer, A. Shakouri and A. Majumdar,

"Thermal conductivity reduction and thermoelectric figure of merit increase by embedding nanoparticles in crystalline semiconductors." *Physical Review Letters* **96** (2006) 045901.

[11] S.L. Garrett, "Reinventing the engine." *Nature*, **339** (1999) 303–305.

[12] P.H. Ceperley, "Gain and efficiency of a short traveling wave heat engine." *Journal of Acoustical Society America* **77** (3) (1985) 1239–1244.

[13] R.S. Reid, W. Ward and G. Swift, "Cyclic thermodynamics with open flow." *Physical Review Letters* **80** (21) (1998) 4617-4620.

[14] T. Jin, G.B. Chen, B.R. Wang and S.Y. Zhang, "Application of thermoacoustic effect to refrigeration." *Review of Scientific Instruments* **74** (1) (2003) 677-679.

[15] O.G. Symko. E. Abdel-Rahman, Y.S. Kwon, M. Emmi and R. Behunin, "Design and development of high-frequency thermoacoustic engines for thermal management in microelectronic." *Microelectronic Journal* **35** (2) (2004) 185-191.

[16] Y. P. Banjare, R.K. Sahoo and S. K. Sarangi, "CFD simulation inertance tube pulse tube refrigerator." in: *19th National and 8th ISHMT-ASME Heat and Mass Transfer Conference*, Paper # EXM-7, 2008.

[17] F. Zink, J. Vipperman and L. Schaefer, "CFD simulation of thermoacoustic cooling." *International Journal of Heat and Mass Transfer* **53** (19) (2010) 3940-3946.

[18] G.W. Swift, "Thermoacoustic engines." *Journal of Acoustical Society America* **84** (4) (1988) 1145-1180.

[19] N.B. Stetson, "Miniature integral Stirling cryocooler." *U.S. Patent* No. 5,056,317, Oct. 15, 1991.

[20] R. Solomon, "Integrated refrigerated computer module." *U.S. Patent* No. 5,349,823, Sep.27, 1991.

[21] FLIR Titanium datasheet, *http://www.goinfrared.com/media/FLIR Titanium Datasheet_I010909PL.pdf*.

[22] L.Bowman, D.M. Berchowitz, and I. Uriell, "Microminiature Stirling cycle cryocoolers and engines." *U.S. Patent* No. 5,457,956, 1995.

[23] M.E. Moran, "Micro-scalable thermal control device." *US Patent* No. 6,385,973 B1, 2002.

[24] M.E. Moran, S. Stelter, and M. Stelter, 2004, "Micro-scale regenerative heat exchanger." *AIAA Canada-Europe-USA-Asia (CANEUS) 2004 Conference on Micro-Nano-Technologies for Aerospace Applications*, Nov. 1-5, 2004, Monterey, CA.

[25] Y.S. Ju, "Solid-state refrigeration based on the electrocaloric effect for electronics cooling." *Journal of Electronic Packaging* **132** (2010) 041004.

[26] M. Valant, "Electrocaloric materials for future solid-state refrigeration technologies." *Progress in Materials Sciences* **57** (6) (2012) 980-1009.

[27] T. Furukawa, "Piezoelectricity and pyroelectricity in polymers." *IEEE Transactions on Electrical Insulation* **24**(3) (1989) 375-394.

[28] P. Kobeco, and I.V. Kurtchatov, "Dielectric properties of rochelle salt crystal." *Z Phys* **66** (1930) 192–205.

[29] A.S. Mischenko, Q. Zhang, J.F. Scott, R.W. Whatmore and N.D. Mathur, "Giant electrocaloric effect in thin-film $PbZr_{0.95}Ti_{0.05}O_3$." *Science* **311** (5765) (2006) 1270-1271.

[30] B. Neese, B. Chu, S.G. Lu, Y. Wang, E. Furman and Q.M. Zhang, "Large electrocaloric effect in ferroelectric polymers near room temperature." *Science* **321** (5890) (2008) 821-823.

[31] Y. Jia and Y.S. Ju, "A solid-state refrigerator based on the electrocaloric effect." *Applied Physics Letters* **100** (2012) 242901.

[32] H. Gu, X. Qian, X. Li, B. Craven, W. Zhu, A. Cheng, S. C. Yao, and Q. M. Zhang, "A chip

scale electrocaloric effect based cooling device." *Applied Physics Letters* **102** (2013) 122904.

[33] H. Gu, B. Craven, X. Qian, X. Li, A. Cheng, and Q. M. Zhang, "Simulation of chip-size electrocaloric refrigerator with high cooling-power density." *Applied Physics Letters* **102** (2013) 112901.

[34] D. Guo, J. Gao, A.J.H. McGaughey, G.K. Fedder, M. Moran and S.C. Yao, "Design and evaluation of a MEMS-based Stirling microcooler." *Journal of Heat Transfer* **135** (2013) 111003.

[35] D. Guo, A.J.H. McGaughey, J. Gao, G.K. Fedder, M. Lee and S.C. Yao, "Multiphysics modeling of a micro-scale Stirling refrigeration system." *International Journal of Thermal Sciences* **74** (2013) 44-52.

[36] D. Guo, J. Gao, Y.J. Yu, S. Santhanam, A. Slippey, G.K. Fedder, A.J.H. McGaughey and S.C. Yao, "Multiphysics modeling of a micro-scale Stirling refrigeration system." *International Journal of Heat and Mass Transfer* **72** (2014) 559-564.

[37] R. Radebaugh, "Pulse tube cryocoolers for cooling infrared sensors." *Proceedings of SPIE, the International Society for Optical Engineering, Infrared Technology and Applications XXVI* **4130** (2000) 363-379.

[38] C.F. Song, Y. Kitamura and S.H. Li, "Evaluation of Stirling cooler system for cryogenic CO_2 capture." *Applied Energy* **98** (2012) 491-501.

[39] N. Pundak, "Stirling cooler." *US Patent* No. 6,397,605, Jun. 4, 2002.

[40] K. Narasaki, S. Tsunematsu, S. Yajima, A. Okabayashi, J. Inatani, K. Kikuchi, R. Satoh, T. Manabe and M. Seta, "Development of cryogenic system for smiles." *AIP Advances in Cryogenic Engeineering: Transactions of the Cryogenic Engineering Conference – CEC* **49** (2004) 1785-1794.

[41] M Kyoya, K. Narasaki, K. Ito, K. Nomi, M. Murakami, H. Okuda, T. Matsumoto and Y. Matsubara, “Development of two-stage small Stirling cycle cooler for temperature below 20 K.” *Cryogenics* **34** (1994) 431-434.

[42] W. R. Martini, “Thermodynamic design of Stirling engines by computer.” *Martini Engineering*, 1980, Richland, Washington.

[43] E. R. Wale and J. I. Smith, Jr., “A mathematical model for steady operation of Stirling-type engines.” *Journal of Engineering for Gas Turbines Power* **90** (1) (1968) 45-50.

[44] K. Lee, I. P. Krepchin and W. M. Toscano, “Thermodynamic description of an adiabatic second order analysis for Stiring engines.” *Proceedings of the 16th IECEC* (1981) 1919-1924.

[45] R. Shoureshi, “Analysis and design of Stirling engines for waste-reat recovery.” 1981, *PhD thesis*, MIT.

[46] R. Radebaugh, "Microscale heat transfer at low temperatures." *Microscale Heat Transfer - Fundamentals and Applications*, 2005, Springer, Berlin.

[47] F. P. Incropera, D. P. DeWitt, T. L. Bergman and A. S. Lavine, *Fundamentals of Heat and Mass Transfer, 6th Edition*, 2006, John Wiley & Sons, New York.

[48] H. Snyman, T.M. Harms and J.M. Strauss, “Design Analysis Methods for Stirling Engines.” *Journal of Energy in Southern Africa* **19** (3) (2008) 4-19.

[49] A. A. Zukauskas, “Heat transfer from tubes in cross flow.” *Advances in Heat Transfer*, 1972, Academic Press, New York.

[50] P.H. Forchheimer, “Wasserbewegun durch boden.” *Zeitschrift des Vereines Deutscher Ingenieure* **45** (1901) 1782-1788.

[51] F.C. Blake, “The resistance of packing to fluid flow.” *AICHE Journal* **14** (1922) 415-422.

[52] S. Ergun, “Fluid flow through packed columns.” *Chemical Engineering Progress* **48** (1952)

89-94.

[53] S. Lee and J. Yang, “Modeling of Darcy-Forchheimer drag for fluid flow across a bank of circular cylinders”, *International Journal of Heat and Mass Transfer* **40** (13) (1997) 3149-3155.

[54] D. Guo, A.J.H. McGaughey, G.K. Fedder, M. Lee and S.C. Yao, “Modeling system dynamics in a MEMS-based Stirling cooler.” *COMSOL Conference*, 2011, Boston, MA.

[55] M. Tanaka, I. Yamashita and F. Chisaka, “Flow and heaq transfer characteristics of the Stirling engine regenerator in an oscillating flow.” *Journal of the Japan Society of Mechanical Engineers* **33** (2) (1990) 283-289.

[56] K. Kadoya, N. Matsunaga and A. Nagashima, “Viscosity and thermal conductivity of dry air in the gaseous phase.” *Journal of Phyical and Cheical Reference Data* **14** (4) (1985) 947-970.

[57] R.C. Tew, T. Simon, D. Gedeon, M. Ibrahim and W. Rong, “An initial non-equilibrium porous media model for CFD simulation of Stirling regenerators.” in: *4th International Energy Conversion and Engineering Conference*, 2006, San Diego, CA.

[58] A. Amiri and K. Vafai, “Transient analysis of incompressible flow through a packed bed.” *International Journal of Heat and Mass Transfer* **41**(24) (1998) 4259–4279.

[59] S. Whitaker, “Forced convection heat-transfer correlations for flow in pipes, past flat plates, single cylinders, single spheres, and for flow in packed-beds and tube bundles.” *AIChE Journal* **18** (2) (1972) 361–371.

[60] T. H. Hwang and S.C.Yao, “Crossflow heat transfer in tube bundles at low Reynolds numbers.” *Journal of Heat Transfer* **108** (3) (1986) 697–700.

[61] C. W. Hirt, A. A. Amsden and J. L. Cook, “An arbitrary Lagrangian-Eulerian computing method for all flow speeds.” *Journal of Computational Physics* **14** (1974) 227–253.

[62] P. R. Amestoy, I. S. Duff and J.-Y. L'Excellent, “Multifrontal parallel distributed

symmetric and unsymmetric solvers." *Computer Methods in Applied Mechanics and Engineering* **184** (2000) 501-520.

[63] Y. Peles, A. Kosar, C. Mishra, C.J. Kuo and B. Schneider, "Forced convective heat transfer across a pin fin micro heat sink." *International Journal of Heat and Mass Transfer* **48** (2005) 3615-3627.

[64] M.W. Losey, J. Jackman, S.L. Firebaugh, M.A. Schmidt and K. Jensen, "Design and fabrication of microfluidic devices for multiphase mixing and reaction." *Journal of Microelectromechanical Systems* **11** (2002) 709-717.

[65] L. A. Christel, K. Petersen, W. McMillan and M. A. Northrup, Rapid, automated nucleic acid probe assays using silicon microstructures for nucleic acid concentration." *Journal of Biomechanical Engineering* **121** (1999) 22-27.

[66] T. H. Chilton and R. P. Generaux, "Pressure drop across tube banks." *Transactions of American Institute Chemical Engineers* **29** (1933) 161-173.

[67] E. S. Gaddis and V. Gnielski, "Pressure drop in horizontal cross flow across tube bundles." *International Chemical Engineering* **25** (1985) 1-15.

[68] W. P. Damerow, J. C. Murtaugh and F. Burgraf, "Experimental and analytical investigation of the coolant flow characteristics in cooled turbine airfoils." *NASA*, 1972, CR-120883.

[69] K. A. Moores and Y. K. Joshi, "Effect of tip clearance on the thermal and hydrodynamic performance of a shrouded pin fin array." *Journal of Heat Transfer* **125** (2003) 999-1006.

[70] B. E. Short, P. E. Raad and D. C. Price, "Performance of pin fin cast aluminum coldwalls, part. 1: friction factor correlations." *Journal of Thermophysics and Heat Transfer* **16** (2002) 389-396.

[71] S. Vanapalli, H. J. M. Brake, H. V. Jansen, J. F. Burger, H. J. Holland, T. T. Veenstra and

M. C. Elwenspoek, “Pressure drop of laminar gas flows in a microchannel containing various pillar matrices.” *Journal of Microelectromechanical Systems* **17** (2007) 1381-1386.

[72] S. C. Lau, Y. S. Kim and J. C. Han, “Effects of fin configuration and entrance length on Local endwall heat/mass transfer in a pin fin channel.” *ASME*, 1995, Paper No.81-WA/HT-6.

[73] A. Kosar, C. Mishra and Y. Peles, “Laminar flow across a bank of low aspect ratio micro pin fins.” *Journal of Fluids Engineering* **127** (2005) 419-430.

[74] A. Kosar, B. Schneider and Y. Peles, “Hydrodynamic characteristics of crossflow over MEMS-based pillars.” *Journal of Fluids Engineering* **133** (2011) 081201.

[75] G.B. Zhou and S.C. Yao, “Effect of surface roughness on the pressure drop of liquid flow in micro-channels.” *Applied Thermal Engineering* **31** (2010) 228-234.

[76] D. Glossa and H. Herwiga, “Microchannel roughness effects: a close-up view.” *Heat Transfer Engineering* **30** (2009) 62-69.

[77] H.Y. Wu and P. Cheng, “An experimental study of convective heat transfer in silicon microchannels with different surface conditions.” *International Journal of Heat and Mass Transfer* **46** (2003) 2547-2556.

[78] G. Croce, P. D’agaro and C. Nonino, “Three-dimensional roughness effect on microchannel heat transfer and pressure drop.” *International Journal of Heat and Mass Transfer* **50** (2007) 5249-5259.

[79] A.S. Rawool, S.K. Mitra and S.G. Kandlikar, “Numerical simulation of flow through microchannels with designed roughness.” *Microfluidics and Nanofluidics* **2** (2006) 215–221.

[80] J. Gao, D. Guo, A.J.H. McGaughey, S. Santhanam, S.C. Yao, M. Moran, W. Anderson, D. Wolf and G. K. Fedder, “Stirling microcooler array with elemental in-plane flow.” *37th GOMACTech Conference*, 2012, Las Vegas.

[81] A.A. Zukauskas and R.V. Ulinskas, "Heat transfer from tubes in cross flow." *Advances in Heat Transfer* **8** (1989) 72–160.

[82] E. M. Sparrow and V. B. Grannis, "Pressure drop characteristics of heat exchangers consisting of arrays of diamond-shaped pin fins." *International Journal of Heat and Mass Transfer* **34** (1991) 589–600.

[83] T. Tsukamoto, M. Esashi and S. Tanaka, "Magnetocaloric cooling of a thermally-isolated microstructure." *Journal of Micromechanics and Microengineering* **22** (9) (2012) 094008.

[84] B. A. Tuttle and D. A. Payne, "The effects of microstructure on the electrocaloric properties of $Pb(Zr,Sn,Ti)O_3$ ceramics." *Ferroelectrics* **37** (1) (1981) 603-606.

[85] X. Li, X.S. Qian, S.G. Lu, J. Cheng, Z. Fang and Q.M. Zhang, "Tunable temperature dependence of electrocaloric effect in ferroelectric relaxor poly(vinylidene fluoride-trifluoroethylene - chlorofluoroethylene) terpolymer." *Applied Physics Letters* **99** (2011) 052907.

[86] G.G. Wiseman and J.K. Kuebler, "Electrocaloric effect in ferroelectric rochelle salt." *Physical Review* **131** (5) (1963) 2023-2027.

[87] W.N. Lawless and A.J. Morrow, "Specific heat and electrocaloric properties of a $SrTiO_3$ ceramic at low temperatures." *Ferroelectrics* **15** (1) (1977) 159-165.

[88] S. G. Lu, B. Rožic, Q. M. Zhang, Z. Kutnjak, X. Li, E. Furman, L. J. Gorny, M. R. Lin, B. Malic, M. Kosec, R. Blinc and R. Pirc, "Organic and inorganic relaxor ferroelectrics with giant electrocaloric effect." *Applied Physics Letters* **97** (2010) 162904.

[89] *http://www.ulet.co.kr/product/Vacuum%20Fluids/heat/galden.htm*.

[90] G. Sebald, L. Seveyrat, J.F. Capsal, P.J. Cottinet and D. Guyomar, "Differential scanning calorimeter and infrared imaging for electrocaloric characterization of poly(vinylidene fluoride-trifluoroethylenechlorofluoroethylene) terpolymer." *Applied Physics Letters* **101** (2012) 022907.

[91] S.G. Lu, Q. M. Zhang, "Electrocaloric materials for solid-state refrigeration." *Advanced Materials* **21** (2009) 1-5.

[92] B. Chu, "PVDF - based copolymers, terpolymers and their multi-component material systems for capacitor applications." *PhD thesis*, 2008, Pennsylvania State University.

[93] Q. Chen, B. Chu, X. Zhou, Q. M. Zhang, "Effect of metal-polymer interface on the breakdown electric field of poly(vinylidene fluoride – trifluoroethylene - chlorofluoroethylene) terpolymer." *Applied Physics Letters* **91** (2007) 062907.

[94] R.W. Ogden, *Non-Linear Elastic Deformations*, 1984, ISBN 0-486-69648-0, Dover.

[95] M. Mooney, "A theory of large elastic deformation." *Journal of Applied Physics* **11** (9) (1940) 582-592

[96] R. S. Rivlin, "Large elastic deformations of isotropic materials. IV. Further developments of the general theory, *Philosophical Transactions of the Royal Society of London. Series A, Mathematical and Physical Sciences* **241**(835) (1948) 379-397.

[97] S.H. Yoon, V. Reyes-Ortiz, K.H. Kim, Y.H. Seo and M.R.K. Mofrad, "Analysis of circular PDMS microballoons with ultralarge deflection for MEMS design", *Journal of Microelectromechanical Systems* **19** (4) (2010) 854-864.

[98] Y. S. Yu and Y. P. Zhao, "Deformation of PDMS membrane and microcantilever by a water droplet: Comparison between Mooney–Rivlin and linear elastic constitutive models", *Journal of Colloid and Interface Science* **332** (2009) 467–476.

[99] D. P. J. Cotton, A. Popel, I. M. Graz and S. P. Lacour, "Photopatterning the mechanical properties of polydimethylsiloxane films." *Journal of Applied Physics* **109** (2011) 054905.

[100] G. Sebald, L. Seveyrat, D. Guyomar, L. Lebrun, B. Guiffard and S. Pruvost, "Electrocaloric and pyroelectric properties of $0.75Pb(Mg_{1/3}Nb_{2/3})O_3$-$0.25PbTiO_3$ single crystals."

Journal of Applied Physics **100** (12) (2006) 124112.

[101] Y. Bai, G. Zheng and S. Shi, "Direct measurement of giant electrocaloric effect in $BaTiO_3$ multilayer thick film structure beyond theoretical prediction." *Applied Physics Letters* **96** (2010) 192902.

[102] Y. Jia and Y. S. Ju, "Direct characterization of the electrocaloric effects in thin films supported on substrates." *Applied Physics Letters* **103** (2013) 042903.

[103] J. Gao, D. Guo, S. Santhanam, Y. J. Yu, A. McGaughey, S. C. Yao and G. K. Fedder, "Release and transfer of large-area ultra-thin PDMS." *MEMS 2014 Conference*, Jan. 26-30, 2014, San Francisco, CA.

Appendices

Appendix A

Publication list

Journal papers:

[1] **D. Guo**, J. Gao, Y.J. Yu, S. Santhanam, A. Slippey, G. K. Fedder, A. J. H. McGaughey and S. C. Yao, "Design and modeling of a fluid-based micro-scale electrocaloric refrigeration system." *International Journal of Heat and Mass Transfer* **72** (2014) 559-564.

[2] **D. Guo***, J. Gao*, Y.J. Yu, S. Santhanam, A. J. H. McGaughey, G. K. Fedder, and S. C. Yao, "Electrocaloric measurement of poly(vinylidene fluoride-trifluoroethylene-chlorofluoroethylene) terpolymer by infrared imaging." *Applied Physics Letters* **105** (3) (2014) 031906. (*Equal contribution)

[3] **D. Guo**, J. Gao, S. Santhanam, and S. C. Yao, "Experimental investigation of laminar flow across short micro pin fin arrays." *Journal of Micromechanics and Microengineering* **24** (2014) 095011.

[4] **D. Guo**, A. J. H. McGaughey, J. Gao, G. K. Fedder, M. Lee and S. C. Yao, "Multiphysics modeling of a micro-scale Stirling refrigeration system." *International Journal of Thermal Sciences* **74** (2013) 44-52.

[5] **D. Guo**, J. Gao, A. J. H. McGaughey, G. K. Fedder, M. Moran and S. C. Yao, "Design and evaluation of a MEMS-based Stirling microcooler." *Journal of Heat Transfer* **135** (11) (2013) 111003.

[6] Y. Li, **D. Guo** and S.C. Yao, "Thermal-aware Micro-channel Cooling of Multicore Processors: A Three-stage Design Approach." *Journal of Electronic Packaging* **136** (2) (2014) 021002.

Conference papers:

[1] J. Gao, **D. Guo**, S. Santhanam, Y. J. Yu, A. McGaughey, S. C. Yao and G. K. Fedder, "Release and transfer of large-area ultra-thin PDMS." *MEMS Conference*, Jan. 26-30, 2014, San Francisco, CA.

[2] **D. Guo**, J. Gao, Y.J. Yu, S. Santhanam, G. K. Fedder, A. J. H. McGaughey, and S. C. Yao, "Design of a fluid-based micro-scale electrocaloric refrigeration system." *ASME HT 2013*, July 14-19, 2013, Minneapolis, MN, HT2013-17396.

[3] **D. Guo**, A. J. H. McGaughey, J. Gao, G. K. Fedder, M. Lee and S. C. Yao, "Numerical modeling of a micro-scale Stirling cooler." *ASME HT 2012*, July 8-12, 2012, Puerto Rico, HT2012-58361.

[4] J. Gao, **D. Guo**, A. J. H. McGaughey, S. Santhanam, S. C. Yao, M. Moran, W. Anderson, D. Wolf and G. K. Fedder, "Stirling microcooler array with elemental in-plane flow." *GOMACTech Conference 2012*, March 19-22, 2012, Las Vegas, NV.

[5] **D. Guo**, J. Gao, A. J. H. McGaughey, M. Moran, S. Santhanam, G. K. Fedder, W. Anderson and S. C. Yao, "Design and evaluation of a MEMS-based Stirling cycle micro-refrigeration system." *ASME 2011 IMECE*, November 11-17, 2011, Denver, Colorado, IMECE2011-63084.

[6] **D. Guo**, A.J.H. McGaughey, G. K. Fedder, M. Lee and S. C. Yao, "Modeling system dynamics in a MEMS-based Stirling cooler." *COMSOL Conference 2011*, October, 2011, Boston, MA.

Appendix B

Fabrication process of silicon pillars

- *Wafer cleaning*

  Acetone, isopropyl alcohol are used to clean the wafer first, then rinse it by DI water.

- *Spin coat photoresist*

  Photoresist AZ 4210, thickness 2.1μm.

  Spin HMDS twice first:

  Spread 6 s @ 600 rpm, then spin 30 s @ 3000 rpm

  Spin AZ 4210:

  Spread 8 s @ 600 rpm, then spin 30 s @ 4000 rpm

  After spinning, use cotton tip to clean the photoresist left on edge of the wafer.

- *Softbake*

  Bake for 1 mins @ 95 °C

- *Expose by Karl Suss MA6 contact aligner at Contact Mode (5 mW/cm^2)*

  Exposure time 150 s.

- *Develop*

  AZ 400K developer (1:4), time 2 mins

  After developing, rinse in DI water, then put sample in Spin Rinse/Dryer

- *1 min oxygen plasma to clean @ 100 W.*

- *DRIE for 50 μm depth etching.*

  Process time: 22 mins (66 cycles)

  Recipe: stdaniso

  Etch:

  SF6 flow 130 sccm, O2 flow 13 sccm

  Cycle time: 12 s, Coil power 600 W

  Passivation:

  C4F8 flow 85 sccm, Cycle time 8 s, Coil power 600 W

- *After DRIE, remove residual photoresist by acetone.*

Appendix C

Equipment for pressure measurements

Mass flow-meters and controller FMA-A2403, Omega Engineering

Differential pressure transducer MMDDU001V10K2A0T1A1CE, Omega Engineering

Appendix D

Infrascope system calibration

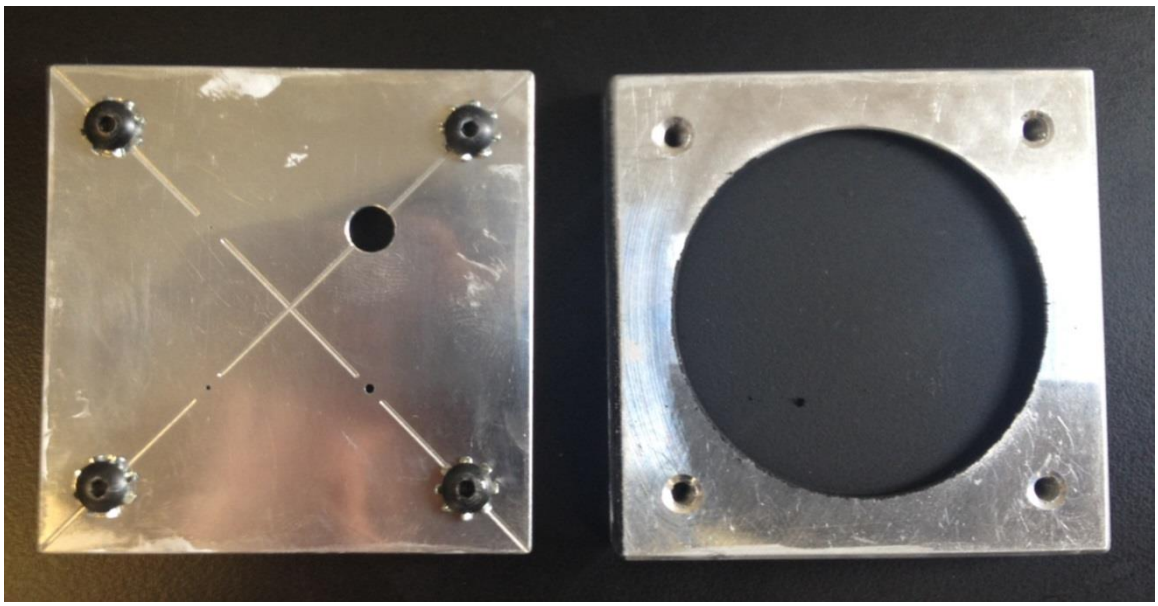

Radiance calibration target Uniformity calibration target

- *Radiance calibration*
  - High temperature ranges of 3 and 4 should not be calibrated. A high temperature source is needed for calibration.
  - Before calibration, back up the old calibrations files. "C:\Program files\QFI\Thermal Map\Parms"
  - Use radiance calibration target for calibration and a thin layer of thermal grease should be placed to achieve a good thermal contact between the thermal stage and the target.
  - Use the hole for calibration and focus on the edge of the hole.

- From the software menu, choose “Calibrate System Radiance -Single Lens / Range” for one lens calibration. Then press “Start” to begin the calibration process.

- *Uniformity calibration*
  - Use uniformity calibration target for calibration and a thin layer of thermal grease should be placed to achieve a good thermal contact between the thermal stage and the target.
  - Focus on the black surface of the target with the help of a thin object placed on top of target. Choose a perfectly uniform area for calibration.
  - From the software menu, choose “Calibrate System uniformity” for one lens calibration. Use the default values for the calibration. Then press “Start” to begin the calibration process.

Appendix E

LabVIEW program for data collection

- *Keithley 2400*

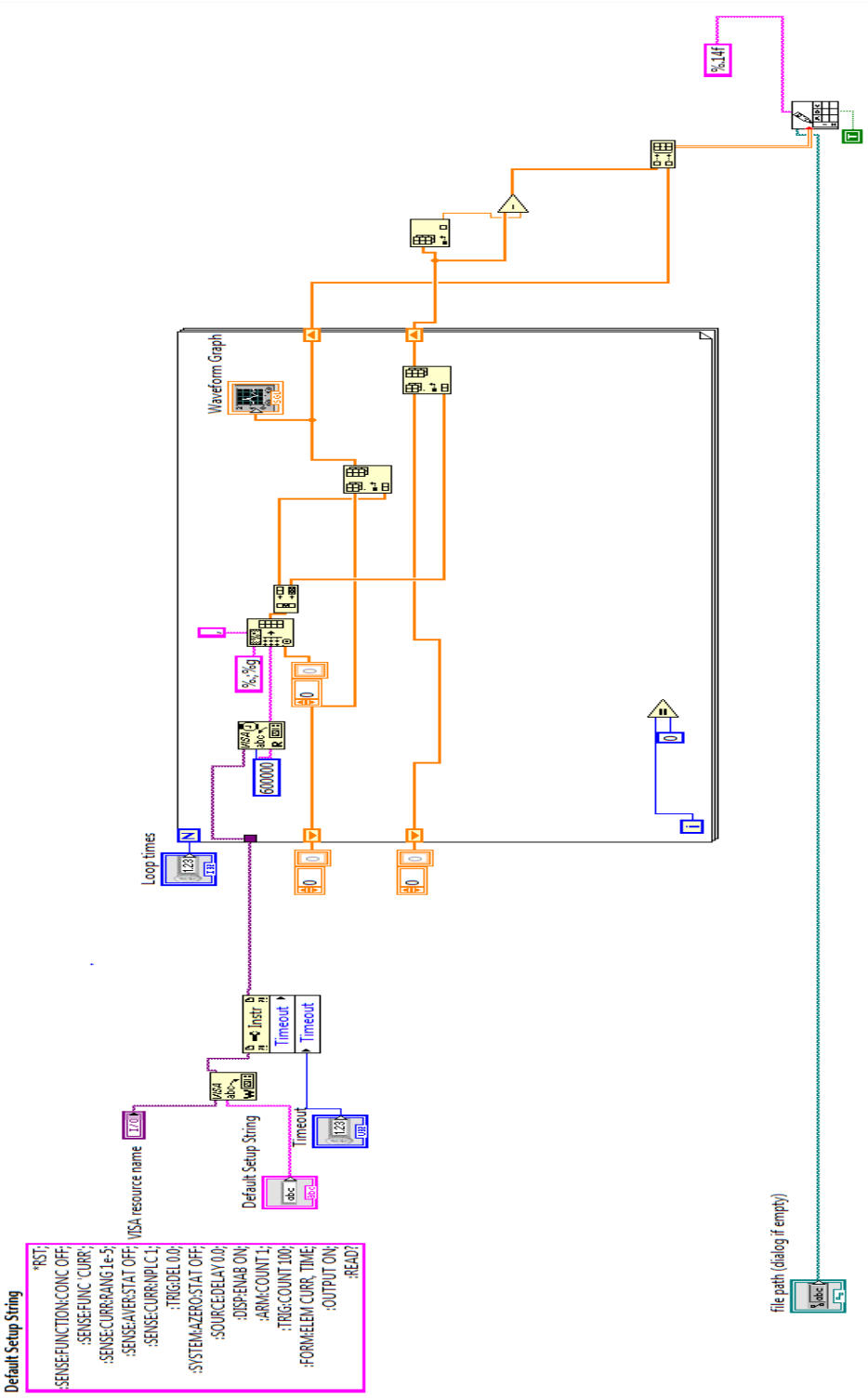

- *Agilent 34401*

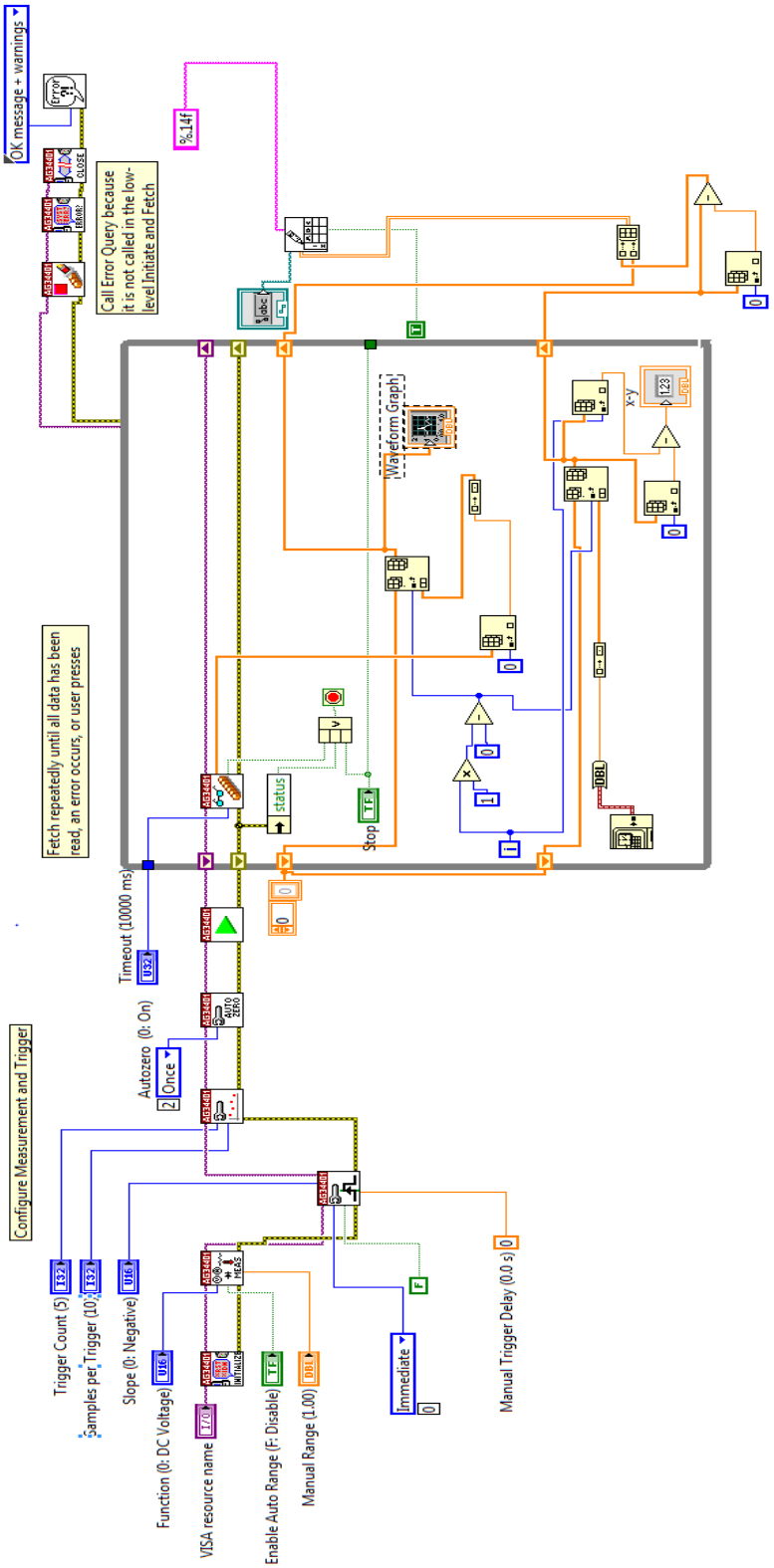

Appendix F

Setting of modeling of Stirling cooler by COMSOL 4.2

- *Parameters*

L	2250[um]	0.0022500 m
H	150[um]	1.5000E-4 m
h1	10[um]	1.0000E-5 m
h2	20[um]	2.0000E-5 m
h3	H-h1-h2	1.2000E-4 m
Lr	500[um]	5.0000E-4 m
R	h3/2+L*L/8/h3	0.0053334 m
M_air	29[g/mol]	0.029000 kg/mol
f	100[Hz]	100.00 Hz
thick	50[um]	5.0000E-5 m
A_wet	(pi*20*8.5/500/5	21363 1/m
LL	2250[um]	0.0022500 m
k_si	163[W/m/K]	163.00 W/(m·K)
HHH	1e30[W/K/m^3]	1.0000E30 W/(m³·K)

- *Variables*

Den_air	ht.pA*M_air/T/R_const
Max_zdisc	h3-R+sqrt(R^2-(x-LL/2)^2-(y-L/2)^2)
Max_zdish	h3-R+sqrt(R^2-(x-LL/2-Lr-LL)^2-(y-L/2)^2)
Zdisc	-Max_zdisc*sin(2*pi*f*t)
Zdish	-Max_zdish*sin(2*pi*f*t-pi/2)*(t>=1/4/f)
Q_visc	fp.mu*((2*d(ht.ux,x)-2*(d(ht.ux,x)+d(ht.uy,y)+d(ht.uz,z))/3)*d(ht.ux,x)+(d(ht.ux,y)+d(ht.uy,x))*d(ht.ux,y)+(d(ht.ux,z)+
Q_pressure	(d(ht.pA,TIME)-d(ht.pA,x)*d(x,TIME)-d(ht.pA,y)*d(y,TIME)-d(ht.pA,z)*d(z,TIME)+ht.ux*d(ht.pA,x)+ht.uy*d(ht.pA,y)+ht.uz
Re_d	abs(Den_air*(abs(u)+1e-30)*20[um]/fp.mu)
Nu_d	2.096*Re_d^0.1135
hfs	abs(Nu_d*ht.kxx/20[um])

- *Geometry*

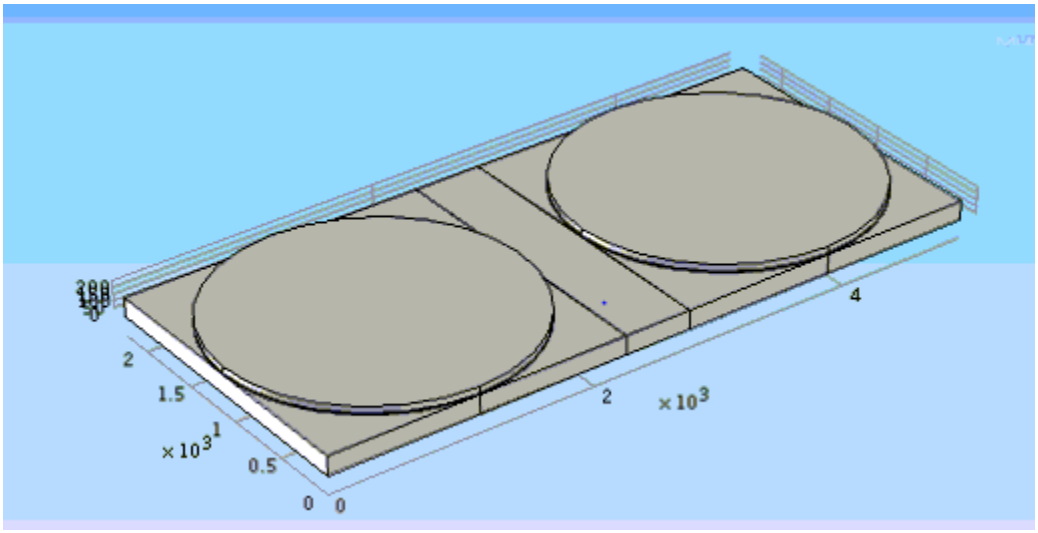

- *Physics*

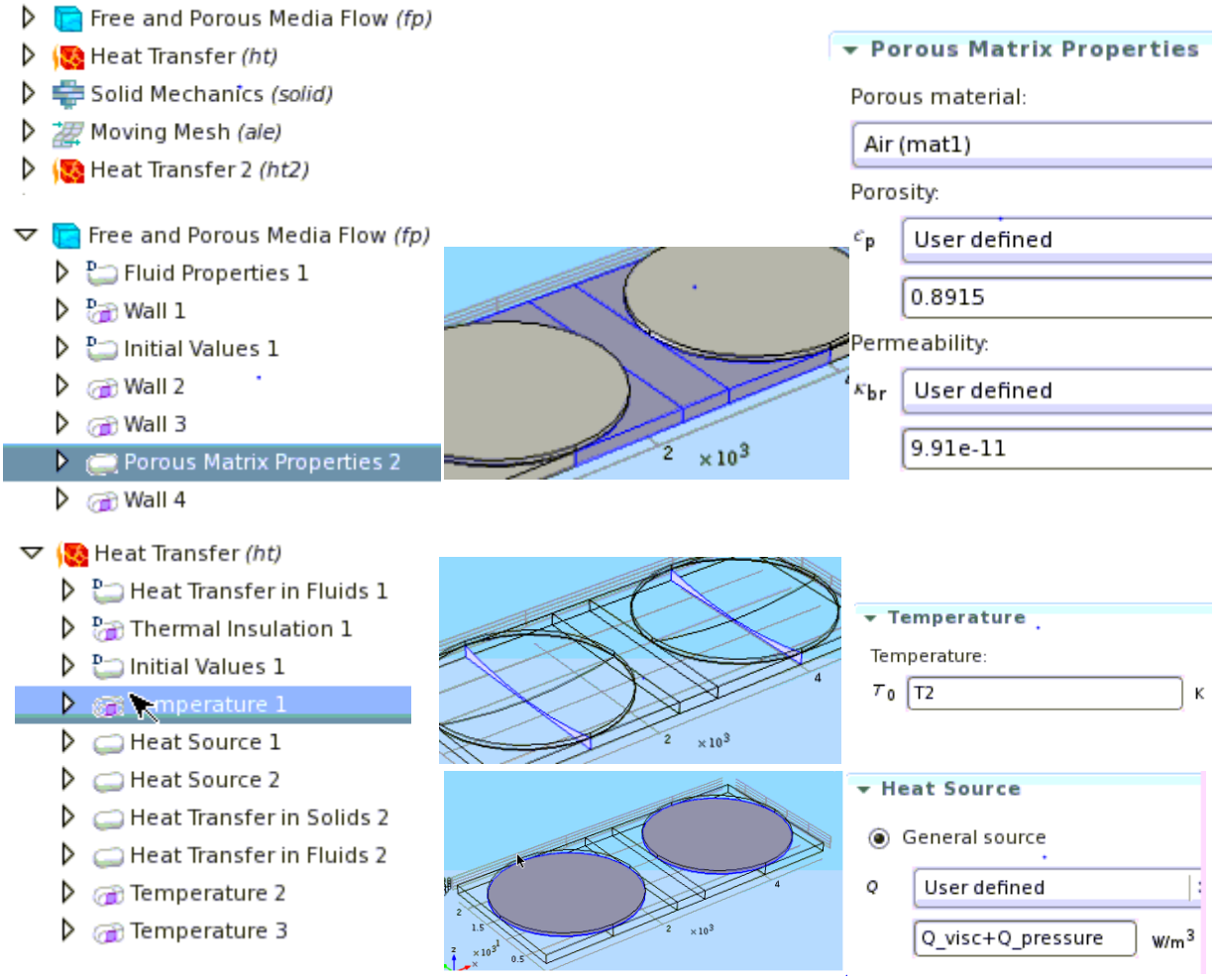

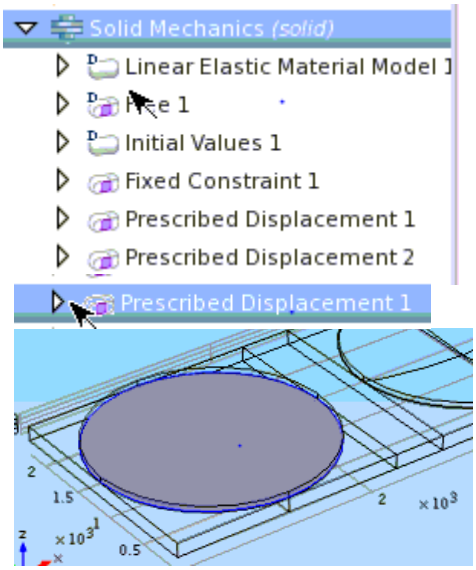
Solid Mechanics (solid)
Linear Elastic Material Model 1
Initial Values 1
Fixed Constraint 1
Prescribed Displacement 1
Prescribed Displacement 2
Prescribed Displacement 1

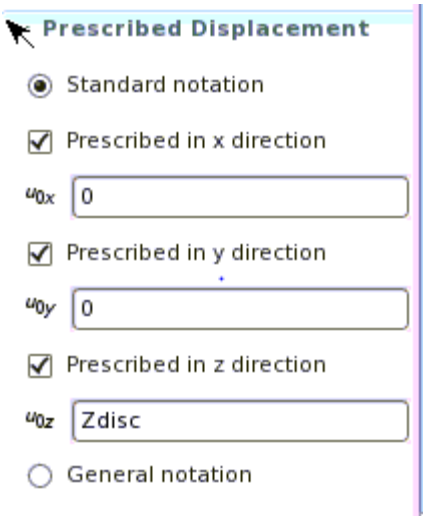
Prescribed Displacement
Standard notation
Prescribed in x direction
u0x
0
Prescribed in y direction
u0y
0
Prescribed in z direction
u0z
Zdisc
General notation

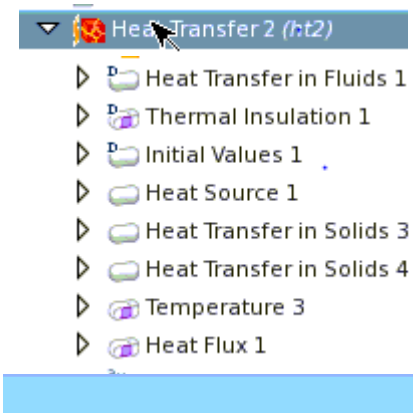
Heat Transfer 2 (ht2)
Heat Transfer in Fluids 1
Thermal Insulation 1
Initial Values 1
Heat Source 1
Heat Transfer in Solids 3
Heat Transfer in Solids 4
Temperature 3
Heat Flux 1

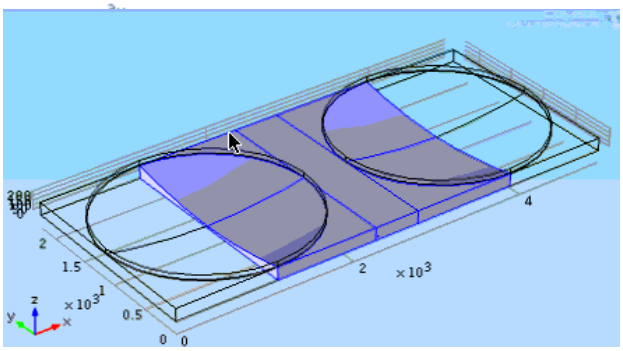

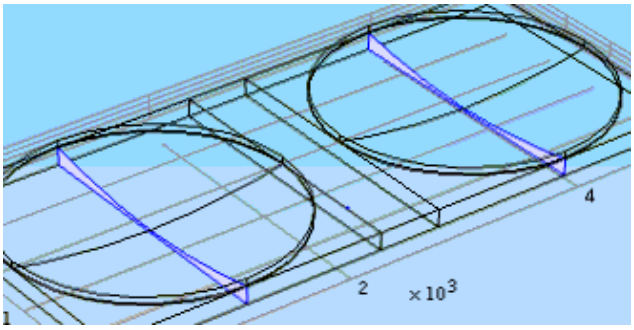

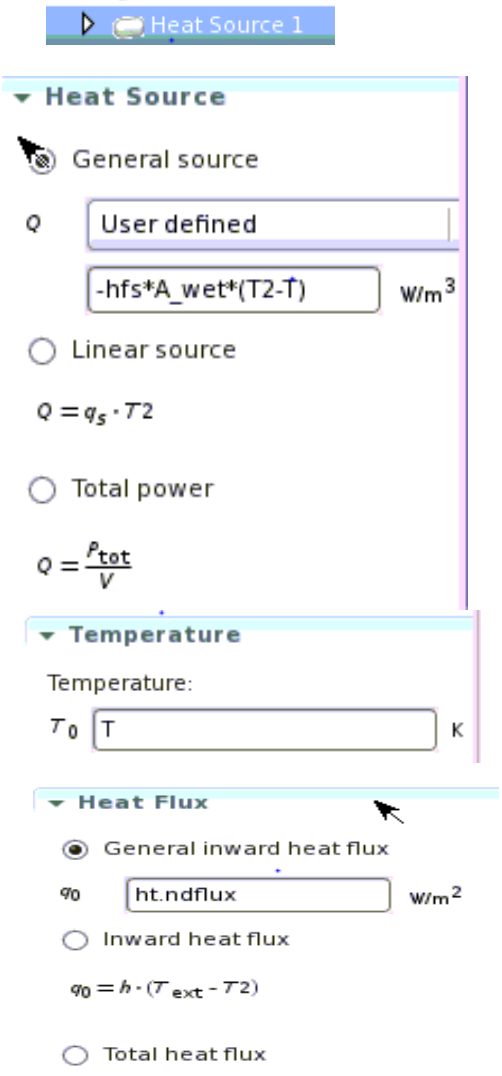
Heat Source 1
Heat Source
General source
Q
User defined
-hfs*A_wet*(T2-T)
W/m3
Linear source
Q = qs · T2
Total power
Q = Ptot / V
Temperature
Temperature:
T0
T
K
Heat Flux
General inward heat flux
q0
ht.ndflux
W/m2
Inward heat flux
q0 = h · (Text - T2)
Total heat flux

Appendix G

Setting of multiphysics modeling of electrocaloric cooler by COMSOL 4.3 b

- *Parameters*

f	5[Hz]	5.0000 Hz	M_H_g	15	15.000
Vin0	85[V]	85.000 V	M_L	50	50.000
cfc	5e10[Pa/m]	5.0000E10 N/n	M_H_i	2	2.0000
H	280[um]	2.8000E-4 m	M_H_d	4	4.0000
H_c	10[um]	1.0000E-5 m	M_L_r	40	40.000
H_ch	150[um]	1.5000E-4 m	M_H_r	10	10.000
H_g	2[um]	2.0000E-6 m	M_ch_e	12	12.000
H_b	H-H_ch	1.3000E-4 m	C1	321[kPa]	3.2100E5 Pa
L_ec	2500[um]	0.0025000 m	C2	0[kPa]	0 Pa
L	2000[um]	0.0020000 m	L_d	L/2	0.0010000 m
LL	2500[um]	0.0025000 m	L_ch_e	(LL-L)/2	2.5000E-4 m
H_d	13[um]	1.3000E-5 m	den_70	1680[kg/m^3]	1680.0 kg/m³
n_ec	6	6.0000			
H_i	2[um]	2.0000E-6 m			

vis_70	0.00084[Pa*s]	8.4000E-4 Pa·s
por_70	0.66666	0.66666
per_70	3.5e-11[m^2]	3.5000E-11 m²
t_ec	20[um]	2.0000E-5 m
h_ch	50[um]	5.0000E-5 m
k_70	0.065[W/m/K]	0.065000 W/(m
cp_70	970[J/kg/K]	970.00 J/(kg·K)
E0	100[MV/m]	1.0000E8 V/m
den_ec	1800[kg/m^3]	1800.0 kg/m³
epss	0.5	0.50000
h_fs	NU*k_70/w_ch	5349.5 W/(m²·K
A_wet	1/2/w_ch	10000 1/m
w_ch	50[um]	5.0000E-5 m
k_si	163[W/m/K]	163.00 W/(m·K)

- *Variables*

gap1	H_ch*(3*((x-L_ch_e)/L_d)^2-2*((x-L_ch_e)/L_d)^3)+v_solid
gap2	H_ch*(1-3*((x-LL/2)/L_d)^2+2*((x-LL/2)/L_d)^3)+v_solid
gap3	H_ch*(3*((x-L_ch_e-LL-L_ec)/L_d)^2-2*((x-L_ch_e-LL-L_ec)/L_d)^3)+v_solid
gap4	H_ch*(1-3*((x-LL/2-LL-L_ec)/L_d)^2+2*((x-LL/2-LL-L_ec)/L_d)^3)+v_solid
Vin1e	2*Vin0+1[V]
Vin2e	1[V]
Fc1	(gap1<0)*(-cfc)*gap1
Fc2	(gap2<0)*(-cfc)*gap2
Fc3	(gap3<0)*(-cfc)*gap3
Fc4	(gap4<0)*(-cfc)*gap4
Vin1d	Vin0*wv1(t)+Vin0+1[v]
Vin2	(t<0.2/f)*1[V]+(t>=0.2/f)*(Vin0*wv2(t)+Vin0+1[V])
Vin1c	(t<0.3/f)*(Vin0*wv1(t)+Vin0+1[v])+(t>=0.3/f)*(2*Vin0+1[V])
Vin1	(t<0.2/f)*(2*Vin0*wv1(t)+1[V])+(t>=0.2/f)*(Vin0*wv1(t)+Vin0+1[v])
dsde	-(6.85e-8)-2*(2.71e-15)*V_ec
V_ec	E0*(wv1(t+0.5/f)+1)/2

- *Geometry & Materials*

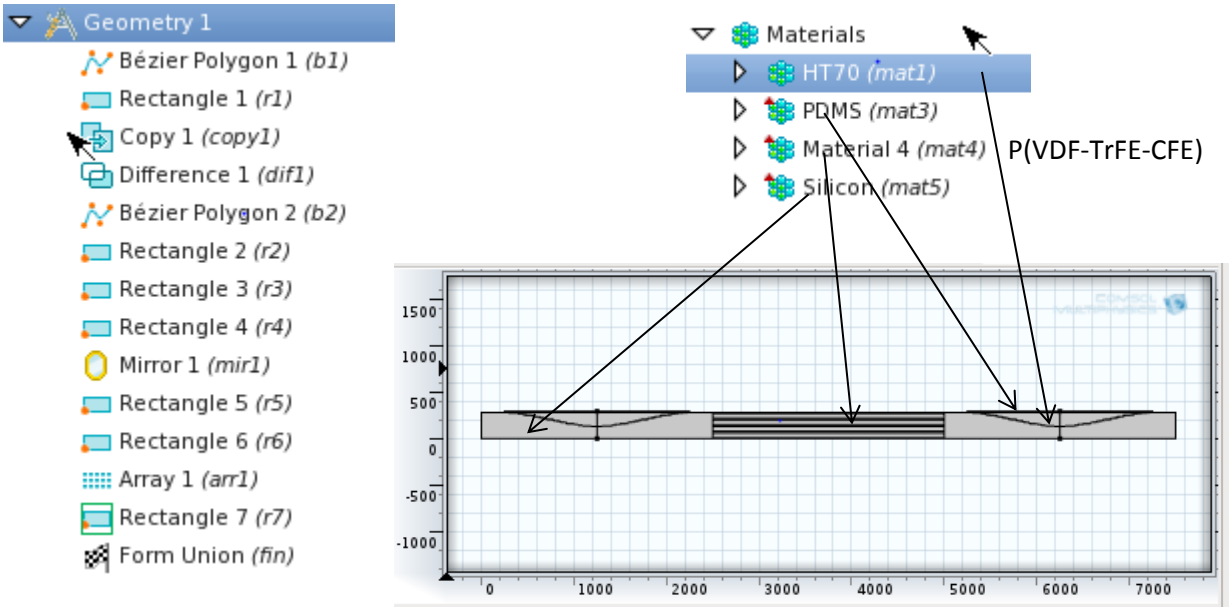

- *Physics*

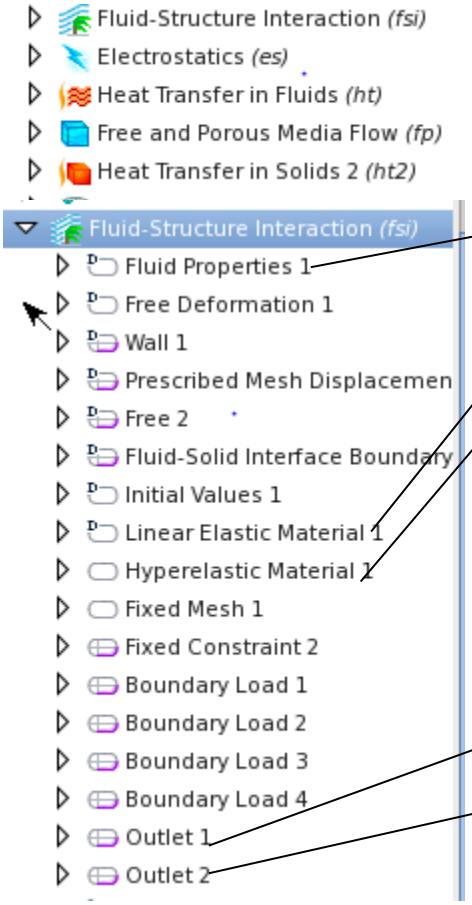

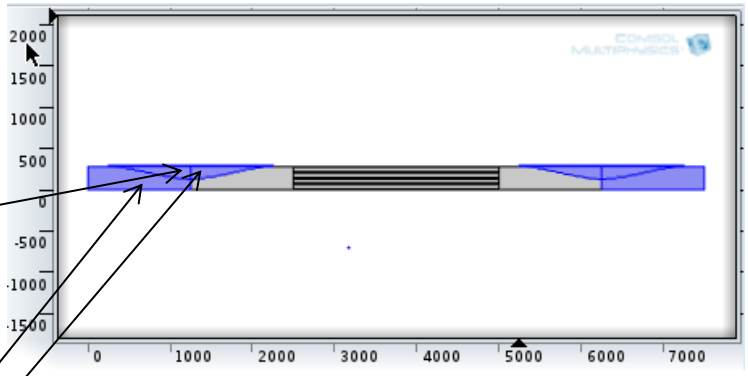

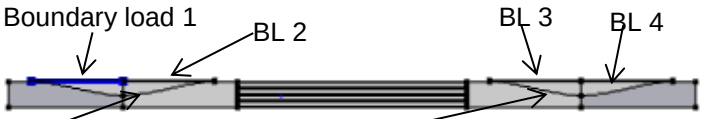

Boundary load 1

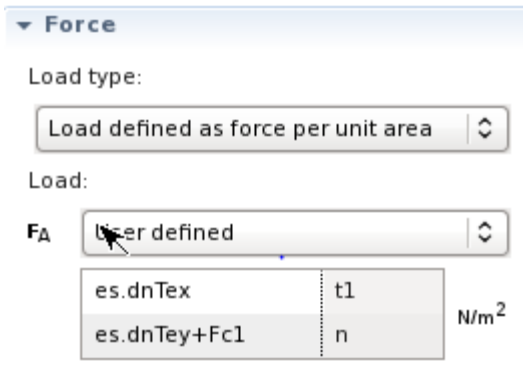

BL 2

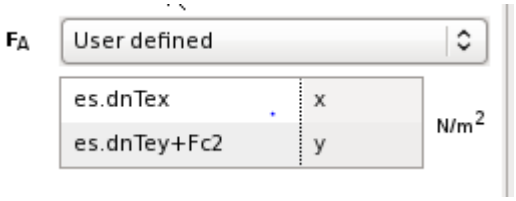

BL 3

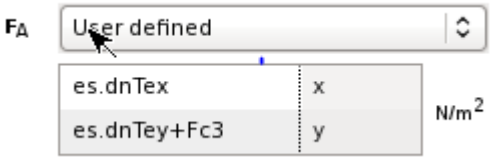

BL 4

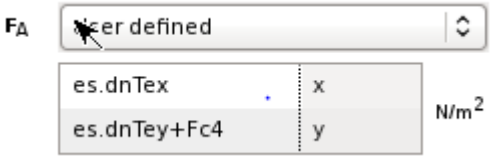

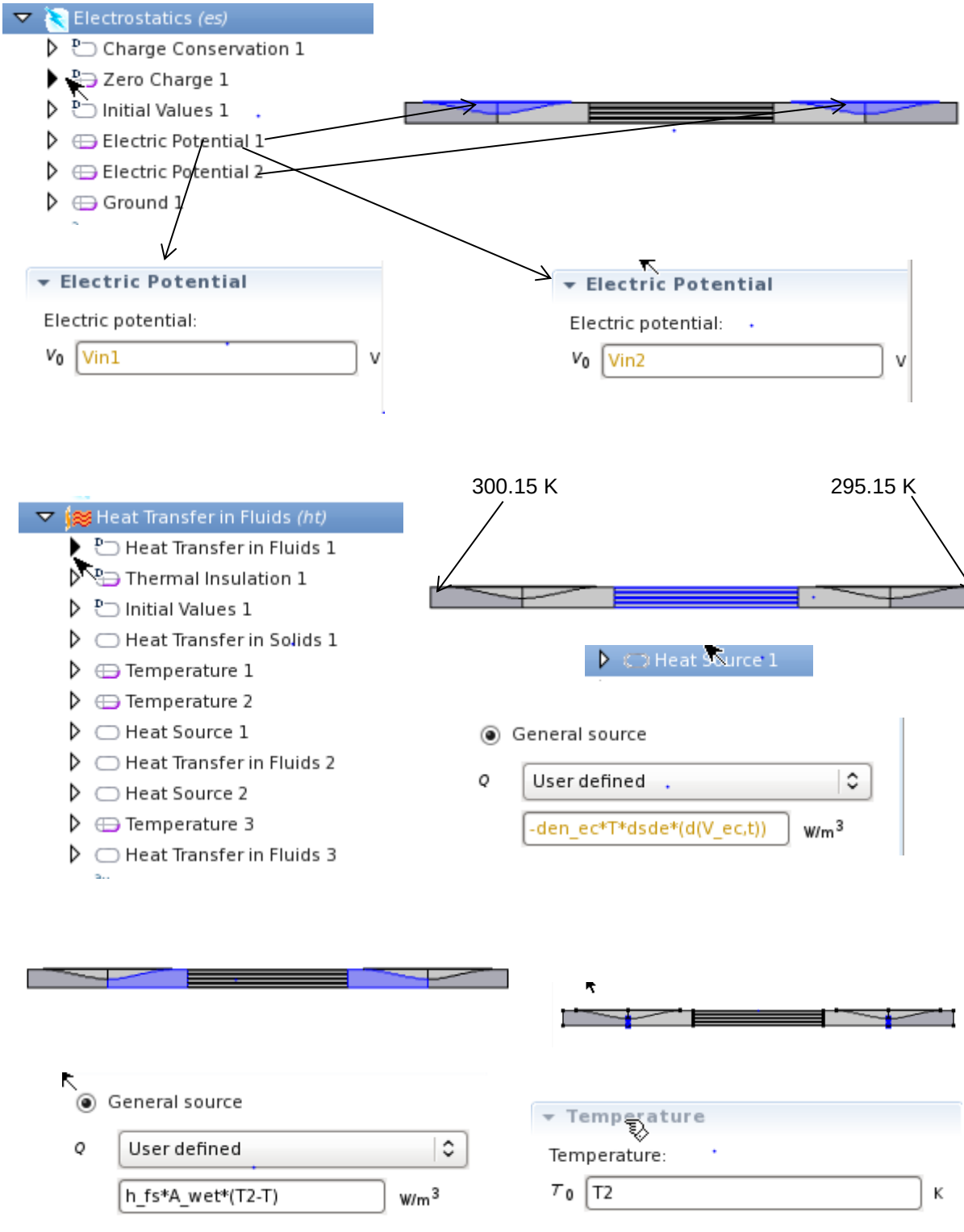
Electrostatics (es)
Charge Conservation 1
Zero Charge 1
Initial Values 1
Electric Potential 1
Electric Potential 2
Ground 1
Electric Potential
Electric potential:
V0
Vin1
V
Electric Potential
Electric potential:
V0
Vin2
V
Heat Transfer in Fluids (ht)
Heat Transfer in Fluids 1
Thermal Insulation 1
Initial Values 1
Heat Transfer in Solids 1
Temperature 1
Temperature 2
Heat Source 1
Heat Transfer in Fluids 2
Heat Source 2
Temperature 3
Heat Transfer in Fluids 3
300.15 K
295.15 K
Heat Source 1
General source
Q
User defined
-den_ec*T*dsde*(d(V_ec,t))
W/m3
General source
Q
User defined
h_fs*A_wet*(T2-T)
W/m3
Temperature
Temperature:
T0
T2
K

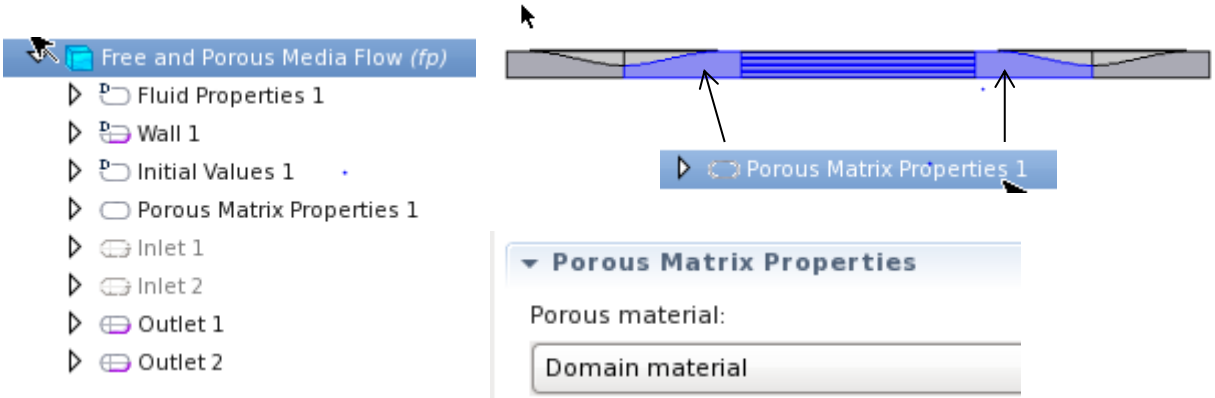
Free and Porous Media Flow (fp)
Fluid Properties 1
Wall 1
Initial Values 1
Porous Matrix Properties 1
Inlet 1
Inlet 2
Outlet 1
Outlet 2
Porous Matrix Properties 1
Porous Matrix Properties
Porous material:
Domain material
Porosity:
ϵ_p
User defined
epss
Permeability:
κ_{br}
User defined
1.87e-10
Boundary Condition
Boundary condition:
Velocity
Normal outflow velocity
Velocity field
u_0
u_fluid
x
v_fluid
y
m/s
Boundary Condition
Boundary condition:
Velocity
Normal outflow velocity
Velocity field
u_0
u_fluid
x
v_fluid
y
m/s

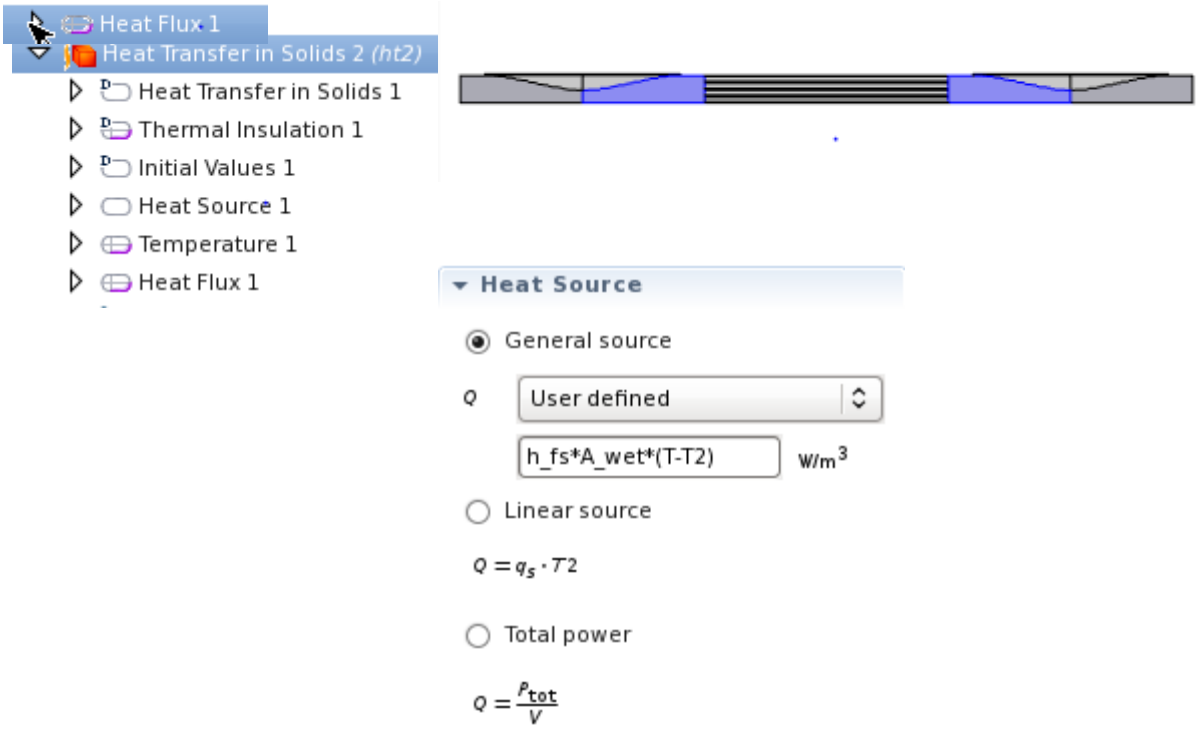
Heat Flux 1
Heat Transfer in Solids 2 (ht2)
Heat Transfer in Solids 1
Thermal Insulation 1
Initial Values 1
Heat Source 1
Temperature 1
Heat Flux 1
Heat Source
General source
Q
User defined
h_fs*A_wet*(T-T2)
W/m3
Linear source
Q = qs · T2
Total power
Q = Ptot / V

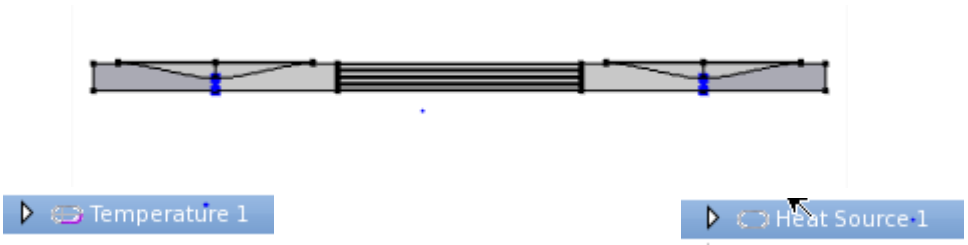
Temperature 1
Heat Source 1

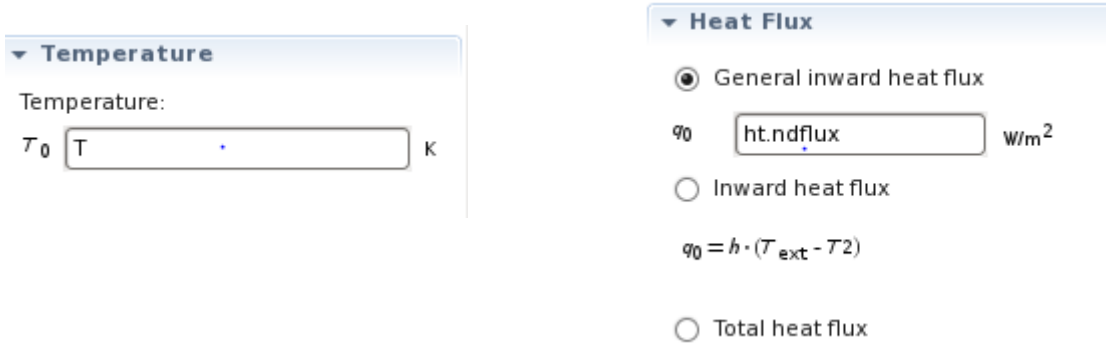
Temperature
Temperature:
T0
T
K
Heat Flux
General inward heat flux
q0
ht.ndflux
W/m2
Inward heat flux
q0 = h · (T ext - T2)
Total heat flux

- *Mesh*

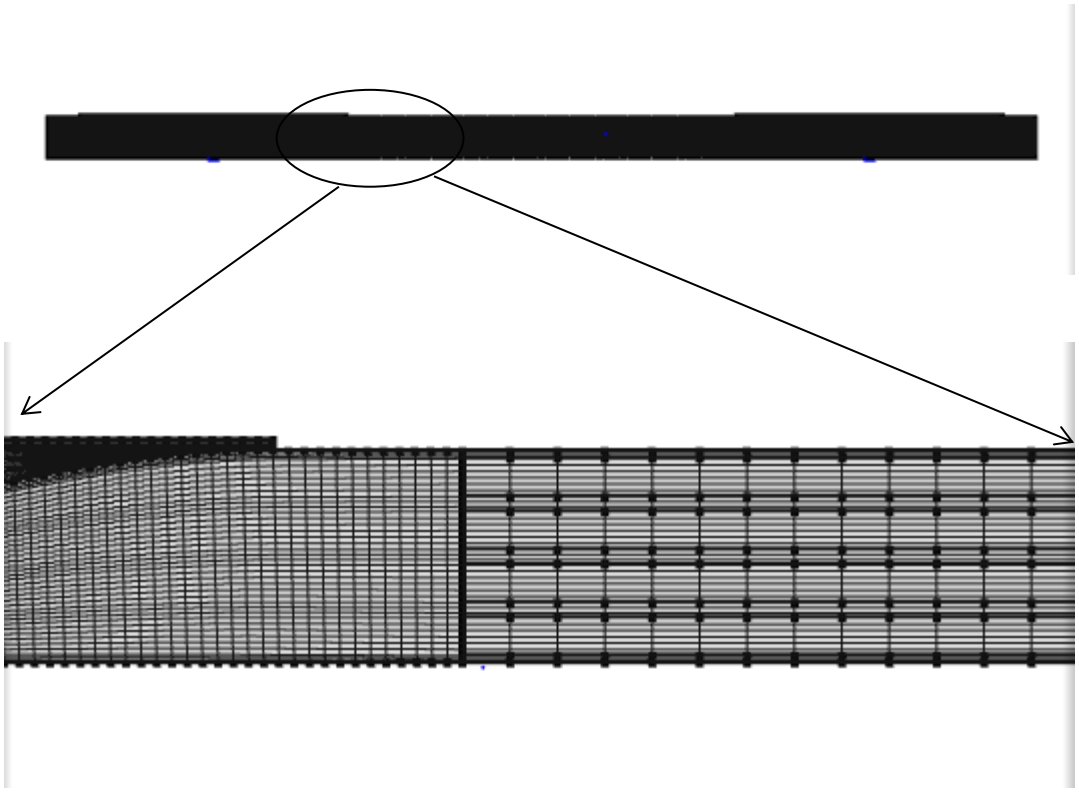

- *Study*

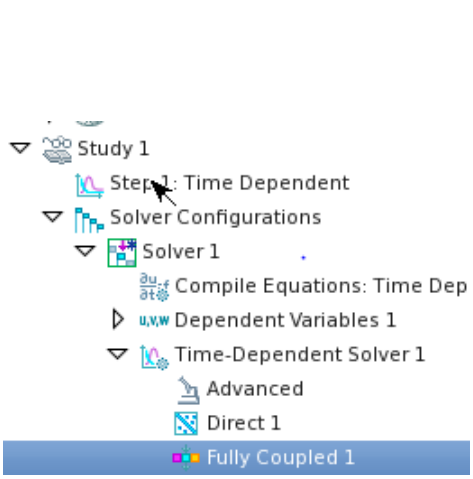
Study 1
Step 1: Time Dependent
Solver Configurations
Solver 1
Compile Equations: Time Dep
Dependent Variables 1
Time-Dependent Solver 1
Advanced
Direct 1
Fully Coupled 1

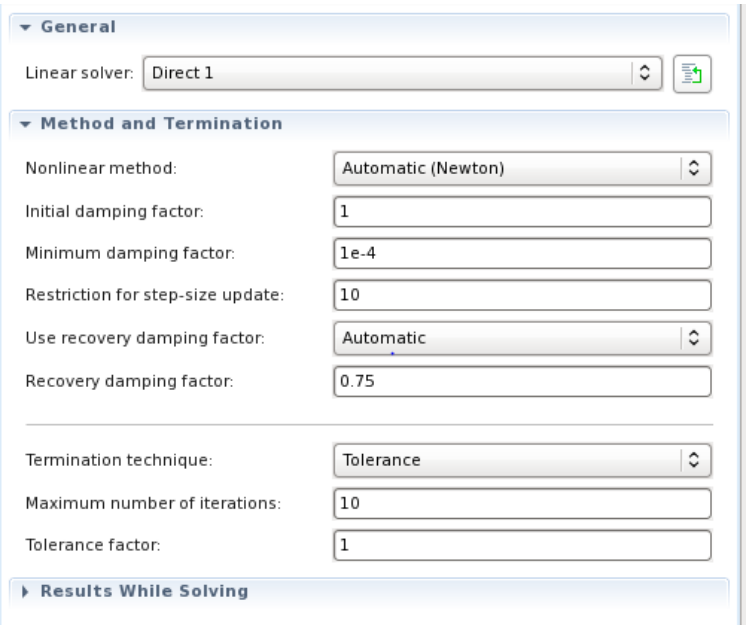
General
Linear solver: Direct 1
Method and Termination
Nonlinear method: Automatic (Newton)
Initial damping factor: 1
Minimum damping factor: 1e-4
Restriction for step-size update: 10
Use recovery damping factor: Automatic
Recovery damping factor: 0.75
Termination technique: Tolerance
Maximum number of iterations: 10
Tolerance factor: 1
Results While Solving

Appendix H

Pictures of P(VDF-TrFE-CFE) film

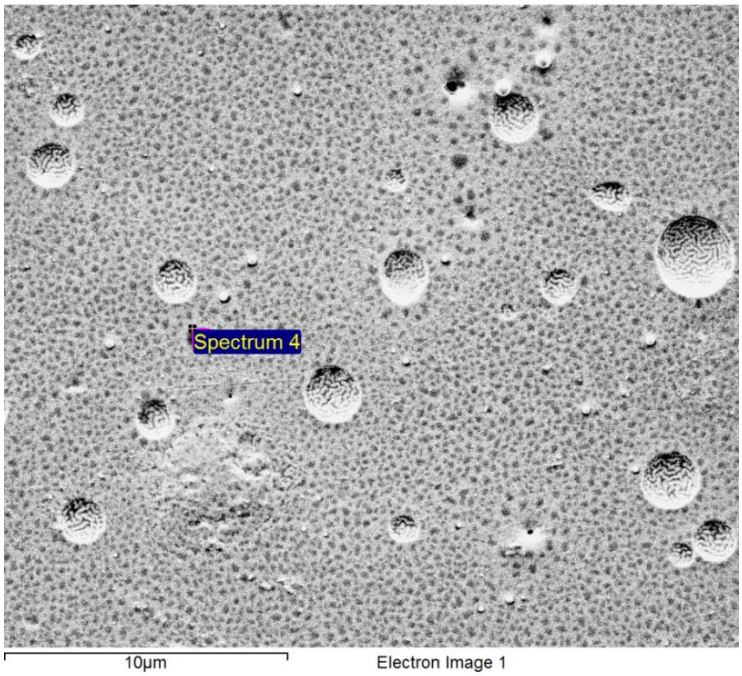

SEM picture of CMU film with gold, before test

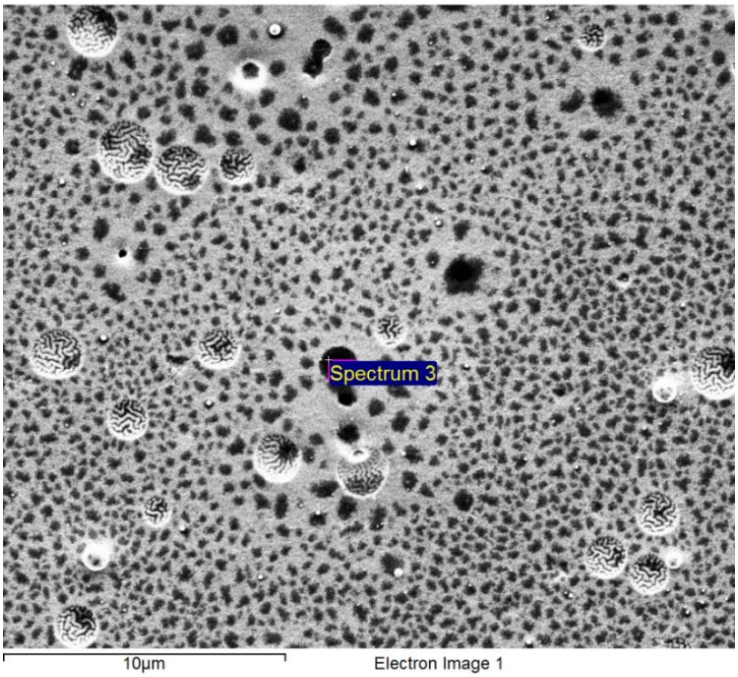

SEM picture of CMU film with gold, after test

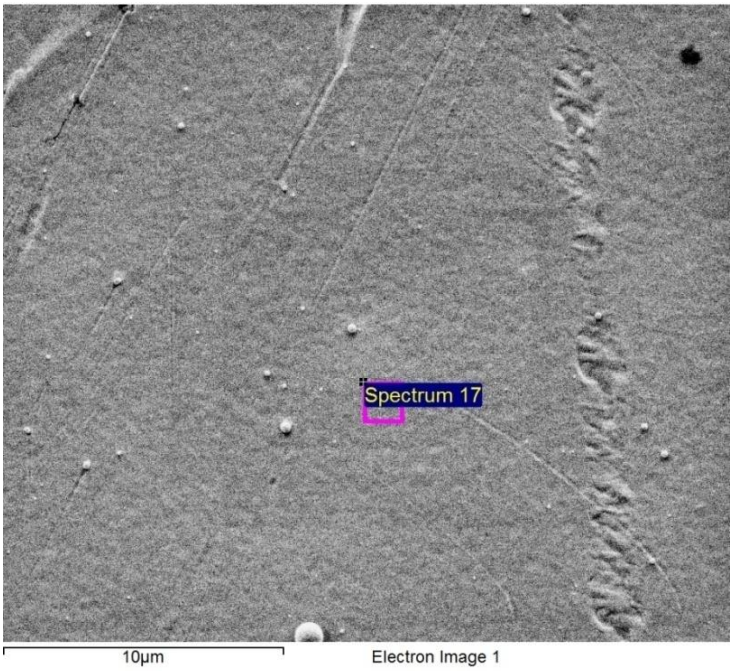

SEM picture of Piezotech film with gold, before test

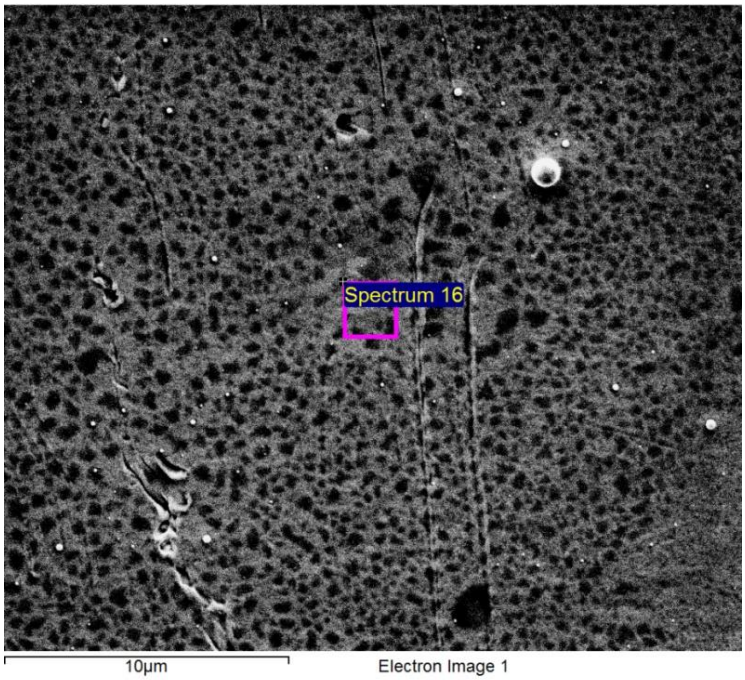

SEM picture of Piezotech film with gold, after test

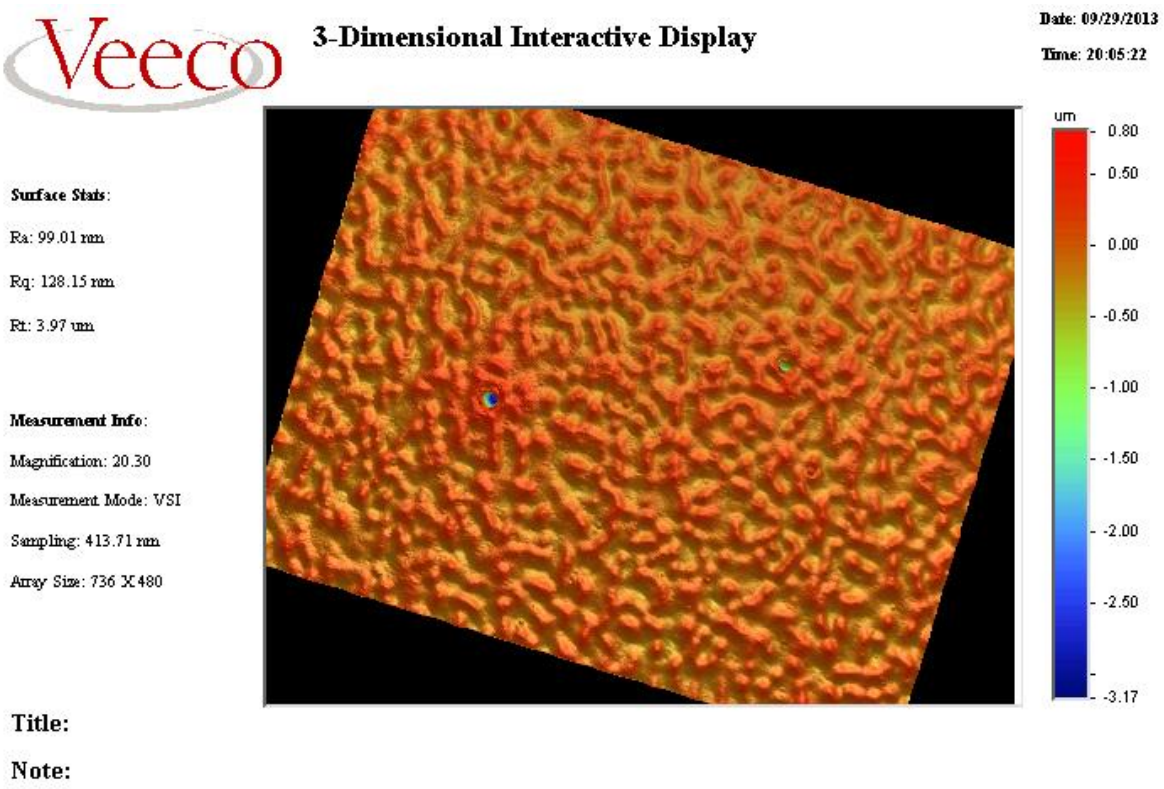

Pits on the film with gold, which may cause breakdown of the film when a high voltage is applied.